

# Development of Digital Architectures for Pixelated Readout of Time Projection Chambers: Q-Pix

Dissertation by  
Kevin Keefe

A DISSERTATION SUBMITTED TO THE GRADUATE DIVISION OF THE UNIVERSITY  
OF HAWAI'I AT MĀNOA IN PARTIAL FULFILLMENT OF THE REQUIREMENTS FOR  
THE DEGREE OF  
DOCTOR OF PHILOSOPHY  
IN  
PHYSICS



KE KULANUI O HAWAI'I MA MĀNOA  
Mānoa, Hawai'i

2023

Dissertation Committee:

Kurtis Nishimura

Chairpersons

Jason Kumar, John Learned, Robert Wright, Peter Sadowski, Gary Varner

Keywords: Field Programmable Gate Array, Time Projection Chamber, Neutrino Oscillation

© 2023

Kevin Keefe  
ORCID: 0000-0001-5794-879X

All rights reserved except where otherwise noted

## ACKNOWLEDGEMENTS

## ABSTRACT

The Standard Model (SM) of physics has proven annoyingly successful in past decades, despite several measurements which hint at its incomplete description of nature. The hunt for New Physics (NP) continues at higher energies ( $>> 1\text{GeV}$ ) with larger detectors ( $\approx 10kT$ ). One such future detector is The Deep Underground Neutrino (DUNE) detector. DUNE (as any beam detector) is a combination of two detectors, a near-detector (ND) and a far-detector (FD) for long-baseline neutrino oscillation measurements. The DUNE FD will be a large scale ( $\approx 40kT$ ) Liquid Argon Time Projection Chamber (LArTPC). This 40-kT scale detector requires high precision in both timing ( $<< \mu\text{s}$ ) and spatial resolutions ( $\approx 1\text{mm}$ ) for vertex reconstruction of interesting neutrino events.

This dissertation discusses recent progress and characterization of a novel implementation of a new pixelated LArTPC readout technology. This novel readout is based on a pixel-level charge-integrate-reset circuit: Q-Pix. We present the basic pixel-level readout circuit and the implications of such an implementation when applied at kiloton LArTPC scales. We also show results from the first prototype implementation based on the Q-Pix readout, which was designed using only off-the-shelf electronics. One problem with any pixelated readout is the ability to handle a large number of unique data channels, which in the case of the DUNE FD is  $\approx 10^8$ . To address the scaling problem, we have developed and tested a modular digital back-end prototype as a proof of concept. In this dissertation, we discuss nominal system requirements to achieve the DUNE-FD APA scale for radiogenic background sensitivity, as well as pixel-level calibration techniques for both timing and charge. Simulations have also been performed based on projected radiogenic backgrounds and high-energy neutrino beamline events, providing initial estimates of the digital back-end requirements in both the quiescent and active states. Finally, based on these results from the simulations and prototypes presented here, we discuss the nominal digital back-end readout constraints of a fully realized Q-Pix implementation for a DUNE-FD APA .

## TABLE OF CONTENTS

Acknowledgements . . . . .	iii
Abstract . . . . .	iv
Table of Contents . . . . .	v
List of Illustrations . . . . .	vii
List of Tables . . . . .	xviii
Chapter I: Introduction . . . . .	1
1.1 The State of Things: The Standard Model . . . . .	1
1.2 The Problem: Moving Beyond the Standard Model . . . . .	7
1.3 Modern Tracking Detectors . . . . .	10
1.4 Ways Forward . . . . .	12
1.5 Neutrino Tracking Detectors in the Current Century . . . . .	19
1.6 Future Detectors . . . . .	20
Chapter II: A Novel Readout Technique for TPCs: Q-Pix . . . . .	23
2.1 Q-Pix: The Circuit Level Design . . . . .	23
2.2 How Q-Pix fits into a 10 kt LArTPC . . . . .	31
2.3 The Digital Back-end . . . . .	36
2.4 Q-Pix and Light Detection . . . . .	36
2.5 Q-Pix at Low Energy: Supernova Studies . . . . .	38
Chapter III: The First Prototype: First Resets and Leakage Measurements . . . . .	40
3.1 Simplified Analog Q-Pix: System Design . . . . .	40
3.2 The SAQ Prototype Design . . . . .	40
3.3 Noise Measurements . . . . .	42
3.4 Xenon Gas Lamp Measurements . . . . .	43
3.5 Results and Discussion . . . . .	43
Chapter IV: Digital Back-end Viability Studies . . . . .	50
4.1 Digital Design Overview . . . . .	50
4.2 The Digital Finite State Machine . . . . .	57
4.3 The Parameter Space of the Digital System . . . . .	58
4.4 The Digital Back-end problem . . . . .	59
4.5 Constraining the digital back-end Design . . . . .	61
4.6 Frequency Calibration of Local Oscillators . . . . .	73
4.7 The Digital Prototype Design . . . . .	78
4.8 Timing Stability . . . . .	82
4.9 Power and Current Characteristics . . . . .	82
4.10 Analysis of Systematics for Different System Implementations . . . . .	82
4.11 Towards the Integration of the Aggregator Node . . . . .	82

4.12 Comments on A Super-DAQ-Node	82
4.13 The Back-End Summary	82
Chapter V: The Q-Pix Back-end and Simulation Studies for Future Q-Pix Prototypes	83
5.1 The Tile Simulation Framework	84
5.2 The Tile Parameters	88
5.3 Simulating The Tile Readout	91
5.4 Physical Simulation Studies	99
5.5 Neutrino Interaction Studies	109
5.6 Q-Pix for Neutrino Oscillation Measurements	115
5.7 Neutrinos, Backgrounds, and Routing	116
5.8 Summary and Further Studies	129
Chapter VI: Summary and Outlook	131
6.1 Conclusions	131
Bibliography	133
Appendix A: Neutrino Interaction Integral Data	139
Appendix B: Q-Pix Analog ASIC First Prototype	151

## LIST OF ILLUSTRATIONS

<i>Number</i>		<i>Page</i>
1.1	Image of Fundamental Particles in the Standard Model, taken from CERN website [1]. All known matter and particle interactions involves combinations of the particles shown here. . . . .	3
1.2	Image based on the 2008 P5 report [2]. The white text labeled within each frontier describes the search for some physics beyond the SM within that frontier. . . . .	8
1.3	Image of a Time Projection Chamber (TPC). Charge is accumulated within the volume as ions are removed from the fiducial volume from another charged ion as it passes through the material. An uniform electric field drifts the free now electrons towards the anode plane. The collection and readout of charge on this anode plane is what is recorded within the detector. Image is taken from [3]. . . . .	12
1.4	Representation of the mass hierarchy scales. This is a representation of the two possible orderings of neutrino masses, due to the uncertain sign of $m_{13}$ . It is also interesting to observe that the absolute mass scale is not measured since oscillation measurements only give difference mass squares. Image was taken from [4]. . . . .	18
1.5	Representation of the Near and Far Detectors for the DUNE experiment. The Near Detector is located within the image labeled as the Particle Detector. One of the key purposes for the Near Detector is to tag outgoing particles from the proton beam. Image was taken from [5]. . . . .	22
2.1	A simplified schematic of front-end Q-Pix Readout circuit. The front-end is a charge sensitive amplifier (CSA) whose output is connected to a Schmitt trigger. The trigger (output) occurs when enough charge as accumulated on the capacitor $C_f$ (currently 1 fC). One of the design parameters for the Q-Pix front-end is the choice of $C_f$ . This front-end circuit is designed within a single analog ASIC which has contains 16 of these circuits. The schematic for this ASIC is shown in Appendix B. Image is taken from [6]. . . . .	24

2.2	A modified image from ?? is shown. The blue box is the Q-Pix circuit (Figure 2.1), which we refer to as the Q-Pix "analog front-end". The right side of the image, encompassed in orange box, we refer to as the "digital back-end". The back-end is responsible for providing the local oscillator as well as accurately recording a reference counter to correspond to the time when the Schmitt trigger signal is received. . . . .	25
2.3	Example reconstruction of the reset time difference (RTD) based on the Q-Pix readout design. Shown is transistor-level charge integration simulation results for minimum ionizing tracks in LAr. The purple curve of the top pannel represents charge accumulating on the CSA, where the green curve is the reset output from the Schmitt trigger. The bottom pannel shows input charge (purple curve) overlayed on top of the reconstructed current signal. The $Q_o$ value taken here is equal to 1 fC. Image is taken from [6]. . . . .	27
2.4	Example reconstruction of the reset time difference (RTD) based on the Q-Pix readout design. Shown is transistor-level charge integration simulation results for minimum ionizing tracks in LAr. $Q_o$ was chosen to be 0.3 fC. The bottom panel in this image shows a better match of the reconstructed signal with a smaller $Q_o$ . However, more ( $\approx 1.0$ fC / 0.3 fC) resets are produced as a result. Image is taken from [6]. . . . .	28
2.5	Arbitrary sine wave based current input. The maximum amplitude is chosen to be close to $I_{max}$ . Reset Charge is chosen to be 1 fC and digital clock frequency of 30 MHz. The input current amplitude is close to the maximum, so that the reconstructed current can be far from the actual. This occurs since $N_{rtd}$ can only take integer values, the reconstructed current can only take values of $\frac{30}{N}$ . The red points indicate possible reconstructed current values, where the two highest points correspond to $\frac{30}{7}$ and $\frac{30}{8}$ , respectively. However, an example of a savgol filter (dark blue) is performed on the resets after the fact with near agreement of the large input. A use case of this kind of digital filtering would be applied to large current values only (peaks of the curves), and not for low current inputs where the pure timestamp difference provides better results. . . . .	30

2.6	Reconstruction of Sub figures cumulative distribution function (CDF) of charge as a function of time (a) and the error (b). The input current for these data are showin in Figure 2.1. The pause in resets are when the error is small, since the current input is near zero. The red line indicates the minimum charge required for a single reset. The right plot indicates the difference between the true and reconstructed charge distributions compared to a single reset. . . . .	31
2.7	Image taken from [7], Fig 1.12 of section 1.8. Image shows an overlay the the relevant charge collection wires within a DUNE-FD SP LArTPC. . . . .	32
2.8	A simple caption [7] . . . . .	33
2.9	Images taken from [ <a href="https://doi.org/10.48550/arxiv.2207.11127">https://doi.org/10.48550/arxiv.2207.11127</a> .] The vertical drift geometry (left) shows an electrode on the top layer, whereas the horizontal (right) geometry integrates the electrodes within the aSe. The vertical geometry is an easier design, but most electrodes are not transparent to VUV scintillation light. The horizontal geometry solves this problem, at the cost of a more complicated design.	38
2.10	Image is taken direclty from [9]. Plotted is the supernova burst triggering effeciency as a function of $\nu_e$ interactions in a 10 kT DUNE-FD module. The points in blue indicate that a series of 60 resets are "clustered" to use as an identification of a supernova event. The other curves are taken from Ref. [supernova_Abi_2021]. . . . .	39
3.1	The SAQ Setup model based on ???. . . . .	41
3.2	The SAQ Setup model based on 3.2. . . . .	42
3.3	The SAQ Setup model based on ???. . . . .	43
3.4	Picture of the TPC and DAQ setups at Wellesley University. . . . .	44
3.5	The SAQ circuit in a Spice Simulation. The IVC [10] chip chosen as the off-the-shelf integrator for this experiment. The main selection choice for this part is due to its low input bias current $\ll 750 \text{ fA}$ . . . . .	45
3.6	An image of the data acquisition board from Digilent, Zybo Z7-20. This board was chosen for its multiple configurable input channels, as well as the Zynq-based archiecture of the onboard FPGA. Additionally, the use of the ethernet provides 1 GB transfer speeds, which is more than sufficient for the application. Packet data transfer rates have been verified with this readout at stable rates of 10 kHz. . . . .	46
3.7	The SAQ GUI with real time plotting of incoming resets to the Zybo board. . . . .	47
3.8	Drift Current Measurements to go here. . . . .	48
3.9	First diffusion measurement in P-10 gas performed at Wellesy University. . . . .	49

4.1	Diagram of the Digital node. The controlling sections of the logic for the digital node are QpixComm, QpixDataProc, QpixRoute, and QpixRegFile. The Comm layer is responsible for routing packets between the physical layer and handles the parsing of incoming data packets. The DataProc layer is responsible for recording timestamp data during a reset from the analog front-end. The RegFile contains configuration information, such as routing. QpixRoute determines the controlling state machine that, based on register configurations, determines what packets are sent to which neighboring nodes. . . . .	51
4.2	Example of Datum words and their allocation as currently implemented in the simulation and first prototypes. . . . .	56
4.3	Diagram of the endeavor transmission (Tx) protocol. . . . .	56
4.4	Diagram of the Digital node's FSM which determines how to respond to incoming packets. . . . .	58
4.5	Example of an Corner Base-Node configuration. The base-node is colored and highlighted in red. . . . .	64
4.6	Example of the fully connected routing configuration for a tile (FCT). Each Node represents a digital channel which must be aggregated, and the red and blue connections distinguish directions of communication. The red connection lines indicate pathways away from the base node, whereas the blue lines represent connection paths towards the base-node in the upper-left. . . . .	65
4.7	Minimal Occupancy Path of a FCT. This routing path ensures that the number of input connections equal the number of output paths for the node. . . . .	68
4.8	Minimal Delay Path of a FCT. This routing path ensures that the minimum number of transactions occur from every node in the FCT to reach the base-node. For any node along any column this is equivalent to the sum of the row and column of that node. . . . .	70
4.9	Minimal Routing Path of a FCT. This routing path ensures that the number of input connections equal the number of output paths for the node. . . . .	71
4.10	Example of an Edge base-node configuration. The base-node is colored and highlighted in red. . . . .	72
4.11	. . . . .	78
4.12	Example of frequency calibrations for the FPGA Adjacent to the Zybo. . . . .	79
4.13	. . . . .	80
4.14	. . . . .	80

4.15	.....	81
5.1	Composition of an example $4 \times 4$ tile. Each node in the tile represents a digital ASIC which contains two FIFOs. One FIFO is used to store timestamps from reset data, which we refer to as the local FIFO. The other FIFO we call the remote FIFO and is used to store all packet transactions from neighbor nodes. The local FIFO is 48 bits wide, where 32 bits come from the timestamp and 16 bits are from the pixels. The remote FIFO is 60 bits wide, since it must store all relevant bits for the 64 bit packet word, where there are 4 unused bits. .....	85
5.2	Example timeline for simulation time steps and injected hits. Before the simulation begins hits are added into a Hit Container for each node. When the simulation begins the time is incremented by a single time step ( $\tau = 1\mu s$ ). The time increments until it is larger than the time of any of the injected hits. The values of the timestamps are then moved from the Hits container into the local FIFO, where the timestamp that is recorded is the soonest clock cycle after the "true" time of the injected hit. When the data are ready to be transmitted from the local FIFO, the time is then updated by transaction time. An example of this procedure is shown in Figure 5.3. ....	87
5.3	Flow chart of the simulation process method which occurs for every simulation time step. The simulation contains a queue of packet transactions. The queue is sorted by ascending time, so that the earliest transaction completed time is processed first. Each transaction contains a packet, a node, and the time the packet arrives. When the node receives the packet, it can optionally create more transactions, depending on the node's state and the packet. Any additional transactions are added to the simulation queue, and are time sorted. The simulation then increments the time for all other nodes within the tile. This procedure repeats until all nodes in the tile reach the designated time (11 seconds). .....	89
5.4	Distribution of ASIC frequencies used in the $8 \times 8$ tile, and in the example FIFO buffer depths for this chapter. The numbers plotted above each ASIC row and column indicate the relative frequency of this ASIC compared to the nominal 30MHz mean. For example, a number of 112 indicates an ASIC which is 12% faster than 30MHz, a frequency of $\approx 33.6MHz$ . .....	92

5.5	Example of timing ASIC state transitions in the simulation framework. The x-axis represents time in $\mu\text{s}$ , and the different y-axis labels represent different ASICs within a $3\times 3$ tile shown. The y-axis also indicates the relative frequencies of the ASICs in the tile, where the node at (0,0) has the fastest frequency, which is 12% faster than 30 MHz. The blue regions indicate that the ASIC is in the idle state. The first orange state indicates that this ASIC (2,2) received a register request from the aggregator node and is now sending its local data, concluding in the purple state, which is sending the event end word. The Packets drift apart in time as they are sent from slower to faster ASICs. Shown here is the possiblity of packet drift due to asynchronous packet transfers that depends on the magnitude of the frequency drift between neighbor ASICs. . . . .	94
5.6	A snake packet transaction example is shown. The broadcast is received by the further node (2,2) and 10 data words are sent, followed by a event end word. Each packet tranverses through all nodes in the tile where remote packets are sent immediately. . . . .	95
5.7	A left packet transaction example is shown. The packet transfers begin with the furthest node (2,2) receives a broadcast from the aggregator. The data are then sent to the "left" and then "up" towards the base node, and finally to the aggregator node. . . . .	96
5.8	A trunk packet transaction example of two data words and a single event end word is shown. This routing method allows for the fastest possible transaction time since it minimizes the edge lengths between the base node and all other nodes within the tile. In this $3\times 3$ example shown, the base node is at (1,0), or in the middle. . . . .	97
5.9	Example local FIFO distribution of a $\approx 3\text{GeV } \nu_e$ event. The numbers over each tile represent the total number of writes which occured to each local FIFO in the array. Even with the lowered resolution (each ASIC accounts for 16 pixels), different tracks are noticeable based on the FIFO depths. The maximum scale for the heatmap is chosen to be 512 resets. . . . .	98
5.10	Example of local (a) and Remote (b) fifo depths of the example neutrino event from 5.3 after processing. The colorbar to highlight the maximum number of transactions is used to indicate remote transactions which were happening for 2% of the total readout time of 10 seconds. The node which has the largest remote buffer depth corresponds to the ASIC with the slowest frequency as shown in Figure 5.2. The reason for this excess of buffer depth is due to packet buildup on the slow ASIC. . . . .	99

5.11	Example of local (a) and Remote (b) fifo depths of the example neutrino event from 5.3 after processing. The ASIC which has the largest remote buffer depth also corresponds to the ASIC with the lowest frequency as shown in Figure 5.2. . . . .	100
5.12	Example of local (a) and Remote (b) fifo depths of the example neutrino event from 5.3 after processing. The ASIC which has the largest packet buildup occurs at (4,1). This ASIC also corresponds to the ASIC which has the lowest frequency along the trunk column as shown in Figure 5.2. . . . .	101
5.13	A simulated push architecture with 20 injected hits at different times. The time of the injected reset is indicated by the green points. Before the simulation is run a node has its hits injected into a storage (orange) list. Then, at each simulation time step ( $\tau_{step} = 1\mu s$ ) the list is examined to see if a new hit will be written. When a hit is found the relative time of the node can move forward in time to when this packet will be completed in time, while all other writes can occur to the local FIFO. This is why the first local FIFO depth increases initially by one despite 10 nearly adjacent injected hits. On the next time step, the depth then moves to nine; the simulation has sent the first of the 10 packets, and records nine. This example correctly shows a maximum local FIFO depth of nine. . . . .	102
5.14	Full 1000 second of radiogenic background source simulation input into all pixels within the APA. A close examination of the resets can reveal the additional resets from the backgrounds which are location dependent. The majority of the uneven distribution of resets occur at the location of the APA bars due to the $^{40}\text{K}$ isotope. . . . .	104
5.15	Baseline noise input for the digital simulation from all radiogenic sources and background leakage current. This figure shows the total resets in the 10 second window for the $16 \times 16$ tile. The other tile size configurations ( $4 \times 4$ , $8 \times 8$ , $10 \times 14$ ) also use these reset data for background noise. All tiles start with the top left node as their origin node. . . . .	105
5.16	All 4096 pixels in the $16 \times 16$ tile for 1000 seconds of radiogenic data. The y-axis represents a different pixel, and the x-axis is a log-scale time axis with even bin widths. There are two clusters of resets for different time intervals. The first large cluster of resets occurs at $\approx 10^{-7}$ seconds and is due to a single radiogenic decay event causing additional resets. The second large cluster of resets occurs at $\approx 10$ seconds. This second cluster of resets is caused from the first reset of a new radiogenic decay event. The ability to perform a charge calibration per pixel may depend on accurately resolving the mean for this "long period" RTD. . . . .	106

5.17	All 4096 pixels in the $16 \times 16$ array for 1000 seconds of radiogenic data. These data are the same as those shown in Figure 5.4, where all pixel RTDs are binned together. There are two clusters of resets on two different time scales. The first cluster of resets near at $\tau_{rtd} \simeq \mathcal{O}(10^{-7})$ is due to events which produce more than one reset. The second cluster of resets near at $\tau_{rtd} \simeq \mathcal{O}(10^1)$ are from a "waiting" period where there is no charge buildup from decays and only background noise. The dominant source of electrons on each pixel is from the $^{39}\text{Ar}$ , with a non-zero contribution from leakage. The leakage current value used in this simulation is 10 aA. . . . .	107
5.18	Both figures indicate a comparison of the amount of electrons deposited on all pixels in the tile shown in Figure 5.4. Plot (A) represents the total number of electrons on a log scale. As expected, $^{39}\text{Ar}$ contributes the majority of background charge. The leakage current used is 10 aA, and represents about 10% of the total contribution of electrons. This implies that leakage currents from the front circuit which are $\approx 100$ aA will contribute nearly as much electrons to the steady-state RTDs as the radiogenic backgrounds. . . . .	108
5.19	Flux spectrum of neutrinos from the neutrino beam used in this study. This figure is taken from [87]. Highlighted in blue is the reconstructed energy range of neutrinos that are used to seed the interaction with the APA LAr's volume. . . . .	110
5.20	Rate of CC neutrino interactions based on flavor as a function of true neutrino energy. Figure is taken directly from [11]. Right is shown the neutrino interaction distribution for the forward horn current. The left image is for the reverse horn current. Both images assume an average exposure rate of 1.2 MW from LBNF beam.	111
5.21	Same $\nu_e$ interaction at Z-position = 180cm, which is in the middle of the drift length of the APA. Image (A) has the incident $\nu_e$ momentum rotated upwards ( $\theta_z = +90^\circ$ ). Image (B) has the incident $\nu_e$ had momentum along the beam direction ( $\theta_z = 0^\circ$ ). Since there are five different z-positions, and five different $\theta_z$ values, each of the 3900 $\nu_l$ interactions are repeated 25 times. These two plots show two of those 25 examples. . . . .	113

5.22	The same $\nu_e$ event as the one shown in Figure 5.21-(A). The plot is zoomed into to the region of interest where the bin widths represent the pixels dimensions in the collection plane. The energy of this $\nu_e$ was 546.1 MeV, and considering that each reset requires 0.1475 MeV, the maximum number of resets this event could produce is $\approx 4368$ . The histogram records 3733 total resets. The most active pixel received 144 resets. When the pixels are binned into ASICs ( $4 \times 4$ pixels) the maximum number resets an ASIC received is 347. . . . .	114
5.23	Example $\nu_e$ events for different z-position of the vertex with $\theta_z = 0$ held constant. Plot (A) bins the maximum value of local FIFO depth for all 3900 events ( $\nu_l$ energies between 250 MeV - 10 GeV) for variable z-position and $\theta_z = 0$ . Plot (B) shows the running integral for each histogram shown in plot (A). The integral continues until 99% of all events are counted. This process is repeated for all 200 possible parameter choices as discussed in Table 5.5. . . . .	115
5.24	Example $\nu_e$ events for different $\theta_z$ with the vertex held constant with z-position = 180 cm. This is a similar plot to Figure 5.23 with the exception that $\theta_z$ is varied and the z-position is held constant at z = 180 cm. A notable difference to note here is the run away effect of the large values of $\theta_z$ . This effect is intuitive: the initial momentum direction affects the direction of where most charge will be deposited. As more charge is localized an ASICs area, it will collect more resets. . . . .	116
5.25	Comparison of buffer depths as a function of energy for different parameters of $\theta_z$ and z-position. There is a large variance between the true $\nu_l$ incident energy and the actual energy deposited in the LAr. This is the reason why only the means are plotted for each energy bin. Plot-(A) shows that the average z-position has a minor affect on the overall local FIFO depth, where the furthest position has the lowest average reset count. Plot-(B) shows average FIFO depth for varied $\theta_z$ . The two curves represented by $\theta_z = \pm 90^\circ$ are similar because they use the same seeded events only pointed up or down, and should have the symmetrical effect since vertex is located in the center of the APA. . . . .	117
5.26	A comparison of ASIC resets vs the energy deposited into the LAr. Plot-(B) shows for Z-position=10 cm ends at $\approx 2$ GeV since no $\nu_e$ events deposit this much energy into the LAr. Both plots indicate that the . . . . .	118

- 5.27 Plot-(A) shows a comparison of the energy deposited into the LAr as a function of the input neutrino ( $\nu_e$ ). Plot-(B) shows a projection against the y-axis for a single bin. The maximum allowed total energy deposited is limited to the total energy of the input neutrino. However, the lower bound for all energies is still, obviously, zero. Therefore, as the input neutrino energy increases the upper bound also increases. The mean value of Plot-(B) indicates that even for a maximum allowed total energy of 5 GeV the mean (average) energy deposited per event is 1479 MeV. Most interactions deposit less than 2 GeV into the LAr, as shown in Figure 5.27. Some pileup events are removed, see Figure 5.5. . . . . 118
- 5.28 A relationship between the total number of resets detected in the APA and the energy deposited for  $\nu_e$  interactions is shown. The solid red line indicates the maximum number of resets that could be measured for a given energy. The small distribution of energies below zero correspond to events that produced no resets. The energy deposited goes above the the threshold limit of 10 GeV. These events carry extra energy from additional leptons which are from pile-up at the DUNE-ND from the FNAL beam. These data are not included in the energy deposited analysis, or in the integrals as shown in Figure 5.21. These high energy deposit events are also not included in the FIFO depth analysis, since these events are beyond the energy range for oscillation measurements. These events are also removed from Figure 5.27. . . . 119
- 5.29 Total integral data for all neutrino event parameters described in Table 5.5. The values of the integrals binned in this figure can be found in Appendix A. These data clearly indicate two different distributions of FIFO requirements. The final Q-Pix design will choose some local FIFO depth. The current Q-Pix digital prototype local and remote FIFO depths are also shown by the red and green lines, repsectively. The data in this plot required 6520 electrons to produce a single reset ( $C_{pixel} = 1 \text{ fC}$  and  $V_{pixel} = 1 \text{ V}$ ). Should the pixel's capacitance or voltage change, the x-axis of this plot would scale approximately by the same factor. . . . . 120
- 5.30 Comparison of buffer depths integrated over energy colored by different parameters of  $\theta_z$  and z-position. The most important result is shown in Plot-(A), which clearly indicates that only two different parameters account for the distribution of larger local FIFO depths. As expected,  $\theta_z$  affects the localization of charge over individual ASICs which affect the local FIFO depth. Plot-(B) shows the distribution of resets indicated by different z-positions. Plot-(B) differs in that the second distribution of resets contains elements from each of the different z-positions. . . . . 121

5.31	Comparison of buffer depths as in incoming prototype and horn current direction from neutrino beam. Plot-(A) indicates that there is not a large average difference between the different neutrino flavors and local FIFO depth. Plot-(B) indicates that the different flux from the two horn currents also do not measurably affect the two different distributions. Plot-(A) however does show a slight difference between $\nu_e$ and $\bar{\nu}_\mu$ . $\nu_e$ has an average local FIFO depth of 394 in the small distribution, where $\bar{\nu}_\mu$ has an average of 313. Most ( $\geq 65\%$ ) of this difference is accounted for the fact that the selected $\nu_e$ near-beam ( $\theta_z = \pm 2^\circ, 0^\circ$ ) events deposited more energy, 1894 MeV than the $\bar{\nu}_\mu$ events 1219 MeV, causing more resets. After the energy correction the mean FIFO depths differ by less than one standard deviation. . . . .	122
5.32	Figure is taken from from the DUNE-FD TDR [12]. Images show the $\nu_e$ and $\bar{\nu}_e$ appearance spectra respectively. The left image shows the reconstructed energy distribution for the beam running in the forward horn current direction for 3.5 years. The weight of appearance spectra decreases with increasing energy beyond $\approx 8$ GeV and has a maximum between 1 and 2 GeV. . . . .	123
5.33	Figure is taken directly from the DUNE-FD TDR [12]. Images show the $\nu_\mu$ and $\bar{\nu}_\mu$ disappearance spectra respectively. The plots assume normal mass ordering and are also staged for 3.5 years (staged) exposure for the beam running in the forward horn current and 7 years in the reverse horn current. The weight of disappearance spectra decreases with increasing energy beyond $\approx 8$ GeV and has a maximum between 1 and 2 GeV. . . . .	124
5.34	Weighted integrals for all neutrino event parameters, with weights drawn from the expected signal curves from Figure 5.6 and Figure 5.6. This plot is similar to Figure 5.5, with the exception that the interaction weights are drawn for the (dis)appearance spectra expected at the DUNE-FD module. The buffer for the oscillation measurements require 394 compared to the uniform interaction energy of 426. . . . .	125
5.38	A caluclation of all of the Reset Time Differences (RTDs) for the example scatter event shown in Figure 5.21. A packet transaction takes $\approx 50$ $\mu$ s to occur. The distribution of RTDs for a scatter event indicate that most of the resets occur separated by less than 1 $\mu$ s. . . . .	130
B.1	Full Schematic of the upcoming Q-Pix analog front-end ASIC. . . . .	152

## LIST OF TABLES

<i>Number</i>	<i>Page</i>
1.1 Description of the discovery of quarks. Notice that as the mass increases for a particular quark the year of discovery also increases. This is a property of how we create and observe the quarks in our accelerators, and also the reason why physicists continue to want to build bigger ones. Interesting physics happens at higher and higher energies, which require larger and more expensive detectors to probe these energy scales. Note that the lighter quark masses are not well understood for other experimental reasons, and the presented data are rounded to three significant figures based on [13]. . . . .	4
1.2 Description of the quantum numbers of the fundamental lepton families. There are three unique families within the leptons: electron, muon, and tau. The charge carrier as well as the neutrino each carry a value of one for this number. Their anti-particle counterparts carry -1 of this number. . . . .	5
1.3 Relative strength chart of the four fundamental forces of nature. Although gravity is not included within the SM it is included, as well as its theoretical force carrier the graviton. . . . .	6
1.4 Relevant Liquid Argon parameter information. Values are taken from [14], with temperature $T_s = 87K$ and electric field $E_f = 0.5kVcm^{-1}$ . . . . .	13
1.5 Known Oscillation Parameters of Interest. Values are taken from the global fit [15]. The values shown assume normal mass ordering for neutrinos and include atmospheric Super-Kamikonde Data. . . . .	19
1.6 Comparison of which type of detectors are useful for measuring which values of neutrino oscillation. . . . .	20
2.1 Selected Requirements of DUNE-FD TPC electronics and Expected QPix Design goals of first generation ASIC development for comparison. The table information is taken from the inner three columns of Table 4.1 in [7]. Due to the different charge sensitive geometries between a wire and pixel-based readout, the required noise and number of channels are not easily comparable. . . . .	34

2.2	Q-Pix based Requirements which are compared to the equivalent DUNE-FD SP module found in table 2.2. Results here are necessarily speculative, but provide an insight to the design goal. The system noise is a contribution of leakage current per reset, uneven electric fields in the TPC, or uncertainties in the replenishment circuit per reset. Signal saturation is defined as the maximum measureable current based $Q_o = 1 \text{ fC}$ and $f_o = 30 \text{ MHz}$ . The Q-Pix readout can also be saturated by too many resets if the FIFO buffers overflow (see Chapter 5 for further discussion). . . . .	35
2.3	Summary of design parameters for the first Q-Pix digital ASIC. The local oscillator is a ring oscillator with a targeted mean of 30 MHz. Each ASIC will be able to communicate with up to four neighbor nodes via a custom "Endeavor" protocol. The testing and verification of the endeavor protocol is found in Chapter 4. The values of the local and remote FIFO depth were selected due to fabrication requirements, whose future values are discussion of Chapter 5. . . . .	37
4.1	The address values are not sequential because some registers have become deprecated through development. . . . .	54
4.2	Description of the bit values within the register request word. . . . .	54
4.3	Data word composition. . . . .	55
4.4	The address values are not sequential because some registers have become deprecated through development. . . . .	59
4.5	FPGA calibration results based on hard interrogations at a frequency of 4 Hz. . . . .	79
4.6	FPGA calibration results based on hard interrogations at a frequency of 0.1 Hz. . . . .	81
5.1	The different tile parameters that are used for the effective tile search. The frequency drift relates the relative distribution of the frequency of adjacent oscillators. The tile size determines how many digital nodes are within a single tile. The routing configurations are described in detail in the previous chapter, and refer to how local data words are sent to the aggregator. The two different architectures define how the node enters the transmit local state. The push architecture enters whenever a new reset is acquired, whereas the pull architecture enters only when a data request is received from the aggregator. . . . .	90

5.2	Example results obtained from the three simulation examples for the pull architectures shown in the previous figures. The value of interest in determining the required remote FIFO depths for each ASIC is the maximum depth that occurred on any node. A memory optimized routing configuration is one that would introduce the least strain on the remote buffer depths for a given local buffer depth input. . . . .	97
5.3	The radiogenic background distribution is the same as that found in previous work [9]. For each 1000 ssecond analysis the pre-rounded values are scaled up by a factor of 100 to achieve the correct normalization of events for each isotope. A key difference between the backgrounds is the origin or source of each background. Of special note is $^{40}\text{K}$ whose source location is the APA beams, and whose resets can be distinctly seen in Figure 5.4 as the slightly more active (yellow) region of the APA. Due to this source alone, it is likely that precise auto-calibration for charges will likely have to account for the pixel location within the APA. . . . .	103
5.4	The different neutrino simulation parameters which are passed into Geant4 based simulation. The original interaction products are generated using GENIE [16] v2.12.10. The output products of the neutrino interaction produced from GENIE are then configured using the different parameters described above. We select $\nu_l$ events for different energies in bin-widths of 250 MeV; We follow the same bin width as is done in [12] for their neutrino oscillation analysis. A selection of 100 events for each $\nu_l$ is taken within each energy bin, for a total of 3900 $\nu_l$ events for each horn current direction, z-position, and $\theta_z$ selection. Since there are two current directions, four $\nu_l$ , five z-positions, and five $\theta_z$ positions, a total of 780,000 neutrino events are simulated. . . . .	112
5.5	Transaction Data . . . . .	122
5.6	Buffer Data . . . . .	123
5.7	Transaction Fit Results . . . . .	124
A.1	APA Integral Data . . . . .	150

## *Chapter 1*

# INTRODUCTION

This chapter outlines and highlights useful background that will be explored in further detail in upcoming chapters as well as provides an outline for the thesis.

We begin with an overview of the standard model, and how both its success and short comings drive larger and more expensive detectors. These detectors must reach for ever newer limits, in both precision and scale, due to the robust nature of the Standard Model. To elucidate the issues at the forefront of the Standard Model we provide a brief history, with an emphasis on the detectors and experiments which helped lead to its current status. Next, we become more specific and discuss DUNE which is a example of a new, large, and expensive detector which aims to push beyond the Standard Model. Finally, we finish this section on a discussion on the developments of new tracking detectors and highlight their relevance to the work presented here.

## **1.1 The State of Things: The Standard Model**

What is the universe made of? What are the fundamental building blocks of matter? Since time immemorial thinkers have questioned the nature of the universe and wondered what the basic building blocks of nature are. The answer to these fundamental questions is the motivation for particle physics.

In the history of science, it is easy to argue that the most successful of all models is the Standard Model of Physics. The Standard Model (SM) [17–19] was originally developed in the mid to late 1970’s and is the model responsible for unifying the weak, strong, and electromagnetic forces together. It was gradually developed in the 1970’s as a result of the boom in particle detectors in the mid and late 1960’s. It has made remarkable predictions about the existence of elusive neutrinos, quarks and vector bosons before their discovery, and more.

The comprehensive and extensive list of known particles as well as various cross-sections, lifetimes, and other known information can be found from the bi-annually published Particle Data Group (PDG) [13]. The SM has been experimentally tested to limits unlike any other theory.

In this section we briefly describe the SM and highlight some (certainly not all) key aspects of its

formulation as understood today. The SM has stood the test of time, despite many known failures and holes in its predictions. Therefore, we hope to elaborate a bit on its status involving predictions and unknown parameters to help the reader better appreciate the significance of looking for physics beyond the SM.

### The Basics of the Standard Model

The SM itself dictates what the fundamental constituents of matter and energy are. Like any theory in science, its purpose is to explain observed phenomena. In this case, the observed phenomena are not simply the origin of all observable particles and their masses, but also a description of all observable interactions.

The interactions described by the SM involve the fundamental particle interactions via three of the four known fundamental forces observed in nature: the electromagnetic, weak, and strong forces. The missing fourth force is one of the major shortcomings of the SM: its inability to incorporate a quantum description of gravity. The discussion of the renormalization of quantum gravity is beyond the scope of the work presented here, so we will only mention that it needs to be achieved.

All currently known fundamental particles are represented in Fig. 1.1. These particles represent the today’s best knowledge of the building blocks of all observed matter in the universe.

### The Quarks

The quarks represent particles in the top left of Figure 1.1.

Quarks are the fundamental particles which constitute the “normal” heavy particles, such as protons and neutrons. The quarks also have unique anti-particle partners, which brings the total number of quarks up to 12. Like all antiparticles, the anti-quark partners have the same mass as the normal partners, with all the quantum numbers reversed.

A unique feature of quarks compared to leptons is that no “free” quark has ever been observed. This means that all current direct observations of quarks are in bound states. Most commonly, the quarks combine in pairs or triplets to form mesons and baryons, respectively. Even more complicated assemblies can be made of additional quarks, such as tetra and penta quarks, as long as all the quantum numbers are unique for each quark.

The mesons contain a quark and an anti-quark, whereas the baryons contain three quarks. Collectively, all particles constituted by any combination of quarks are known as hadrons. In 1961

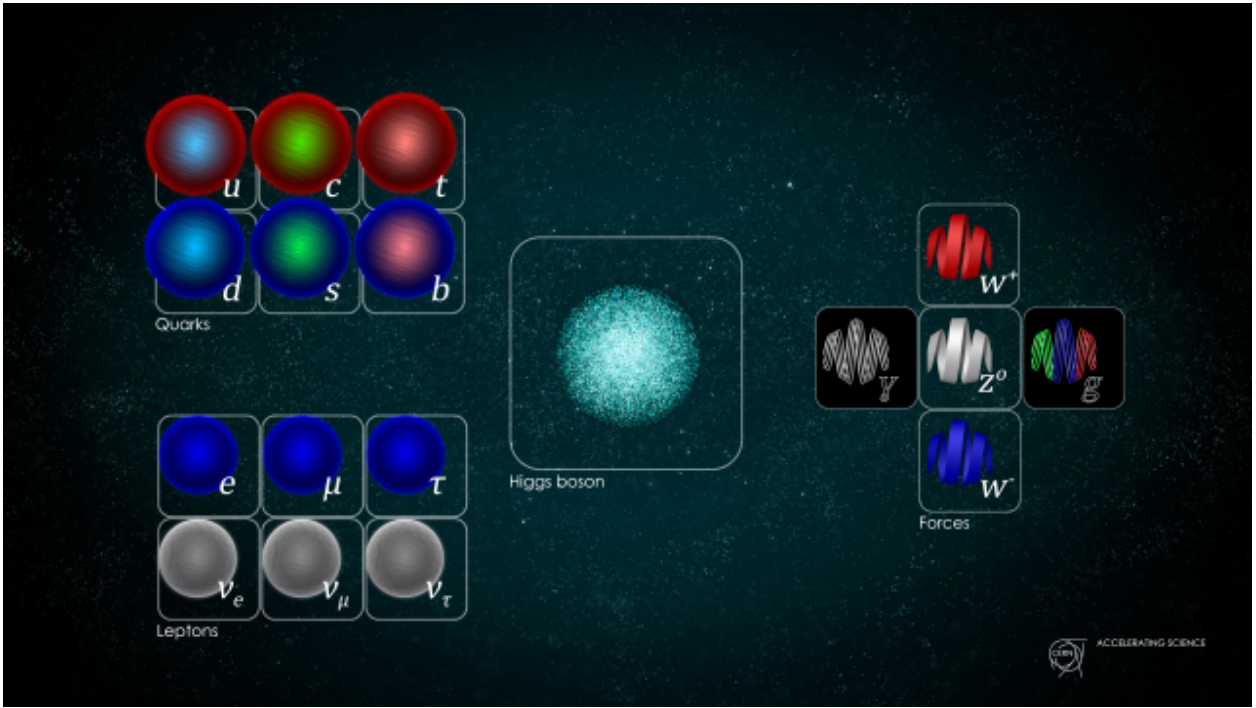


Figure 1.1: Image of Fundamental Particles in the Standard Model, taken from CERN website [1]. All known matter and particle interactions involves combinations of the particles shown here.

Murray Gell-Mann proposed his “eight-fold way” [20] which provided a method of grouping the hadrons.

Since quarks are not freely observable a common place to infer their existence (and to create heavier hadrons) are in particle accelerators. The most well known particle accelerator is the Large Hadron Collider (LHC) in Geneva. These Particle accelerators generate extremely high energy ( $\approx \mathcal{O}(10TeV)$ ) protons which when collided can generate new composite hadrons of any mass so that the total energy is conserved.

Since quarks, due to their color, readily combine to create more easily observed composite particles. The Quark model was then proposed by Gell-Mann in 1964 [21]. This model is a group theory concept (known as SU(3) symmetry) and is the means for which the fundamental particles (quarks) combine into the composite particles (hadrons) which are more readily and easily measured today. Eventually experiments conducted at the Stanford Linear Accelerator (SLAC) between 1967-1973 verified the existence of these quarks and Gell-Mann won the Nobel Prize in 1969.

The rescue of the quark model came with the measurement of [22]. The  $J/\psi$  particle indicated the existence of a fourth since then unmeasured quark, which we now know as the charm ( $c$ ).

Quark	Charge	Mass (MeV)	Year Discovered	Ref.
up	$\frac{2}{3}$	2.16	1968	SLAC [23, 24]
down	$-\frac{1}{3}$	4.67	1968	SLAC [23, 24]
strange	$-\frac{1}{3}$	93.4	1968	SLAC [23, 24]
charm	$\frac{2}{3}$	1270	1974	SLAC [22]
bottom	$-\frac{1}{3}$	4180	1977	Fermilab [25]
top	$\frac{2}{3}$	173000	1995	Fermilab [26]

Table 1.1: Description of the discovery of quarks. Notice that as the mass increases for a particular quark the year of discovery also increases. This is a property of how we create and observe the quarks in our accelerators, and also the reason why physicists continue to want to build bigger ones. Interesting physics happens at higher and higher energies, which require larger and more expensive detectors to probe these energy scales. Note that the lighter quark masses are not well understood for other experimental reasons, and the presented data are rounded to three significant figures based on [13].

## The Leptons

The leptons represent particles in the bottom left of Figure 1.1.

The first lepton discovered, and the most commonly recognized, is the electron which was discovered by J. J. Thomson. Just like the quarks, the leptons come in three families (electron,  $\mu$ ,  $\tau$ ). Also like the quarks, the leptons have charge, mass, and flavour which means they can decay.

Unlike the quarks the leptonic particles do not have a color quantum number and therefore do not combine together to create composite particles. Additionally, free leptons are observed, e.g. the electron.

The most difficult to measure fundamental particles of within the SM are the neutrinos. This is because these leptons carry no net charge. However, since they carry flavour and can decay (or be absorbed) and they also carry their respective lepton number, the neutrinos in the family can be identified by measuring their partner.

For example, a common process to observe an anti-electron neutrino ( $\hat{\nu}_e$ ) is through inverse beta-decay (IBD) following the reaction:

$$\hat{\nu}_e + p \rightarrow e^+ + n \quad (1.1)$$

Lepton	Charge	$N_e$	$N_\mu$	$N_\tau$
$e^-$	1	1	0	0
$\nu_e$	0	1	0	0
$\mu$	1	0	1	0
$\nu_\mu$	0	0	1	0
$\tau$	1	0	0	1
$\nu_\tau$	0	0	0	1

Table 1.2: Description of the quantum numbers of the fundamental lepton families. There are three unique families within the leptons: electron, muon, and tau. The charge carrier as well as the neutrino each carry a value of one for this number. Their anti-particle counterparts carry -1 of this number.

This IBD reaction is a common measurement tool for identifying neutrinos because of the distinguishable detection signature of the produced particles. The positron ( $e^+$ ) annihilates quickly ( $\approx \mathcal{O}(ns)$ ) and will produce back-to-back 511 keV photons. The produced neutron, on the other hand, wobbles around much longer ( $\mathcal{O}(us)$ ) before being captured, which produces scintillation light of energy proportional to the neutrons energy when captured.

The muon ( $\mu$ ) was discovered by Anderson and Neddermeyer in 1936 by observing cosmic ray showers [27].

The tau ( $\tau$ ) was discovered by SLAC in 1975 [28].

The first measurements of the neutrinos in each family were much harder than their charged partners. The electron neutrino ( $\nu_e$ ) and the muon neutrino ( $\nu_\mu$ ) are observed in decay interactions.

The tau neutrino ( $\nu_\tau$ ) was exceptionally difficult to measure. Like the previous neutrino partners, the  $\nu_\tau$  is discovered by looking for the creation of its partner ( $\tau$ ) during a CC interaction. As a comparison the  $\tau$  has a lifetime of only  $10^{-13}$  s whereas the muon life time  $T_\mu \approx \mathcal{O}(1\mu s)$  or seven orders of magnitude shorter!

The first successful experiment came in 2000 [29]. DONUT utilized a much more complicated emulsion detector to collect tracks from a 800 GeV proton beam offline. The exxperiment collected a total of 203 neutrino interactions, of which it found evidence for a total of only four interactions.

Force	Scale	Theory	Carrier	Ref.
Strong	10	Chromodynamics	gluon	TASSO [30]
Electromagnetic	$10^{-2}$	Electrodynamics	photon	Planck?
Weak	$10^{-13}$	Flavourdynamics	$W^\pm, Z$	CERN [32],[33]
Gravity	$10^{-42}$	General Relativity	graviton	??

Table 1.3: Relative strength chart of the four fundamental forces of nature. Although gravity is not included within the SM it is included, as well as its theoretical force carrier the graviton.

### The Forces - Vector Bosons

All forces within the standard model (electromagnetism, weak, and strong) are governed via a “carrier” particle. These carrier particles are represented on the center-right of 1.1.

The electromagnetic force is governed by particle exchanges of a photon. Other than perhaps gravity, which isn’t explained by the SM, this is the most well known and described force. All particles which carry charge interact via this force. Therefore the neutrinos are the only particles within the quarks and leptons which do not interact at all with the electromagnetic force (this is why detecting them is so hard). The full theoretical description of this force is governed by Quantum-Electrodynamics (QED).

The weak-nuclear force is governed by particles exchanges of one of the three particles in the center:  $W^\pm$  and  $Z$ . This force involves a change in flavor of a particle, and involves both quarks and leptons. It is also responsible for all decay processes. The theoretical description of these mechanics are called Quantum-Flavourdynamics (QFD).

The strong-nuclear force is governed by the exchange of the gluon ( $g$ ). This force is responsible for color changes of matter and describes why nuclei are held together. Since this force only involves exchanges of a gluon, the leptons are therefore unaffected since these particles carry no color quantum number. The full theoretical description for the strong-nuclear force is Quantum-Chromodynamics (QCD).

The gluon was discovered in at the TASSO experiment 1979 [30, 31].

Measurements of the intermediate bosons were much harder. The  $W^\pm$  boson were measured in 1983 [32]. Followed by the  $Z$  boson which was measured shortly afterwards in the same experiment [33].

## The Higgs - Scalar Boson

The last particle to be discovered in the SM was the Higgs particle. The Higgs particle was originally predicted in 1964 by Peter Higgs [34]. This particle is important to describe how mass is given to the elementary particles described by the SM. Finally, in 2012 the Large Hadron Collider (LHC) was able to infer the massive Higgs particle [35].

### 1.2 The Problem: Moving Beyond the Standard Model

Despite its (SM) numerous achievements in predictive power and experimental verification we know today that it has crucial shortcomings. The Standard Model (SM) [17–19] has no ability to account for Dark Matter or Dark Energy in the universe, nor the distribution (or the hierarchy) of neutrino masses, nor is it able to relate how gravity interacts with the other fundamental forces of nature (Unification). It also doesn't account for some 'basic' properties it has, such as: why are there only three generations of leptonic particles (electron, muon, and tau)? These short-comings offer hints for where to search for physics. Physicists have known about these short comings from the conception of the Standard Model and have (to no avail) sought out what's next.

With a plethora of hints to search for New Physics (NP), it can be useful to organize the efforts of search. In 2008 the Particle Physics Project Prioritization Panel (P5) did just this and labeled the three frontiers of physics: the cosmological, energy, and intensity frontiers. Each of these frontiers offer different kinds of challenges and serve as guides to look for physics beyond the SM.

### Searches at High Energy

The energy frontier is concerned with the origin of mass. The Large-Hadron Collider (LHC) [35] experiment is the archetypal experiment aimed at solving problems within this frontier. The LHC itself consists of other large-scale tracking and calorimetry experiments such as ATLAS [36] and CMS [37].

Large particle accelerators are used to generate source particles of ever increasing energy. Due to the conservation of mass, the higher the energy of the particle accelerated the higher the mass (energy) of the particles created after certain collisions can be.

There also exist lepton colliders [38] which offer unique areas of search along this frontier too. More detailed descriptions of such collider experiments are beyond the scope of the work presented here, and further reading may be pursued from the extremely detailed technical design reports cited here of Belle-II and the ATLAS experiments.

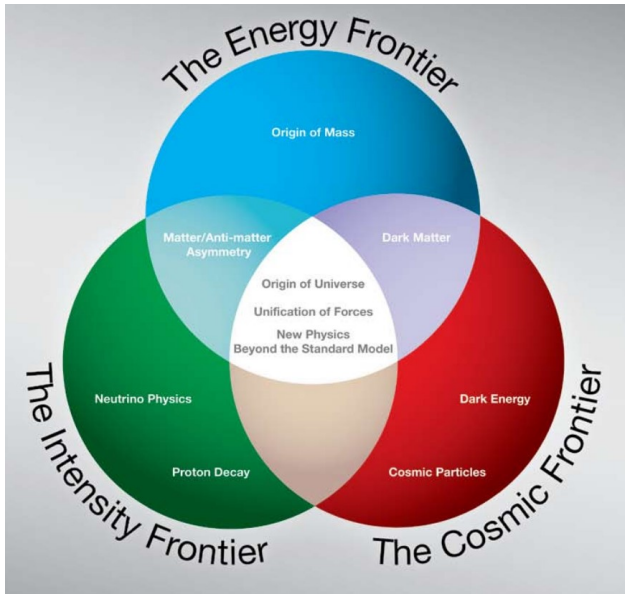


Figure 1.2: Image based on the 2008 P5 report [2]. The white text labeled within each frontier describes the search for some physics beyond the SM within that frontier.

## Other Searches

The cosmological frontier aims to search for NP on extremely large time and distance scales by relying on observational techniques. Cosmological measurements have shown that majority of the universe's matter is not visible to light, and so we call it dark matter. Additionally, the universe is expanding at an accelerated rate, which we can tell from the blueshift of distance galaxies. Likewise, cosmologists have also discovered that the universe is expanding due to some invisible energy in the universe, and so we call it dark energy.

The search for these dark causes of the universe lie within the realm of the cosmological frontier.

Dark energy currently resides as the explanation for the observed accelerated expansion of the universe. Dark matter is commonly used to explain the deviation of the rotational frequency of galaxy clusters.

The third (and final) frontier we'll discuss is the Intensity frontier. The Intensity Frontier of Physics ([2]) is one which today requires very large and very precise measurements to gain the statistics to declare an observation. In order to address the issues posed within this frontier the large scale detectors hunting for New Physics (NP) have continued to grow in size, energy sensitivity, and importantly cost: [39].

As compared to the energy frontier which normally relies on creating new particles from accelerators

the Intensity Frontier often searches for rare events, like a proton decay.

Neutrino searches also lie within this frontier. Neutrinos are notoriously difficult to detect and measure since they can only be probed via the weak-nuclear force, and even then only indirectly since they carry no charge themselves.

### How did we get here?

Many times since the early 20th century it was thought that the goal of physics was accomplished. However, during each of these moments of false triumph some new detector was built to take a new measurement; thus, the door to new understanding of nature is never closed. This section provides a brief and (necessarily) incomplete history of significant measurements and detector developments relevant to particle physics in the creation of the SM. In order to clear an obstacle, it is often helpful to remember the previous ones.

### A Century of New Physics

At the turn of the 20th century particle physics was in its infancy. In 1900 Max Planck first introduces the concept of energy quanta for the first time concerning photons to eliminate the infamous ultra-violet catastrophe problem introduced by statistical mechanics. JJ Thomson used a single cathode-ray tube to discover the electron and the nucleus, and won for himself the Nobel Prize in 1906. Milikan's famous oil-drop experiment won him the Nobel Prize in 1923.

However, as each of these new discoveries solved problems only more questions were produced. Once the nucleus was discovered to contain only protons and neutrons, the natural question arose: what holds all of the positive charge together in the center. Thus, physicists cleverly named the new force which was stronger than the electromagnetic force: the Strong Force.

The bubble chamber was then invented in 1952 by Donald Glaser [40]. These detectors proved significant in the discover of the W and Z bosons and ultimately allowed the unification of the electromagnetic and weak forces to form the electroweak theory.

Next the spark chamber eventually lead to the gradual development of the wire-spark chamber. In 1968 Georges Charpak developed the Multi-Wire Proportional Chamber (MWPC) for which he (much later) won the Nobel Prize in 1992. From this key insight a new detector concept was made possible.

### Finding Neutrinos

Hints at the existence of neutrinos began early last century. More than 100 years ago Chadwick was able to show that the energy spectrum from a decaying electron was continuous [41]. This unknown cause of the spectrum even lead some physicists to belief that perhaps the conservation of energy was violated. Wolfgang Pauli instead predicted a particle which he originally called the neutron to also be a decay product, but not easily observable. This third particle in the decay would explain the energy spectrum of the electron. Quickly however the particle name neutron was taken by a different neutral particle in 1932 [42] The discovery of the neutron and the continuous spectrum of beta decay forced Pauli to come up with a new theory attempting to describe beta decay [43].

Originally physicists held little hope that such an elusive particle would ever be detected. However, the motivation to save this conservation law lead Wolfgang Pauli to the first prediction (1930) of the neutrino; the reason that the energy was a spectrum from the electron was that some of the energy was “taken up” by the neutrino. Finally, some 26 years later in 1956 was the first observation of the electron neutrino [44].

The discovery of the electron neutrino  $\nu_e$  was the first of the three families to be discovered. A few years later the first reactor neutrino ( $\nu_\mu$ ) was observed at Brookhaven National Laboratory (BNL) [45].

The first measurement of the  $\tau$  neutrino ( $\nu_\tau$ ) happened much later in 2001 [29]. this detector used nuclear emulsions.

Daya Bay [46] has also established measurements of electron anti-neutrino ( $\bar{\nu}_e$ ) disappearance.

After this first discovery is when the answers, followed by more questions, came. Since then, many large-scale experiments have been dedicated to measuring the three generations of neutrinos. [46–53]

All reliable information we have about neutrinos come from these large scale detectors.

Originally the mass of the neutrino predicted by the SM was massless. That was until the Solar-neutrino anomaly measured significantly less neutrinos than predicted [54]. The solution for this was oscillation.

### 1.3 Modern Tracking Detectors

It could be said that any definition defining a “new” age of a types of detectors is subjective. Nevertheless, we proceed to define that modern particle detectors were the age that began to use modern electronics, or electronics after the development of the metal–oxide–semiconductor field-effect transistor (MOS-FET). If there was any invention which was able to drive the development of

computers and measuring electronics, it was the transistor. Therefore, the beginning of the modern particle detection age began with the transistor, and it saw to the end of the spark chamber and bubble chamber detectors.

### **Multi-Wire Proportional Chamber**

The middle of the 20th century saw a dramatic increase in the ability and reduction of the cost of electronics. These (then) new electronics allowed for fast digitizing measurements of voltage or current. Thus, new proportional counter detectors were capable of using computers to do the measuring or counting of the events within the detector. The rate at particles could then be detected increased by orders of magnitude.

Using the fast digitizers and closely spaced wires Georges Charpak (1924-2010) created the first-Wire MWPC in 1968 [55]. This new detector was one which paved the way for modern detector development, for which Charpak won the 1992 Nobel Prize.

### **Time Projection Chambers**

Time Projection Chambers (TPC) [56] have been shown to be extremely useful in high energy physics experiments due, in part, to their high resolution in both timing and spatial dimensions. This detector was originally used in the Position-Electron Project PEP-4 experiment which measured electron-positron collisions from the 29 GeV electron beam produced at the Stanford Linear Accelerator (SLAC). The first TPC design used high pressure gas and was able to measure 1000s of particle tracks per second (compared to 1-10) and provide full 3-D event reconstruction.

It did not take long for other experimentalists to generalize this concept to different elements or even to liquid.

### **Noble Gases and Time Projection Chambers**

The technology of TPCs has greatly matured since their original inception. in many kinds of detectors across HEP. TPCs can also incorporate two phases of a substance (liquid and gas), called Dual Phase (DP) TPCs.

the Xenon-1T is a dark matter experiment which is a dual-phase TPC [57].

The LUX experiment is a single phase TPC also hunting for dark matter.

A specific kind of TCP is a Liquid Argon Time Projection Chamber (LArTPC) [58].

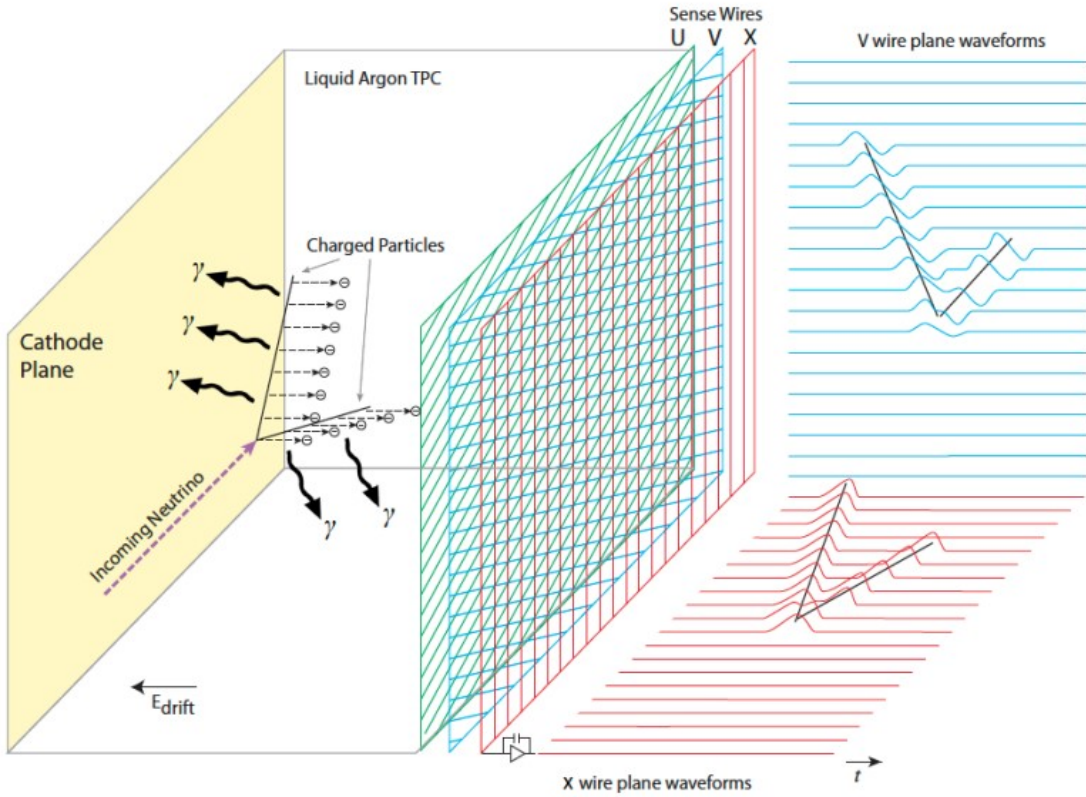


Figure 1.3: Image of a Time Projection Chamber (TPC). Charge is accumulated within the volume as ions are removed from the fiducial volume from another charged ion as it passes through the material. An uniform electric field drifts the free now electrons towards the anode plane. The collection and readout of charge on this anode plane is what is recorded within the detector. Image is taken from [3].

Recent work on LArTPCs ([59–61].)

Energy resolution of the LArTPCs within DUNE are still unknown to within a factor of 4 [62].

## 1.4 Ways Forward

Despite the passing of generations of detectors and developments in electronics the SM remains. For nearly 50 years now the SM is still our best model at describing nature as we know it, despite also knowing that there must be more. Here in this section we describe in some more detail current searches at the intensity frontier where physicists are looking to go beyond the SM.

We give special attention to neutrino oscillation at the end of this section since later chapters

Property	Symbol	Value	Unit
Density	$\rho$	1.3973	$gcm^{-3}$
Fano Factor	$F$	0.107	-
Dielectric Constant	$\epsilon$	1.505	-
electron drift velocity	$v_e$	0.1601	$cm/\mu s$
Ionization Energy of single $e^-$	$W_i$	23.6	$eV/e^-$
Ionization Energy of single $e^-$ from photon	$W_{scint}$	19.5	$eV/\gamma$
Minimum Specific energy loss	$(dE/dX)_{MIP}$	2.12	$MeV/cm$
Hadronic Interaction Length	$\lambda_{int}$	85.7	cm
Scintillation Emission Wavelength	$\lambda_{scint}$	128	nm
Longitudinal Diffusion Coeffecients	$D_L$	6.6270	$cm^2/s$
Transverse Diffusion Coeffecients	$D_T$	13.2327	$cm^2/s$

Table 1.4: Relevant Liquid Argon parameter information. Values are taken from [14], with temperature  $T_s = 87K$  and electric field  $E_f = 0.5kVcm^{-1}$ .

simulation studies will be based off results hoping to measure this effect.

## Hadron Decay

Does a proton decay? This is the fundamental question for physicists studying hadron decay. The SM predicts that the proton itself is stable, so it should never decay. Therefore, the search for proton decays offers a path for physics beyond the SM. Attempts to unify all the fundamental forces of nature into a unified theory are called Grand Unified Theories (GUTs), and according to many GUTs, the proton does indeed decay.

Current measurements on the proton lifetime indicate that its lifetime is on the order of magnitude (or above)  $10^{34}$  years. Even at its most frequent, this is an exceedingly rare event considering that the lifetime of the universe is  $\approx \mathcal{O}(10^{10} yrs)$

Since these events are so rare, extremely large detectors with large numbers of protons inside of them are required to constantly observe many protons. An example of a second generation proton decay studies is the Imaging Cosmic and Rare Underground Signals(ICARUS) experiment [63].

There are at least two prominent decay chains that are expected to be dominant, depending on the Grand-Unification-Theory (GUT) that hopes to go beyond the SM. The first one is:

$$p^+ \rightarrow e^+ + \pi^0 + 2\gamma \quad (1.2)$$

This interaction is easily detectable in cherenkov based detectors due to the emission of both the gammas as well as the high energy of the emitted positron. In fact, the worlds best estimate for proton lifetime comes from this decay-chain [64].

Other Supersymmetric GUT models predict instead [65]:

$$p^+ \rightarrow K^+ + \nu \quad (1.3)$$

In this case the Kaon is generally moving too slow to be measurable by cherenkov detectors. However, a TPC style detectors are still sensitive to its signature charge deposition. This is an interesting reaction since the worlds best limits are currently provided by the Super-Kamiokande experiment, which is itself a cherenkov based detector in water.

These searches are interesting, if albeit difficult, both due to the rareness of such an event. If any detector was able to clearly measure even a single proton decay, that would provide direct evidence for physics beyond the SM. Future detectors that will continue to probe for nucleon decay are DUNE, Hyper-Kamiokande, and JUNO [3, 39, 66].

## Supernova Studies

A supernova occurs when a massive star runs out of the necessary elemental fuel for fusion at its core. When this happens the inward pull of gravity due to the mass of the star overcomes the reduced outward pressure from the nuclear fusion.

It has been nearly 30 years since the last observed neutrinos from a galactic core collapse supernova, SN 1987A [67]. Sensitivity to supernova neutrinos is crucial for understanding the mechanisms that govern particles at these extreme densities and pressures. Interestingly, because neutrinos are so weakly interacting, it is possible to observe their signature and arrival before the photons arrival of a Type-II supernova.

The principal interaction chain observable in a TPC is:



A LArTPC is sensitive to  $\nu_e$  by measuring the signature of both the  $e^-$  and  ${}^{40}Kr^+$ .

## Neutrino Oscillation

Another possible route beyond the Standard Model is the detailed study of neutrinos.

Here we provide a general description of a model to describing neutrino oscillation. We elucidate the measurable parameters which govern this oscillation and describe how these values are currently measured in experiments today.

Of all known particles the most elusive (hardest to detect and measure) is the neutrino. For this reason the least is known about the neutrino. What we do know about the neutrino is there are three flavors each associated with their leptonic partners: the electron, muon, and tau.

Tokai to Kamioka (T2k) [68] has well established neutrino oscillation measurements.

It came as a welcome shock that neutrino oscillation was first measured. This oscillation indicates that a neutrino as it moves through space can change its state; a electron neutrino can oscillate into a muon neutrino or even a tau neutrino. This happens because the mass eigenstate and flavor eigenstates which govern the neutrino are not equal.

The standard notation which relates the mass eigenstates ( $\nu_i$ ) and flavor eigenstates ( $\nu_\alpha$ ) ,

$$\nu_i = U_{i\alpha} \nu_\alpha \quad (1.5)$$

$$\begin{pmatrix} \nu_e \\ \nu_\mu \\ \nu_\tau \end{pmatrix} = \begin{pmatrix} U_{e1}, U_{e2}, U_{e3} \\ U_{\mu 1}, U_{\mu 2}, U_{\mu 3} \\ U_{\tau 1}, U_{\tau 2}, U_{\tau 3} \end{pmatrix} \begin{pmatrix} \nu_1 \\ \nu_2 \\ \nu_3 \end{pmatrix} \quad (1.6)$$

The matrix elements within  $U_{li}$  represent the mixing coefficients and are used to calculate the probability that a certain neutrino will oscillate from one family to another. We identify  $U_{ij}$  as the

commonly known  $U_{PMNS}$  matrix, where PMNS stands for: Pontecorvo–Maki–Nakagawa–Sakata, or the four theorists who helped developed this convention. Luckily, there are not a total of nine free parameters within the SM that determine this. The  $U_{PMNS}$  matrix can be additionally rewritten following [69, 70] as:

$$U_{PMNS} = U_{sol} \times U_{rea} \times U_{atm} \times U_{maj} \quad (1.7)$$

After expanding the matrix representations, equation 1.4 becomes:

$$U_{PMNS} = \begin{pmatrix} 1 & 0 & 0 \\ 0 & C_{23} & S_{23} \\ 0 & -S_{23} & C_{23} \end{pmatrix} \times \begin{pmatrix} C_{13} & 0 & S_{13}e^{-i\delta_{CP}} \\ 0 & 1 & 0 \\ -S_{13}e^{-i\delta_{CP}} & 0 & C_{13} \end{pmatrix} \times \begin{pmatrix} C_{12} & S_{12} & 0 \\ -S_{12} & C_{12} & 0 \\ 0 & 0 & 1 \end{pmatrix} \times \begin{pmatrix} e^{i\alpha_1} & 0 & 0 \\ 0 & e^{i\alpha_2} & 0 \\ 0 & 0 & 1 \end{pmatrix} \quad (1.8)$$

We identify above the additional matrix components where historically these values are measured. Therefore, instead of nine unknown parameters for the SM, there are only six. The components  $C_{ij}$  and  $S_{ij}$  in the matrices are defined to be  $\cos(\theta_{ij})$  and  $\sin(\theta_{ij})$ , respectively.

Then, the six parameters of the  $U_{PMNS}$  are identified as:

- $\theta_{13}$ , reactor measurements.
- $\theta_{12}$ , atmospheric measurements.
- $\theta_{23}$ , solar measurements.
- $\delta_{CP}$ , Charge-conjugation parity violation.
- $\alpha_1/\alpha_2$ , The two Majorana Phase parameters.

The Majorana phases ( $\alpha_i$ ) are sensitive in experiments that can detect the Majorana nature of neutrinos such as neutrinoless double beta decay. In neutrino oscillation measurements, these phases cancel out and are not measurable. Therefore, we ignore these two phases for the remainder of this work.

Next we demonstrate the calculation of the probability of oscillation from one mass eigenstate to another. Namely we calculate the probability  $P(\mu \rightarrow e)$  which is the probability of interest in

a long beamline experiment. First we identify that equation 1.4 can be rewritten to isolate the flavor-eigenstate terms ( $\nu_\alpha$ ) by multiplying by the adjoint of the PMNS matrix ( $U_{PMNS}^*$ ). Then the relationship between the mass and flavor eigenstates become:

$$\nu_\alpha = U_{PMNS}^* \nu_i \quad (1.9)$$

The value of interest is  $P(\mu \rightarrow e)$ . The probability to end up in state  $\nu_e$  beginning from  $\nu_\mu$  is:

$$P(\mu \rightarrow e) = |\langle \nu_e | \nu_\mu \rangle|^2 \quad (1.10)$$

We then use equation 1.4 to represent the matrix elements of  $U_{PMNS}$  from  $\nu_e$  and  $\nu_\mu$  to obtain:

$$P(\mu \rightarrow e) = \left| \sum_i U_{ei} U_{\mu i}^* e^{-iE_i t} \right|^2 = \sum_i |U_{ei} U_{\mu i}^*|^2 + 2\Re \left( \sum_{i>j} U_{ej}^* U_{\mu j} U_{ei} U_{\mu i}^* e^{-i\Delta_{ij} t} \right) \quad (1.11)$$

Where we identify that the cross terms introduce a phase difference shown as  $\Delta_{ij}$  in the second term in equation 1.4. This represents the neutrino oscillation term and represents the difference in the mass states of the neutrinos:

$$\Delta_{ij} = (E_i - E_j) \quad (1.12)$$

The energy of the neutrino in each state can be approximated to first order following:

$$E_i = \sqrt{p^2 + m_i^2} \approx p + \frac{m_i^2}{2p} \quad (1.13)$$

The momentum of all of the mass eigenstates is the constant. Then oscillation parameter becomes:

$$\Delta_{ij} \approx \frac{1}{2p} (m_i^2 - m_j^2) = \frac{\Delta m_{ij}^2}{2p} \quad (1.14)$$

Finally, the last two parameters which govern the neutrino oscillations are identified as the mass differences between the three mass states. Now, the frequency of the oscillation between neutrino

## Neutrino Mass Hierarchy

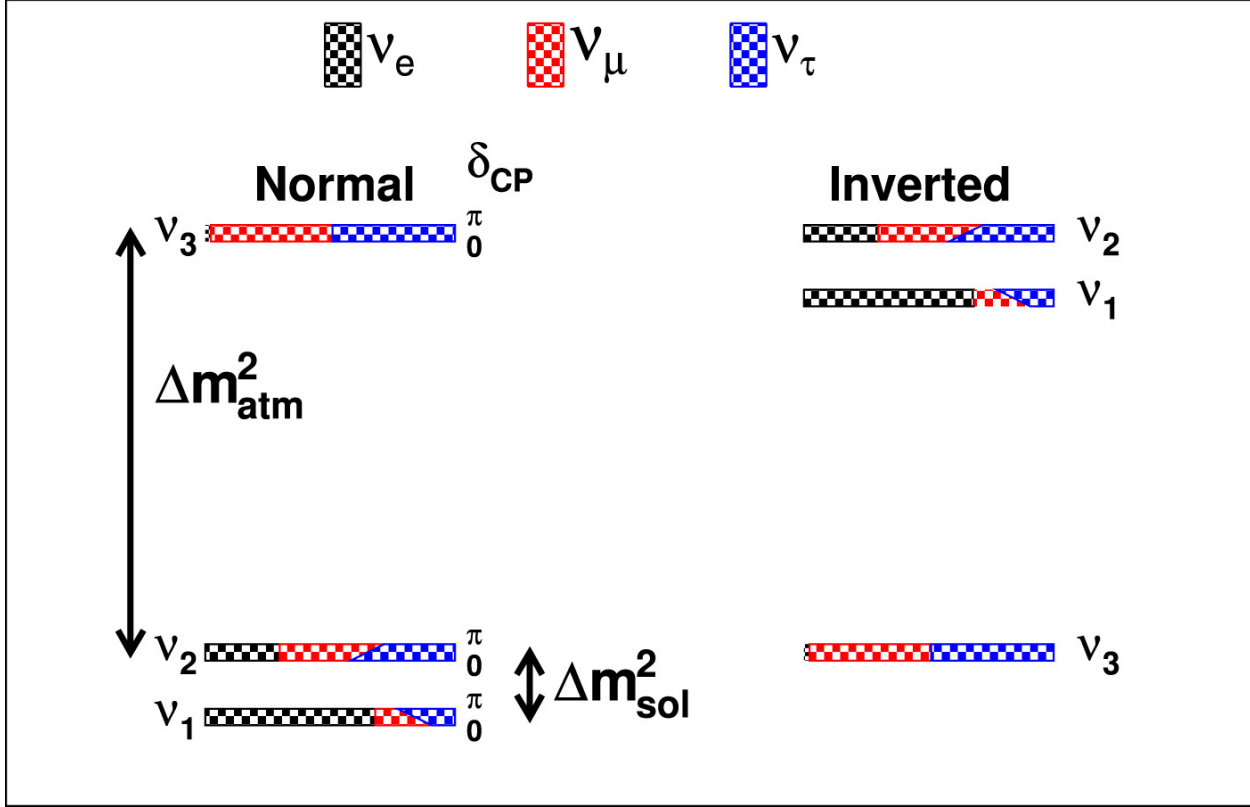


Figure 1.4: Representation of the mass hierarchy scales. This is a representation of the two possible orderings of neutrino masses, due to the uncertain sign of  $m_{13}$ . It is also interesting to observe that the absolute mass scale is not measured since oscillation measurements only give difference mass squares. Image was taken from [4].

states depends on the difference of the square their masses ( $\Delta m_{ij}^2$ ), where three neutrino masses imply two independent differences. The mass differences provide two additional parameters are needed to fully describe neutrino mixing. The six values of interest and their current best known fits are shown in Table 1.4:

The the sign of  $m_{13}$  is unknown. This leads to two possible ordernigs of the masses, known as normal and inverted, NO and IO respectively. The normal ordering indicates that the masses of the neutrinos follow the ordering of their charged partners. That is, NO implies a mass ordering of:  $\nu_e < \nu_\mu < \nu_\tau$ . Whereas, the IO has a mass ordering:  $\nu_\tau < \nu_e < \nu_\mu$ .

Neutrino oscillations in matter are slightly different than those in vacuum [71]. The Mikheyev-

Paramater	Best Fit	Unit	Best Soruce
$\theta_{13}$	$8.57^{+0.12}_{-0.12}$	na	Reactor
$\theta_{12}$	$33.44^{+0.77}_{-0.74}$	Atmospheric	
$\theta_{23}$	$49.2^{+0.9}_{-1.2}$	na	Solar
$\delta_{cp}$	$197^{+27}_{-24}$	na	Atmospheric+Accelerator
$\Delta m_{21}^2$	$7.42^{+0.21}_{-0.20}$	$10^{-5} eV^2$	Solar
$\Delta m_{31}^2$	$2.517^{+0.026}_{-0.028}$	$10^{-3} eV^2$	Atmospheric

Table 1.5: Known Oscillation Parameters of Interest. Values are taken from the global fit [15]. The values shown assume normal mass ordering for neutrinos and include atmospheric Super-Kamikonde Data.

Smirnov-Wolfenstein (MSW) effect [72] also contributes to differening neutrino oscillations as they move through matter of varying density, which additionally complicated the calculation. The MSW effect also affects neutrinos differently than anti-neutrinos, which is useful for measuring  $\delta_{cp}$ . This resonance affect for beam-line experiments affects  $\nu_e$  in the case of normal mass ordering (NO), whereas in the case of inverted mass order (IO), the  $\hat{\nu}_e$  experiences resonance and is thus more likely.

## 1.5 Neutrino Tracking Detectors in the Current Century

Finally, in this last section we discuss the development of various upcoming detector technologies. There are many motivating pressures for new detectors to adopt pixelated designs. Below we discuss two contributing factors: the development of electronics and computing algorithms.

First, previously pixelated detectors have historically been more difficult because of the issues of cost and size regarding the number of readout channels. This is being addressed, in part, by the advent of newer, cheaper, and larger Field-Programmable-Gate Arrays (FPGAs). One method for reducing the electronic overhead required in pixelated detectors is to use digital multiplexing. Cheap, high channel FPGAs directly solve this problem. Other electronics development, such as the Silicon-Photomultiplier, offer much cheaper alternatives for large pixel counters compared to their historical counter-parts.

Paramater	Best Experiments	Type of Detector
$\theta_{13}$		
$\theta_{12}$		
$\theta_{23}$		
$\delta_{cp}$		
$\Delta m_{21}^2$		
$\Delta m_{31}^2$		

Table 1.6: Comparison of which type of detectors are useful for measuring which values of neutrino oscillation.

## 1.6 Future Detectors

[73] Another driving factor is the the development of Machine Learning (ML) algorithms, particularly Convctional Neural Network (CNN [74]). Recent industry has driven the need for CNNs to be able to correctly identify and label 2-D images of various kinds, and thus championed much of progress in this field and spawned many kinds of CNN algorithms.

Recently, it has been shown how these kinds of algorithms extend into High Energy Physics (HEP) for particle identification. A major issue at the Intensity Frontier of physics is the sheer amount of data to store and process. These ML algorithms provied a developed tool to automate the analysis of huge amounts of data ( $>> 1TB$ ) and have been shown to be quite accurate ( $> 99\%$ ) at particle identification in LArTPCs.

Additional work has been performed in recent years which show that LArTPCs can also utilized a pixel-based readout [75], [76].

The end of the Standard Model era is inevitable. SM simply fails to account for physics with all major frontiers for physicists to accept its completeness; we know there is much and more to learn about nature.

The 20th century saw unprecedeted progress in its sophistication of its detectors from ray tubes, to spark chambers, to proportional counters, and to huge ( $>20$  km) particle accelerators. This century shows no signs holding any less promise than its predecessor. Continued development in electronics, computing, and analysis methods will lead to more and newer frontiers of physics.

The work presented in this introduction aims to not only encapsulate the massive progress particle physics has made since the electron's discovery, but also to server as a reminder of how extraordinarily surprising nature is. At every turn and at every point where physicists think they've arrived at

the end (or at an impossible roadblock) there always remains more to discover. If we have learned anything, we have learned to knock and the door shall be opened.

## The Deep Underground Neutrino Experiment

The Deep Underground Neutrino Experiment (DUNE) is a long-baseline neutrino beam experiment [3, 7, 12, 77]. DUNE, when constructed, will be composed two detectors, a near detector (ND) and a far detector (FD) which are separated by a distance of 1300 km.

The ND is located at Fermilab and its purpose is to characterize the source neutrino beam created there. The ND serves many purposes. To name a few..TODO

The FD will be placed underground at Sanford Underground Research Facility (SURF) and be approximately 1300 km away from the ND. This detector represents an enormous engineering challenge to place such large, cold, and complicated detector. The FD will be composed of up to four separate 10 kiloton modules.

DUNE plans to offer an incredibly rich searches across the sectors listed above 1.6. We briefly discuss the relevance of some the searches below, but more detailed reading can be pursued at [12].

Two of these four modules at least will use a known wire-based readout technology and a vertical drift-readout. The two remaining modules are considered modules of opportunity and their readout technology is yet unknown. A purpose of this dissertation is show the viability of a novel readout technology.

DUNE has three main science goals, all of which are geared towards pushing beyond the standard model:

- Hadron Decay 1.4
- Core-collapse Supernovae 1.4
- Neutrino Oscillation 1.4

We will discuss the relevance of each of these items, and in chapter 2 where we will further discuss how the work presented here relates to each of these topics.

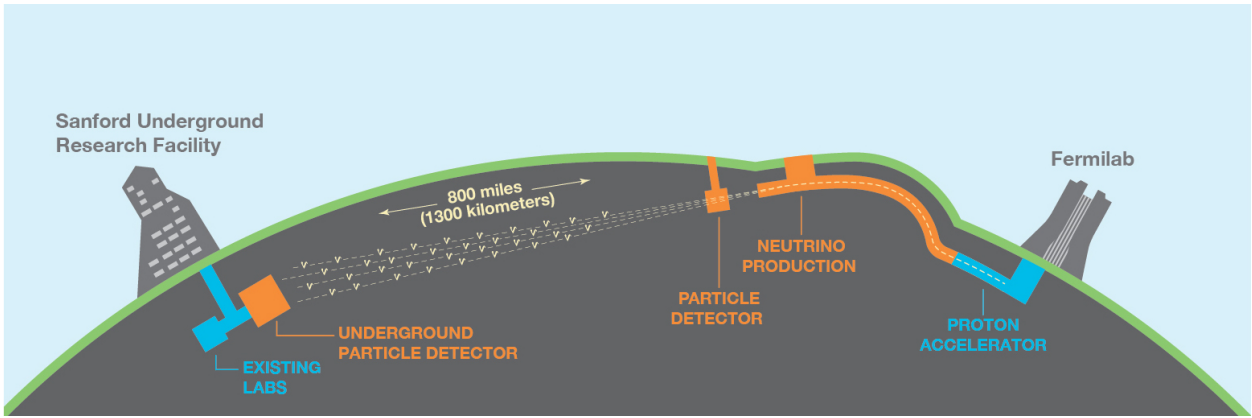


Figure 1.5: Representation of the Near and Far Detectors for the DUNE experiment. The Near Detector is located within the image labeled as the Particle Detector. One of the key purposes for the Near Detector is to tag outgoing particles from the proton beam. Image was taken from [5].

Conventional horizontal drift detection for foreseeable DUNE modules are already considered possible for lengths up to 6.5m [78].

## *Chapter 2*

# A NOVEL READOUT TECHNIQUE FOR TPCS: Q-PIX

We begin this chapter in Section ?? by introducing a novel pixel-based readout concept for TPCs. Pixel-based readouts offer several advantages over the traditional wire readout [79]. A key improvement offered by pixelization is true 3-D image reconstruction. This allows for sharper vertex reconstruction, improving the overall resolution of a LArTPC and may reduce the time required for a NP measurement. Other benefits include a reduction in the amount of data storage required and there simpler data analysis.

Next, in Section 2.2 we discuss how this readout technology can be extended to a DUNE-FD 10 kT module. We compare the design specifications for the current wire-based readout of a DUNE-FD and discuss how the Q-Pix readout can meet similar design goals. We note the advantages of pixelization come at the cost of increased design complexity. The traditional wire-based readout of a DUNE-FD module will have hundreds to thousands of channels, while a pixel-based readout will have tens of millions of channels. This number of channels required to provide a stable readout over the expected lifetime of DUNE ( $\approx 20$  years), where the electronics are continuously operating at liquid argon temperatures. A goal of this dissertation is to address the channel size problem.

Two prototype ASICs have been developed to test each side of the readout shown in Figure 2.1. We refer to the ASIC developed to test the front-end as the "analog ASIC". Likewise, we refer to the ASIC developed to test the back-end as the "digital ASIC". The contributions to the design of digital ASIC is a major component of this thesis. In Section 2.3 we discuss the design challenges of a large pixelated detector, with a special emphasis on the requirements of the digital back-end. Finally, in Sections 2.4 and ?? we briefly describe other work towards validating the Q-Pix design in a LArTPC.

## **2.1 Q-Pix: The Circuit Level Design**

The fundamental Q-Pix circuit (2.1) was first introduced by Nygren and Mei [6]. The principle of the front-end circuit operates on producing a signal output from Schmitt trigger connected to a charge sensitive amplifier (CSA) circuit. The CSA's input is connected to the anode of a TPC

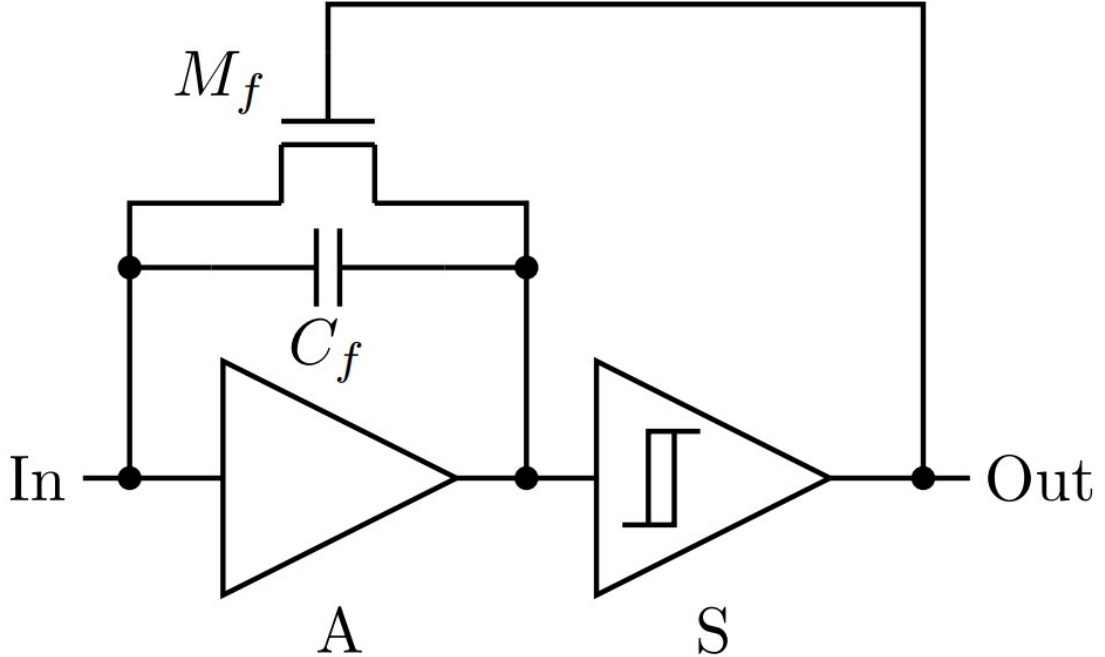


Figure 2.1: A simplified schematic of front-end Q-Pix Readout circuit. The front-end is a charge sensitive amplifier (CSA) whose output is connected to a Schmitt trigger. The trigger (output) occurs when enough charge as accumulated on the capacitor  $C_f$  (currently 1 fC). One of the design parameters for the Q-Pix front-end is the choice of  $C_f$ . This front-end circuit is designed within a single analog ASIC which has contains 16 of these circuits. The schematic for this ASIC is shown in Appendix B. Image is taken from [6].

where drifted electron charge accumulates. Voltage is then built up across the capacitor from the accumulating charge according to the equation:

$$Q_i = C_i V_i \quad (2.1)$$

After the capacitor voltage exceeds a set threshold ( $V_i$ ) the schmitt trigger activates. The Schmitt trigger output is sent as a signal input to the digital logic to be recorded. This signal is shown as the output in Figure 2.1. The Schmitt trigger input to the digital back-end is recorded against a free running local oscillator ( $f_o = 30$  MHz ).

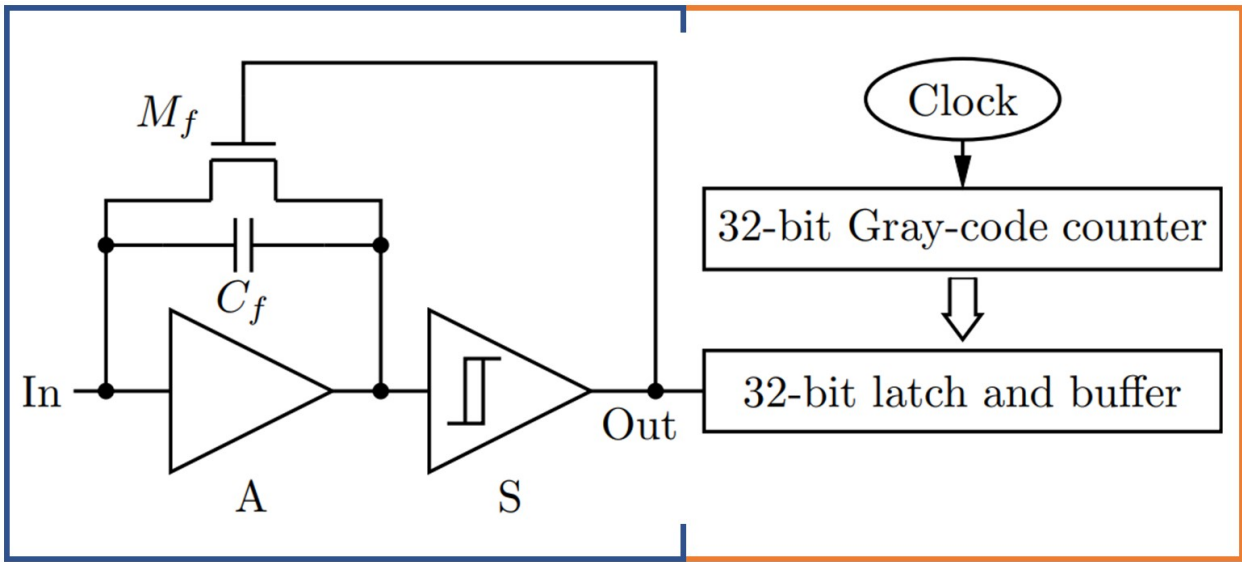


Figure 2.2: A modified image from ?? is shown. The blue box is the Q-Pix circuit (Figure 2.1), which we refer to as the Q-Pix "analog front-end". The right side of the image, encompassed in orange box, we refer to as the "digital back-end". The back-end is responsible for providing the local oscillator as well as accurately recording a reference counter to correspond to the time when the Schmitt trigger signal is received.

The Q-Pix readout records 32-bit latch values as a response to the Schmitt trigger output; it does not measure voltage, charge, or time. We refer to this 32-bit measurement as a "timestamp". These timestamps are produced when enough charge accumulates on the capacitor to produce a reset pulse, therefore the Q-Pix readout does not depend on an external system trigger to acquire data.

There are two components of the Q-Pix readout: analog and digital. The analog portion of the readout begins with the CSA and ends at the Schmitt trigger output. The digital portion of the readout begins at timestamp record. These two portions are shown in Figure 2.1.

## Current Reconstruction

Here we describe the basic principle of reconstructing the input current from a collection of timestamp measurements.

A timestamp measurement indicates that a certain amount of charge was accumulated at the CSA. Since total charge is conserved we can say that the total accumulated charge ( $Q_{in}(t)$ ) is equal to the total

amount of charge discharged from each reset ( $Q_{out}(t)$ ) plus any residual charge still on the pixel ( $Q_c(t)$ ). Therefore, we can relate the total accumulated charge to the total charge discharged with the following equation:

$$Q_{in}(t) = Q_{out}(t) + Q_c(t) \quad (2.2)$$

One of the features of the analog ASIC is the replenishment circuit. This circuit is a constant current source which can remove a constant number of electrons from the CSA. This provides a major simplification to the current reconstruction. If we assume that each reset removes the same amount of charge ( $Q_o$ ) we can rewrite the total charge out ( $Q_{out}$ ) in terms of the integer number of resets at time t, ( $N(t)$ ):

$$Q_{out}(t) = Q_o N(t) \quad (2.3)$$

Equation 2.1 then gives us the measured current by definition ( $I_{out} = \frac{dQ_{out}}{dt}$ ):

$$I_{out} = \frac{d}{dt}(Q_o N(t)) = Q_o \frac{dN}{dt} \quad (2.4)$$

We identify  $\frac{dN}{dt}$  at the number of resets per unit time. We can calculate the average current between two resets, or  $\frac{dN}{dt} = \frac{1}{dT}$ . Then,  $dT$  is the time difference between two resets and is measured at the local oscillator:  $dT = \frac{f_o}{N_{rtd}}$ , where  $N_{rtd}$  is the difference between the two timestamps. Equation 2.1 becomes:

$$I_{out} = \frac{Q_o f_o}{N_{rtd}}$$

(2.5)

Equation 2.1 shows the fundamental equation for the Q-Pix readout reconstruction. There are three important parameters: the charge per reset ( $Q_o$ ), the frequency of each local oscillator ( $f_o$ ), and  $N_{rtd}$  which is the difference between two timestamp measurements. Figures which demonstrate the transistor level effects of this reconstruction are shown in Figure 2.1 and Fig. 2.1. Figures section 2.1 show the charge reconstructions with a  $Q_o$  value of 1 fC and 0.3 fC, respectively.

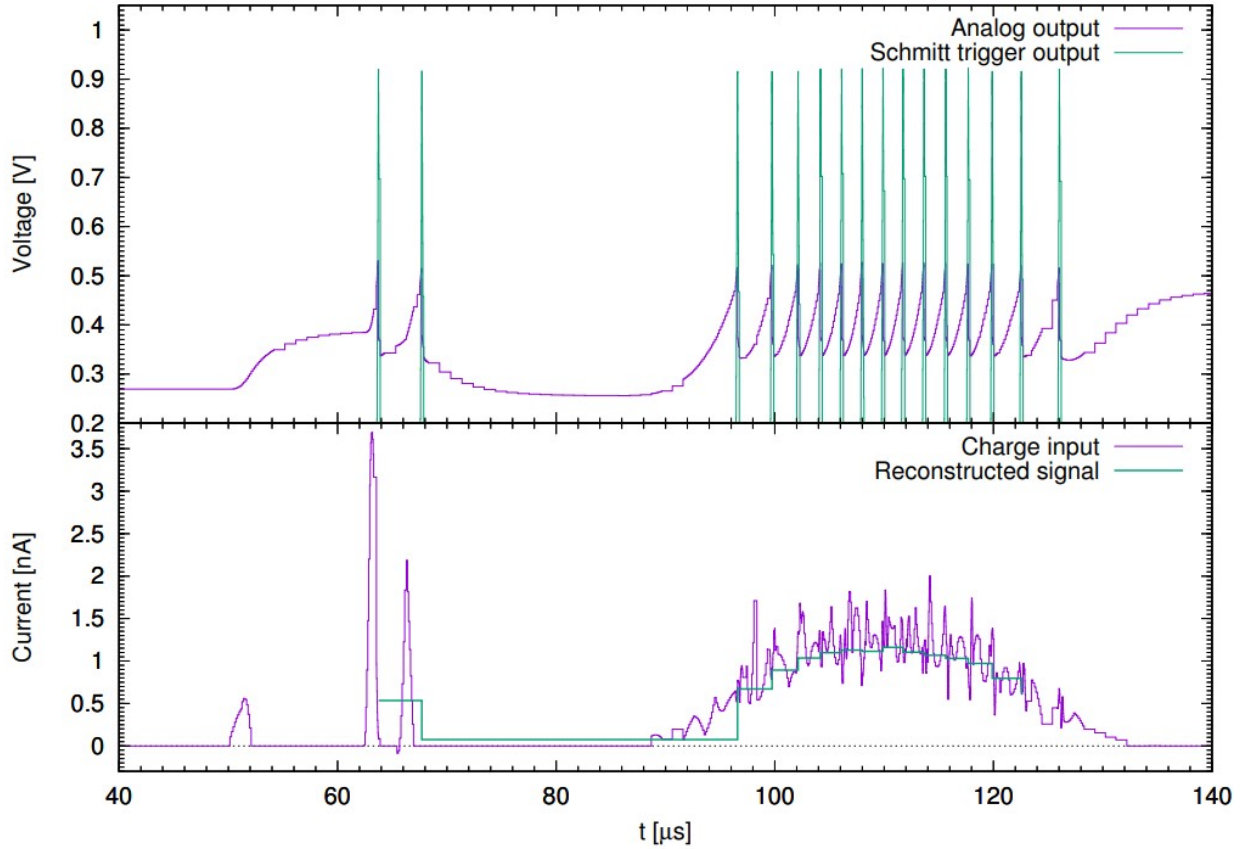


Figure 2.3: Example reconstruction of the reset time difference (RTD) based on the Q-Pix readout design. Shown is transistor-level charge integration simulation results for minimum ionizing tracks in LAr. The purple curve of the top pannel represents charge accumulating on the CSA, where the green curve is the reset output from the Schmitt trigger. The bottom pannel shows input charge (purple curve) overlayed on top of the reconstructed current signal. The  $Q_o$  value taken here is equal to 1 fC. Image is taken from [6].

Of these three parameters in Equation 2.1, two of them need to be calibrated. The validation of the charge calibration is beyond the scope of this work, but is briefly described in Chapter 5 Section 5.4. The local oscillator frequency is a digital ASIC level calibration and its results are a product of this thesis. Its procedure and first results are described in Chapter 4. The remaining reconstruction parameter is the timestamp, which is recorded by the digital back-end.

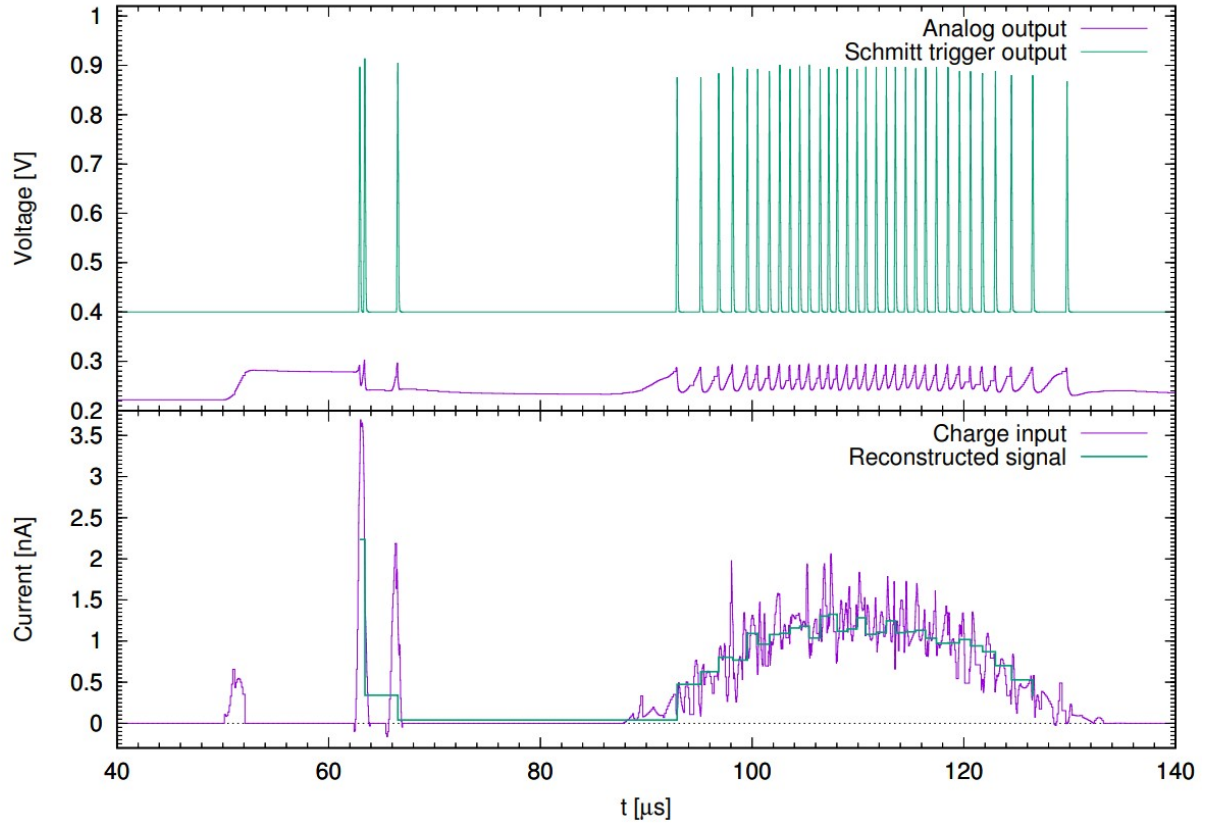


Figure 2.4: Example reconstruction of the reset time difference (RTD) based on the Q-Pix readout design. Shown is transistor-level charge integration simulation results for minimum ionizing tracks in LAr.  $Q_o$  was chosen to be  $0.3 \text{ fC}$ . The bottom panel in this image shows a better match of the reconstructed signal with a smaller  $Q_o$ . However, more ( $\approx 1.0 \text{ fC} / 0.3 \text{ fC}$ ) resets are produced as a result. Image is taken from [6].

### Event Reconstruction

One of the important features of a TPC is the ability to precisely reconstruct full tracks of ionizing particles. One intended benefit of a pixelated readout on any TPC is to show that there are improvements to reconstruction of these 3-D images.

Event reconstruction requires 3-spatial coordinates ( $x, y, z$ ) of a track's charge as well as time,  $t$ . The Q-Pix readout gives two ( $x, y$ ) coordinates for "free". Time is intrinsic to the Q-Pix datum, and may also be provided by an external photonics system (see Section 2.4). The final coordinate,  $z$ , is obtained with the LAr drift velocity (Table 1.3) and the drift time ( $T_{drift}$ ) by the equation:

$$z_{drift} = v_e * T_{drift} \quad (2.6)$$

measured current between each reset from Equation 2.1:

The reconstructed charge as a function of time is a piece-wise function of time based on the difference between successive  $N_{rtd}(i)$ :

$$Q_{i,drift}(t) = \frac{Q_o f_o}{N_{i,rtd}} t \quad (2.7)$$

### Comments on Uncertainties

The verification of the Q-Pix readout, in part, relies on tests to show that these timestamp data can be safely recorded and sent without loss to disc. Here we discuss potential uncertainties within the Q-Pix readout.

### Near Maximum Reset Rate

Equation 2.1 relates the maximum current ( $I_{max}$ ) in a Q-Pix readout at the limiting case of  $N_{rtd} = 1$ . For  $Q_o = 1$  fC and  $f_o = 30$  MHz,  $I_{max} = 30$  nA. However, since  $N_{rtd}$  is a difference between two 32-bit timestamps, it can only take positive integer values. This means that each current measurement can only take the form, for N integer:

$$I_{max} \sim \frac{30 \text{ nA}}{N}$$

Therefore, there can be large uncertainty in the measured currents for RTDs near the frequency of the oscillator. However, if there is sufficient total charge these discrete uncertainties can be accounted for after digital processing. An example of a periodic artificial input current of with  $I \approx I_{max}/10$  is shown below in Figure 2.1. The reconstructed charge over time is shown in Figure 2.6.

### Comments on Reconstruction Requirements

The uncertainty for the two transverse coordinates ( $\hat{x}$  and  $\hat{y}$ ) come from the pixel size. If we assume the electric field to be uniform, on average, across all  $O(10^7)$  pixels in an APA, then the charge drift will be uniformly distributed over the pixel size. Then, the pixel dimensions determine the resolution:  $\frac{3mm}{\sqrt{12}} \approx 0.87mm$ .

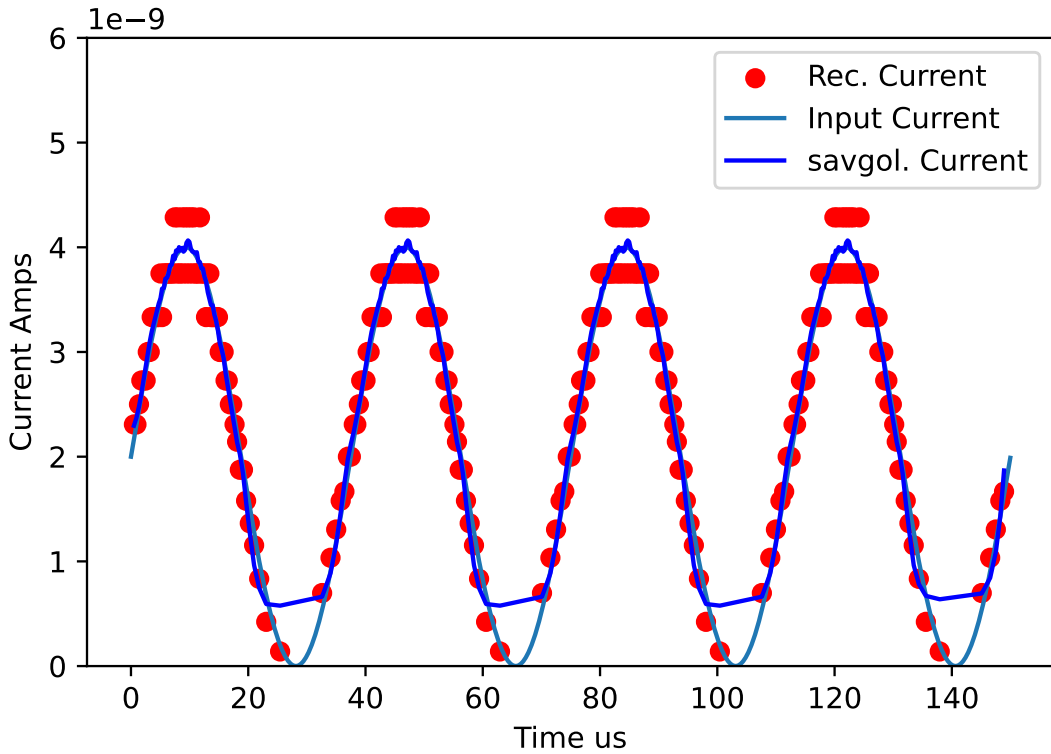


Figure 2.5: Arbitrary sine wave based current input. The maximum amplitude is chosen to be close to  $I_{max}$ . Reset Charge is chosen to be 1 fC and digital clock frequency of 30 MHz. The input current amplitude is close to the maximum, so that the reconstructed current can be far from the actual. This occurs since  $N_{rtd}$  can only take integer values, the reconstructed current can only take values of  $\frac{30}{N}$ . The red points indicate possible reconstructed current values, where the two highest points correspond to  $\frac{30}{7}$  and  $\frac{30}{8}$ , respectively. However, an example of a savgol filter (dark blue) is performed on the resets after the fact with near agreement of the large input. A use case of this kind of digital filtering would be applied to large current values only (peaks of the curves), and not for low current inputs where the pure timestamp difference provides better results.

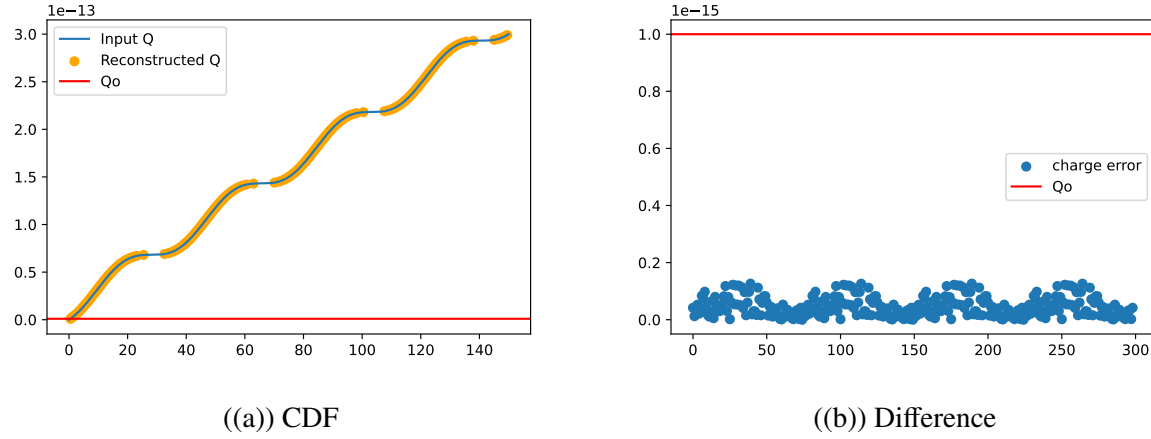


Figure 2.6: Reconstruction of Sub figures cumulative distribution function (CDF) of charge as a function of time (a) and the error (b). The input current for these data are shown in Figure 2.1. The pause in resets are when the error is small, since the current input is near zero. The red line indicates the minimum charge required for a single reset. The right plot indicates the difference between the true and reconstructed charge distributions compared to a single reset.

In order to reach the required uncertainty to measure the z-position ( $\sigma_z \simeq 1$  mm), the uncertainty from  $f_o$  must be small ( $\sim 1$  ppm). Other measurement uncertainties stem from Equation ???. The precision of the local oscillator frequency and the constant charge per reset determine the current reconstruction precision. Variable replenishment circuits can impact  $Q_o$ , which will also affect  $\sigma_z$ .

## 2.2 How Q-Pix fits into a 10 kt LArTPC

A future target detector for the Q-Pix readout is the DUNE-FD 10 kt module. To explore how Q-Pix could be used in this detector we provide a brief over-view of the DUNE-FD electronics and compare with those requirements for Q-Pix based readout. The simulation results presented in Chapter 5 are based on the detector volume of a single APA within a DUNE-FD module.

### The DUNE Far Detector Electronics

The DUNE-FD is a modular assembly of Anode Plane Assemblies (APA) as shown in Figure 2.2. Each Single-Phase (SP) 10 kt module consists of 150 APAs. The APA's full description can be found at [7]. Each APA stores its own front-end electronics which are in the LAr and are shown in Figure 2.2.

Figure 2.2 shows that each APA uses 20 FEMBs to digitize 128 of the 2560 channels. Of the 128

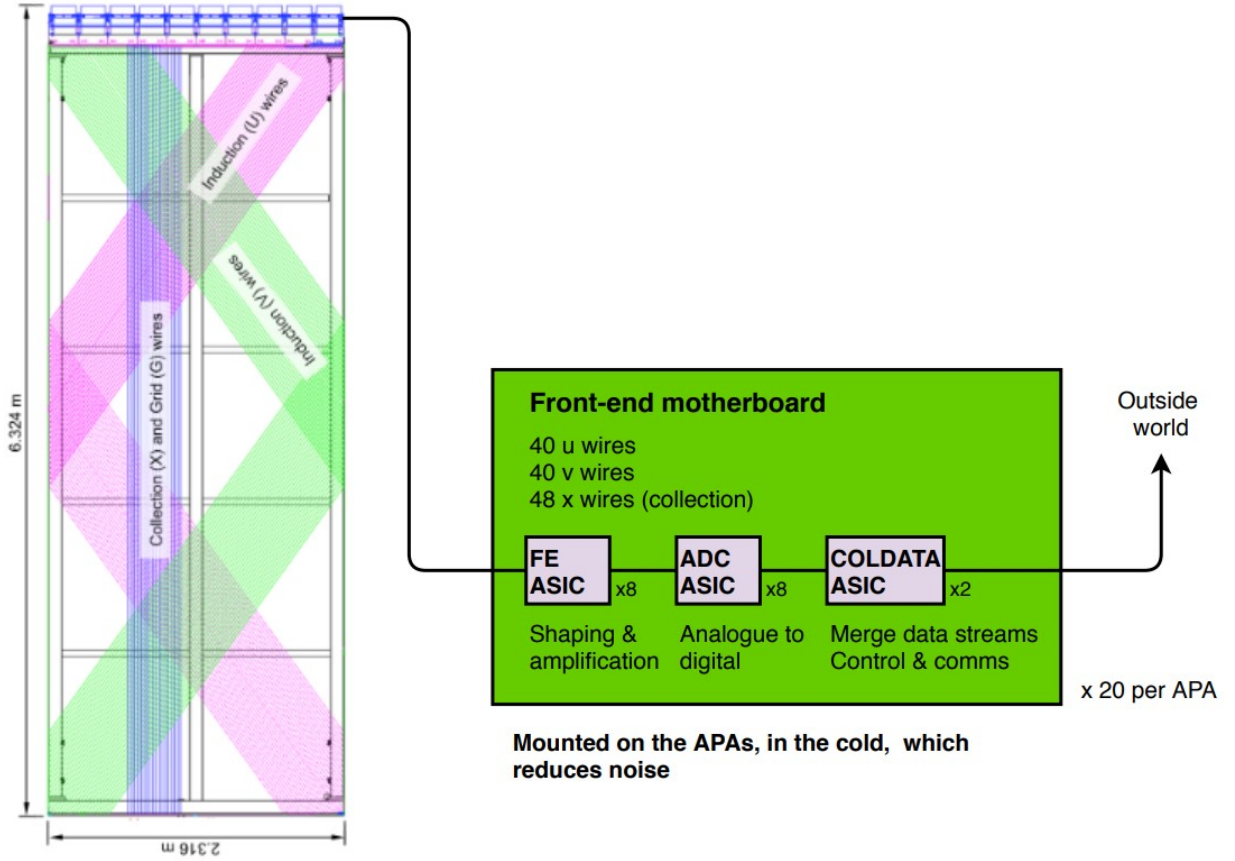


Figure 2.7: Image taken from [7], Fig 1.12 of section 1.8. Image shows an overlay the the relevant charge collection wires within a DUNE-FD SP LArTPC.

channels 40 are each taken from the U and V (induction) layers, and 48 wires are taken from the X (conduction) layer. Each FEMB also houses a total of 18 ASICs which smooth, digitize, and aggregate data before being sent to the Warm Interface CRATE (WIC). The total number of ASICs per APA is  $18 \times 20 = 360$ . Since each 10 kt module uses 150 APAs the total number of ASICs would be multiplied by 150.

On each FEMB are three ASICs responsible for collecting the charge as it passes between the wires and sending it out of the cryostat. The first ASIC is a waveform-shaping and amplification ASIC. The second ASIC is the ADC ASIC and is responsible for the converting the analog signal to digital. The final ASIC, called the COLDATA ASIC, merges the data streams from the previous

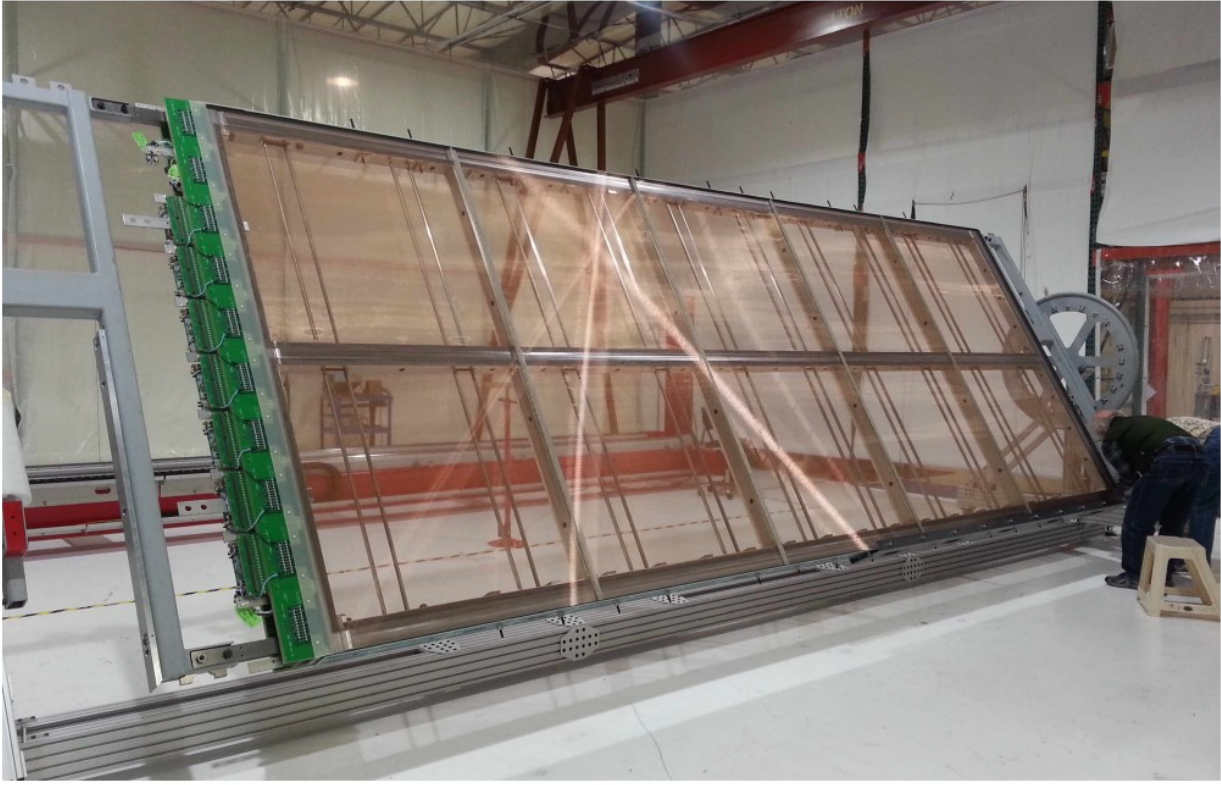


Figure 2.8: A simple caption [7]

ASICs and is responsible for communication between the motherboard and the outside world.

Table 2.2 summarizes the electronic requirements expected for the DUNE-FD SP module. The maximum expected data collection is expected to not exceed more than 30 PB/year, which corresponds roughly to  $\approx 1Gb/s$  of continuous collection. The expected wire electron noise level is design to be  $\approx 1000 e^-$ . Sampling frequency of 12 bit ADCs is 12 MHz. Large signals require a linear reponse of  $500 ke^-$ , and ensures that fewer than 10% of beam events experience saturation. Dune expects to draw less than 50 mW per channel, and incur less than 1% dead channels.

### **Q-Pix Comparison to DUNE-FD Electronics**

Each APA is  $6.324 \text{ m} \times 2.316 \text{ m}$ , for a total area of  $14.646 \text{ m}^2$ . From these dimensions the expected channel count of the QPix readout on the DUNE-FD APA is

$$N_{pix} = 14.646 \text{ m}^2 * \frac{1 pixel}{4 \text{ mm}^2} * \frac{1000^2 \text{ mm}^2}{\text{m}^2} = 915399 \quad (2.8)$$

Description	Specification	Rationale
System Noise	$< 1000 e^-$	Provides $>5:1$ S/N on induction planes for pattern recognition and two-track separation.
Signal Saturation	$500,000 e^-$	Maintain calorimetric performance for multi-proton final state.
Cold Electronics Power Consumption	$< 50 \text{ mW per channel}$	No bubbles in LAr to reduce HV discharge risk
Number of Channels per front-end motherboard	128	The total number of wires on one side of an APA, 1,280, must be an integer multiple of the number of channels on the FEMBs.
Dead Channels	$< 1\%$	Minimize the degradation in physics performance over the $> 20$ -year detector operation.
Maximum diameter of conduit enclosing the cold cables while they are routed through the APA frame.	6.35 cm (2.5")	Avoid the need for further changes to the APA frame and for routing the cables along the cryostat walls

Table 2.1: Selected Requirements of DUNE-FD TPC electronics and Expected QPix Design goals of first generation ASIC development for comparison. The table information is taken from the inner three columns of Table 4.1 in [7]. Due to the different charge sensitive geometries between a wire and pixel-based readout, the required noise and number of channels are not easily comparable.

The total number of free running oscillators ( $N_{osc}$ ) per DUNE-APA for a given pixel of  $4 \text{ mm}^2$  is:

$$N_{osc} = \frac{915399}{16} \approx 57213 \quad (2.9)$$

$N_{osc}$  represents the total number of front-end ASICs whose data must be aggregated and sent outside of the cold electronics to a warm interface. Therefore we expect the order of the number of free running oscillators per DUNE-APA  $O(10^5)$ . This also gives an order of magnitude estimate of the increase of number of ASICs compared to the MWPC readout of Single-Phase (SP) DUNE-FD.

To have a comparable power draw compared to DUNE-FD, which has 2560 channels, then QPix would need less than  $\approx 140 \mu\text{W}$  of power draw per channel. Too much energy dissipated in the LAr creates bubbles which is a high voltage (HV) discharge risk. The total channel count for a 10 kT module is based on 150 DUNE-APAs or  $2560 \times 150 = 384000$ . Thus, the number of extra

Description	Specification	Rationale
System Noise	$\approx 300e^-$	Provides $\approx 17:1$ S/N ratio, a component of front-end integrator.
Signal Saturation	30 nA per pixel	Upper limit from local oscillator frequency and integrator reset.
Cold Electronics Power Consumption	$< 100\mu\text{W}$ per channel	Equivalent power consumption for heating found in DUNE-FD.
Number of Channels per Tile	4096	Design parameter to be calculated.

Table 2.2: Q-Pix based Requirements which are compared to the equivalent DUNE-FD SP module found in table 2.2. Results here are necessarily speculative, but provide an insight to the design goal. The system noise is a contribution of leakage current per reset, uneven electric fields in the TPC, or uncertainties in the replenishment circuit per reset. Signal saturation is defined as the maximum measureable current based  $Q_o = 1 \text{ fC}$  and  $f_o = 30 \text{ MHz}$ . The Q-Pix readout can also be saturated by too many resets if the FIFO buffers overflow (see Chapter 5 for further discussion). The power consumption per channel is a direct division compared to Table 2.2. The number of channels per tile depends on the tile size as well as the number of pixels per ASIC (see Chapter 4 for further discussion).

analog channels that QPix is required to measure, compared to the typical wire readout, increases by a factor of  $915399/2560 \approx 357$ .

Q-Pix will instead offer conversion from analog (charge) to digital (32 bit time) signals on a single ASIC. These front-end ASICs would be arrayed in modular tiles within a single APA. Where the tiles themselves would be connected and spread out to cover the entire area of an APA. A further discussion of the Q-Pix tiles can be found in Section ??.

To connect the entire APA the Q-Pix readout will design modular tiles which will hold a subset of nodes ( $\sim 16 \times 16$  ASICs). Each tile will interface with a single FPGA (or other ASIC) chip which would concentrate the digital data for each tile; we refer to this FPGA as the DAQ-Node (DN). Then, each DN can interface could optionally connect a single concentrator FPGA for the entire APA. This final concentrator would send the data to the Warm-Interface-Cards (WIC) out of the cold electronics (CE). The final concentrator FPGA we refer to as the Super-DAQ-node (SDN).

The exact description and characteriziation of the WIC for a Q-Pix depends on the final implementation of the SDN.

## 2.3 The Digital Back-end

We define the digital back-end as the part of the larger Q-Pix readout system that is responsible for handling the timestamp data once it is recorded. This sub-system must be able to record and store data, be robust against SPF, define error states, and more.

In this section we introduce considerations which guided the design of the first two Q-Pix ASIC prototypes. These design choices for the digital prototype are enumerated in table 2.3.

### Digital ASIC Prototype Design Choices

The table 2.3 highlights some design choices of the first digital Q-Pix ASIC prototype. Four neighbor connections were chosen as the design choice two allow for communication in either direction along the x and y axes. The local and remote FIFO depths determine how many resets and communication packets the ASIC may store at any one time.

### Single Point Failures

Q-Pix digital design should provide “robust resilience” against single point failure (SPF). The readout technology presented here relies on huge numbers of readout channels ( $10^8$ ) compared to current MWPC designs ( $10^5$ ). As such, extra care must be made in designing new technology to improve over established, seemingly simpler means.

This principle guides design choices such as the use of independent local oscillators at the pixel-level instead of a provided distributed clock. This design choice, in particular, is discussed at length in chapter 4, and the findings presented there are one of the major contributions presented in this thesis.

The design which avoids SPF and handles the digital requirements presented here, namely: the continual time calibration of each local oscillator ( $N_{osc} \approx 10^5$ ) is a product of this thesis.

However, as discussed in a later section (Sect. ??) since the amount of data produced depends on the charge acquired in event, the amount of data collected can not be known before recording.

## 2.4 Q-Pix and Light Detection

Parameter Name	Value	Description
Local Oscillator Frequency	30 MHz	Determines maximum current reconstruction (equation 2.1). Stability of local oscillator also determines z-position reconstruction uncertainty (Sect. 2.1).
Connections	4×2 (Tx and Rx)	Eight differential pair connections are made to support four transmitter (Tx) and receiver (Rx) lines.
Communication Protocol	Endeavor	Protocol determines packet stability based on oscillator frequency as well as packet transaction time. Results of these tests are done in Chapter 4.
Timestamp Bits	32	Determines the total number of unique counts each timestamp value can take. Also determines the "warp-around" time based on the local oscillator (see Equation ??).
Local FIFO Depth	64	Total number of timestamps the ASIC can store before running out of memory. ASIC will not record additional resets until emptied.
Remote FIFO Depth	128	Total number of remote packets ASIC can store before running out of memory. ASIC will not write additional packets from neighbors.

Table 2.3: Summary of design parameters for the first Q-Pix digital ASIC. The local oscillator is a ring oscillator with a targeted mean of 30 MHz. Each ASIC will be able to communicate with up to four neighbor nodes via a custom "Endeavor" protocol. The testing and verification of the endeavor protocol is found in Chapter 4. The values of the local and remote FIFO depth were selected due to fabrication requirements, whose future values are discussion of Chapter 5.

The results of this thesis analyze the response of the Q-Pix digital readout without any analysis paid towards photon collection. However, recent progress regarding amorphous selenium (aSe) [8] has been made towards inclusion of an optical system.

The current pixel dimensions of Q-Pix are 4 mm × 4 mm which have a total active area of 16mm<sup>2</sup>. Most of this active area is unused for the charge collection pad, which could be as small as drill-hole via (6 mil << 16mm<sup>2</sup>). Most of the remaining area, then, could be plated with a photo-sensitive material (such as aSe).

aSe could capture incoming scintillation photons and provide an additional voltage measurement at each pixel. Depending on the sensitivity, such a measurement could be used to reconstruct tracks by providing a  $\frac{dE}{dX}$  measurement, or even be used as a time-tag or a trigger.

The use of a reference trigger could be useful to establish event-time within the same system,

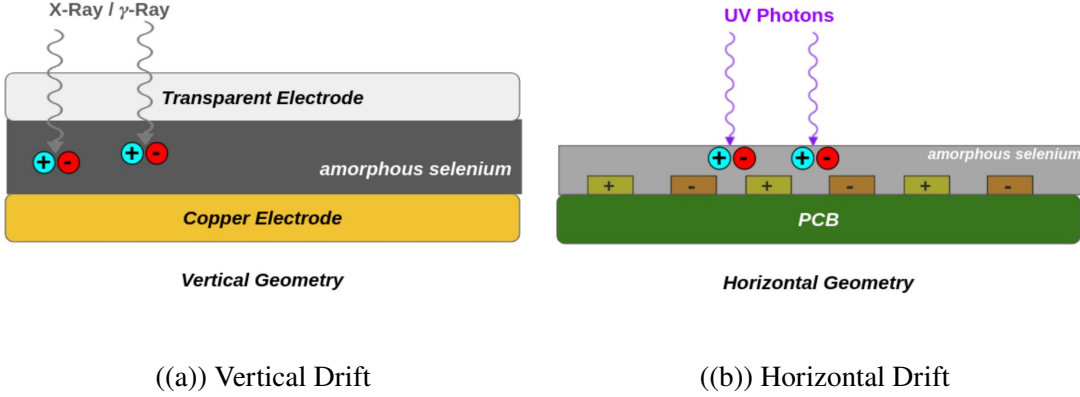


Figure 2.9: Images taken from [<https://doi.org/10.48550/arxiv.2207.11127>.] The vertical drift geometry (left) shows an electrode on the top layer, whereas the horizontal (right) geometry integrates the electrodes within the aSe. The vertical geometry is an easier design, but most electrodes are not transparent to VUV scintillation light. The horizontal geometry solves this problem, at the cost of a more complicated design.

and allow adjacent pixels which would receive photons, but not charge, to contribute to time reconstruction. Any reconstructed event requires some  $T_o$  time to indicate the start of the event. Typically this is done via scintillation photons from a secondary system, where the photons arrive nearly instantly at the collection planes compared to the slow drift speed of the electrons.

The natural pixelization of Q-Pix required the charge collection can also be used to be sensitive to scintillation photons. These photons could not only provide the required event timing but also provide an additional means of calorimetry and track reconstruction. Additional work is currently underway to demonstrate the viability.

Currently there are two competing geometries to incorporate light collection within Q-Pix. Figure 2.9 shows the vertical and horizontal drift geometries. The vertical drift geometry is an easier design geometry, however the top electrode must not only be able to collect charge it must also be transparent. On the other hand, the horizontal drift geometry solves the transparency problem but involves a more complicated hardware design.

## 2.5 Q-Pix at Low Energy: Supernova Studies

Work has been done to characterize a Q-Pix readout ability measure core collapse supernovae [9] events within a DUNE-FD module. These studies involved particle Geant4-based( [80]) simulations

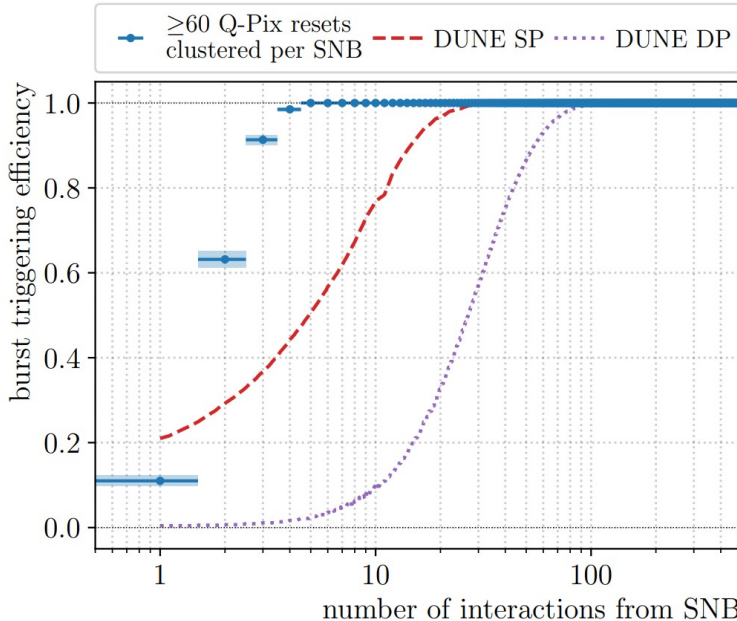


Figure 2.10: Image is taken directly from [9]. Plotted is the supernova burst triggering efficiency as a function of  $\nu_e$  interactions in a 10 kT DUNE-FD module. The points in blue indicate that a series of 60 resets are "clustered" to use as an identification of a supernova event. The other curves are taken from Ref. [supernova\_Abi\_2021].

for low energy ( $\approx 10$  MeV) neutrino events. The results indicate several advantages Q-Pix readout will have over a traditional wire-based readout.

One advantage is the lower overall data rates ( $1.03 \times 10^{-6} < 2$  pB per year) compared to the traditional single-phase readout. This reduction in data rates could allow for a 10 kT Q-Pix module to collect timestamp data continually. Such a continuous readout, with no trigger, could be particularly useful in collecting supernova burst events. Figure 2.5 compares the trigger sensitivity supernova trigger burst efficiencies between the Q-Pix readout against traditional wire-readout.

## *Chapter 3*

# THE FIRST PROTOTYPE: FIRST RESETS AND LEAKAGE MEASUREMENTS

In this chapter we present the first implementation of the Q-Pix-based design using off-the-shelf electronics.

This section describes the first prototype based on the Q-Pix readout: The Simplified Analog Q-Pix (SAQ). First we discuss the design goals of the prototype and highlight the basic building blocks of any Q-Pix based prototype. Next, We describe the prototype status as well as lessons learned in characterizing noise and performing calibrations.

In the final part of this section we describe the future goals of this prototype, including the calibration of GEMs and promising future analysis. The final results of SAQ are just beyond the scope of this work, but I provide SAQ's details here as a means of introducing the front-end of Q-Pix as well as highlighting my personal contributions to Q-Pix's overall development.

The entire data acquisition (DAQ) chain used for both SAQ experimental setups are my sole independent work. My contributions include the the development and deployment firmware on the Zybo-Z7 FPGA, as well as the embedded software code on the integrated SoC processing system. I developed the the Python3 software which handles packet communication as well as the GUI for data collection. I also developed the data storage trees, which are the original containers for all data used in the analysis. Additionally, I wrote analysis scripts used for the work done at the SAQ site at the University of Texas at Arlington.

### **3.1 Simplified Analog Q-Pix: System Design**

The SAQ prototype is designed as a first physical proof-of-concept for a Q-Pix readout.

### **3.2 The SAQ Prototype Design**

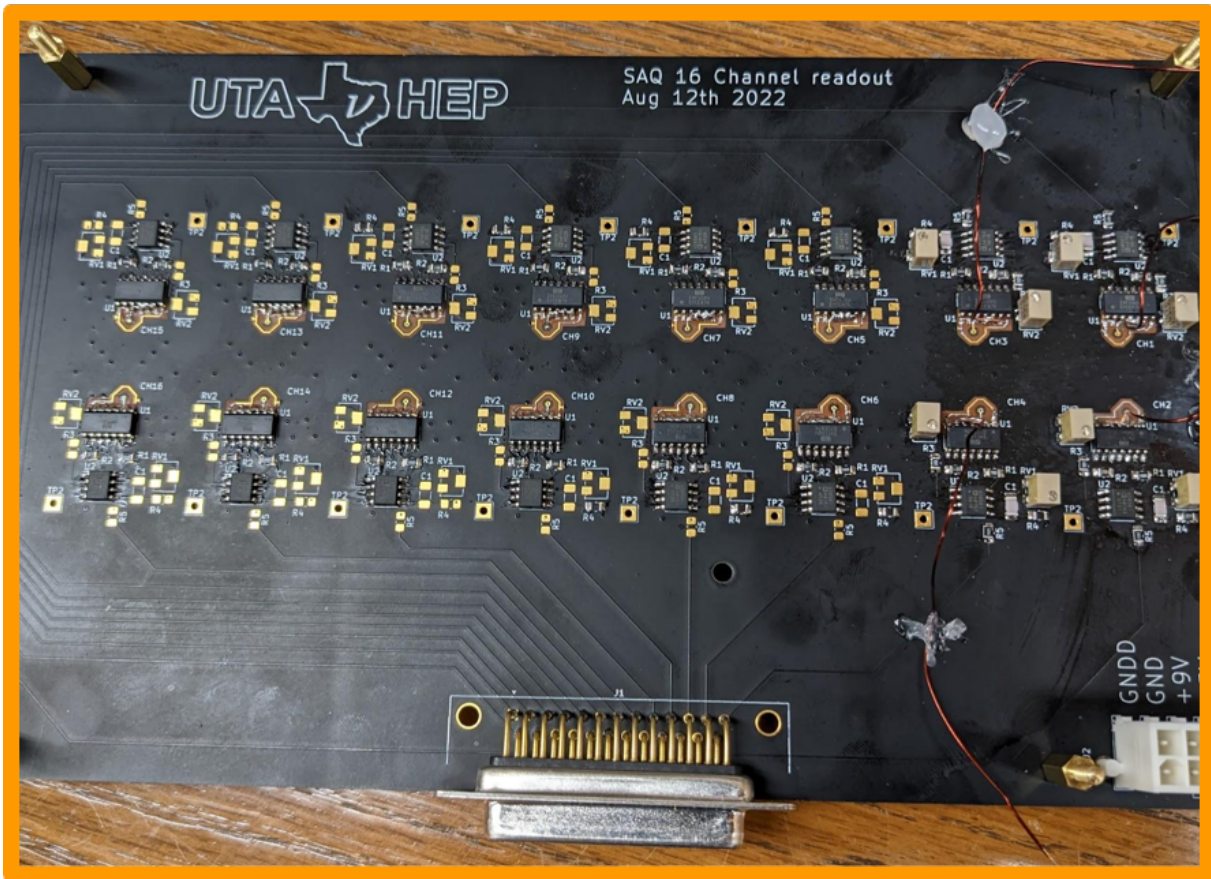


Figure 3.1: The SAQ Setup model based on ??.

## The TPC Design

### The Integrator Circuit

## The SAQ Data Acquisition

All resets are recorded via a Zybo-Z7-20 Digilent FPGA prototype board, which uses an Artix Zynq based architecture. The reference manual for the Zybo Z7 board used in SAQ can be found at [81].

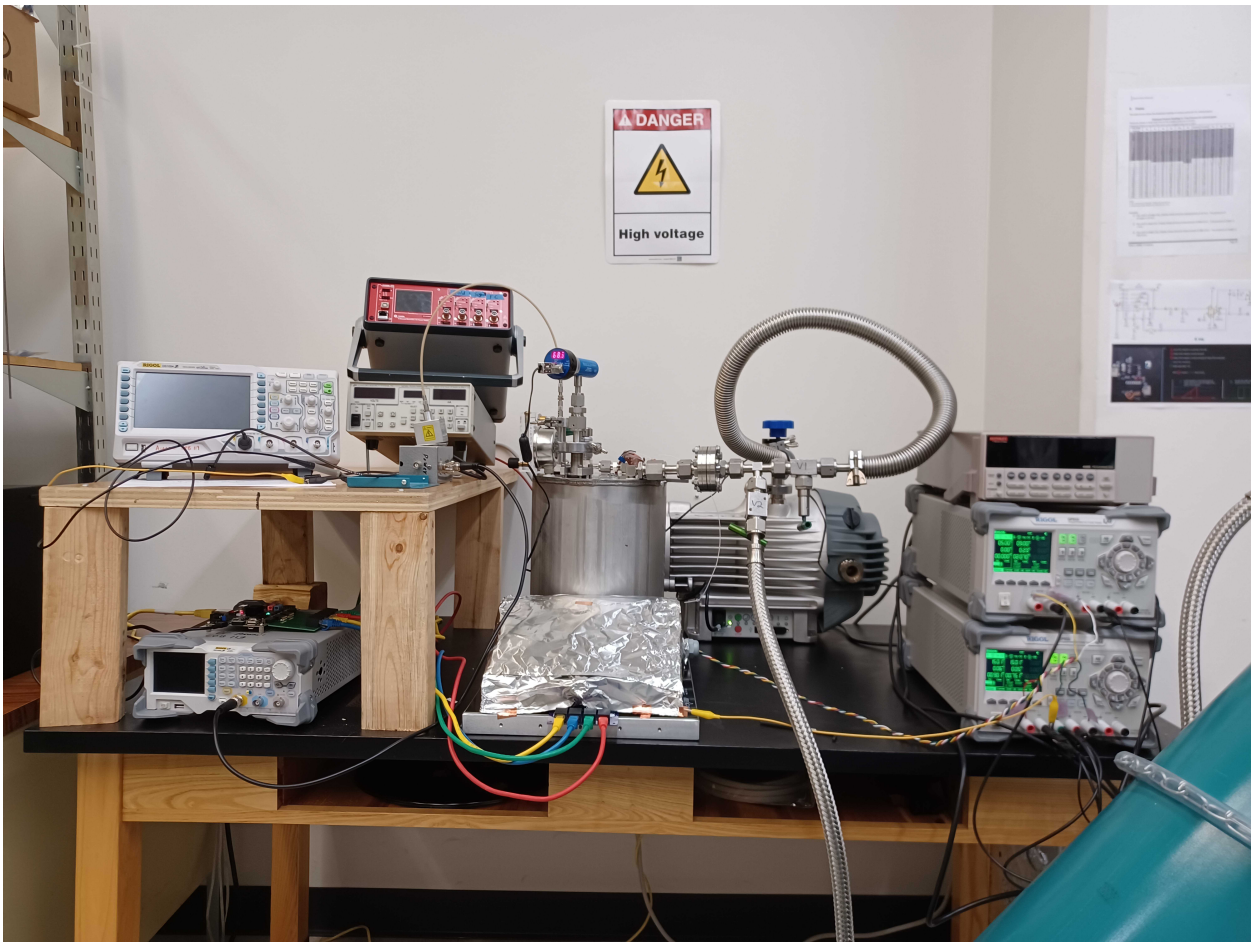


Figure 3.2: The SAQ Setup model based on [3.2](#).

### 3.3 Noise Measurements

The Q-Pix readout is dependent on the integrator, which provides the basic datum of the reset time. Therefore, a dominant source of noise are electrons which accumulate on the integrator which are not signal electrons. There are two possible sources for these noise electrons: excess electrons produced from the target volume or leakage current due to transistor effects from the integrator circuit. In this section we focus on the noise electrons due to the leakage current.

#### Integrating towards background Current

Leakage current arises due to non-ideal behavior of the integrator operational amplifier, where the voltage across the two input terminals is nonzero. Measurements of this leakage current then are performed by measuring voltage difference across the terminals as well as directly using a pico-ammeter.

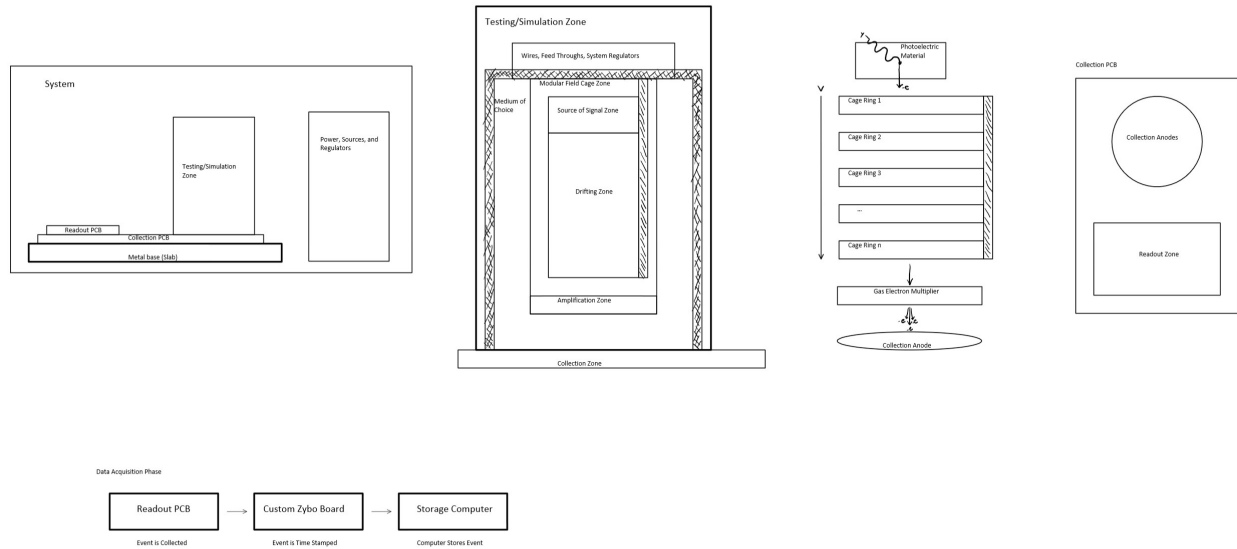


Figure 3.3: The SAQ Setup model based on ??.

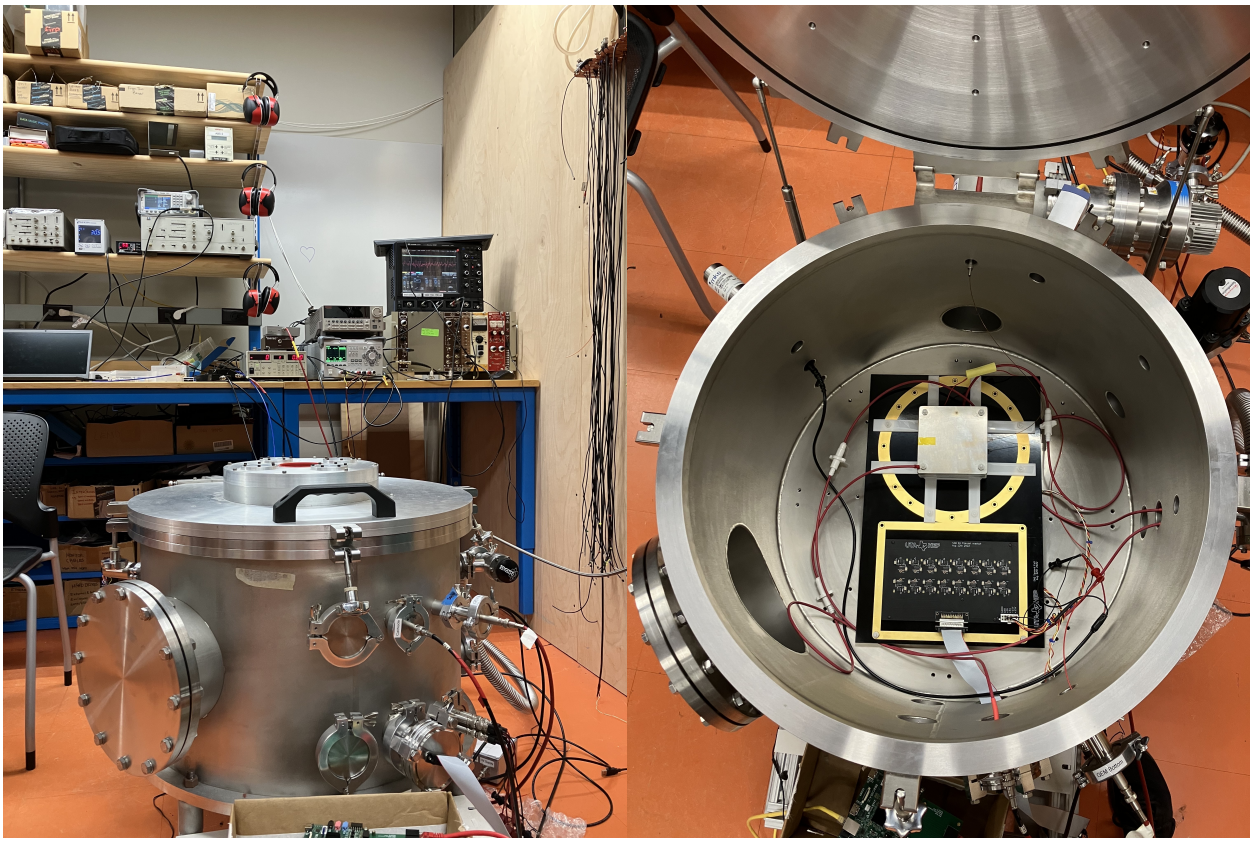
## Background Current in the GAr

The second source of noise electrons are produced from the target volume. The target volume is an ultra pure Argon Gas at TODO militorr. In this case the excess electrons come from the nominal decay of Ar-39, which provide excess electrons from the natural  $\beta$  decay, at a rate of  $\approx 1 \text{ BqKg}^{-1}$

## Digital Noise Sources and Clock Stability

### 3.4 Xenon Gas Lamp Measurements

### 3.5 Results and Discussion



((a))

((b))

Figure 3.4: Picture of the TPC and DAQ setups at Wellesley University.

### Current Status and Planned Measurements

Measurements of Transverse and Longitudinal diffusion of electrons within electric fields of strength 500 V/cm have been performed before [82].

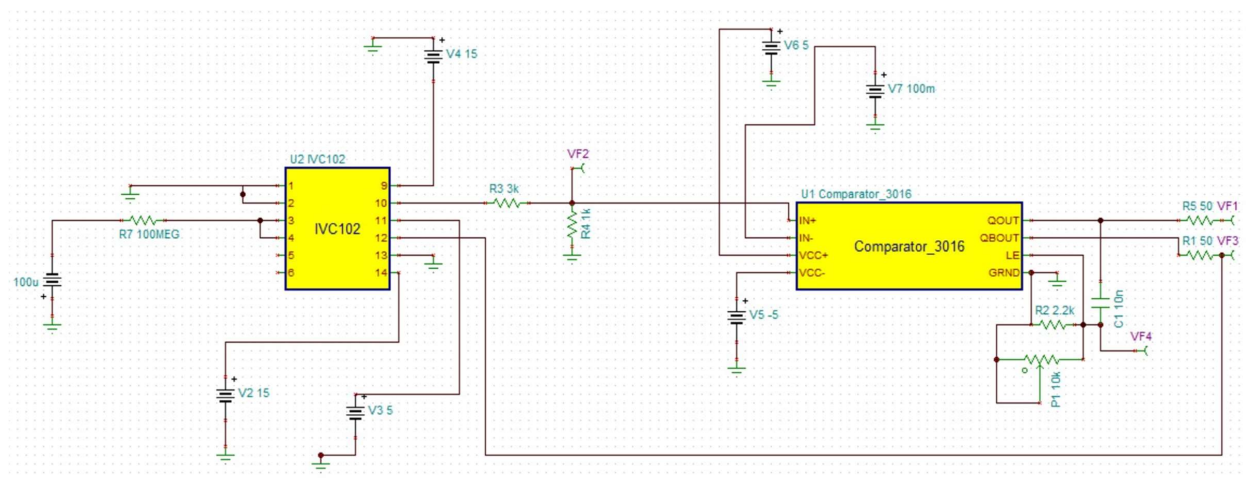


Figure 3.5: The SAQ circuit in a Spice Simulation. The IVC [10] chip chosen as the off-the-shelf integrator for this experiment. The main selection choice for this part is due to its low input bias current  $\ll 750 \text{ fA}$ .

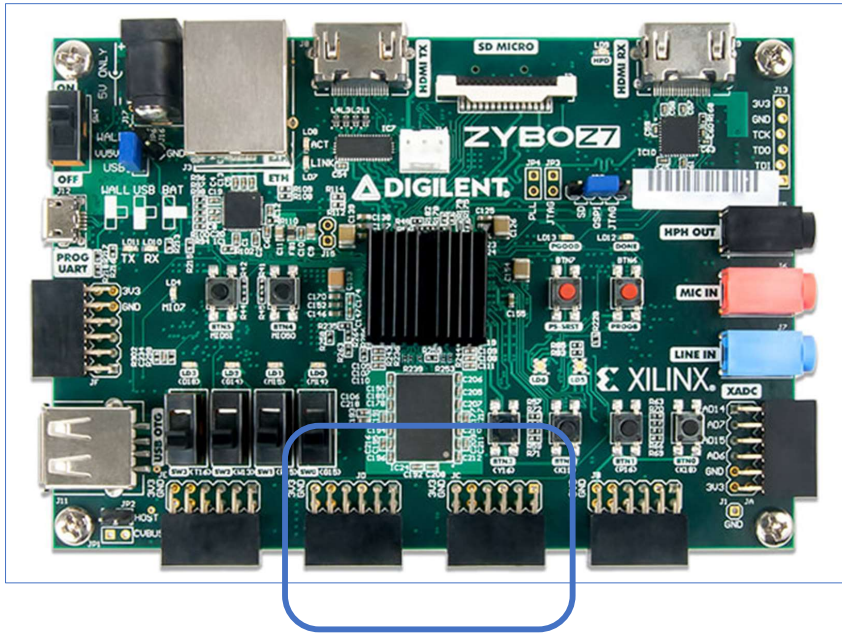


Figure 3.6: An image of the data acquisition board from Digilent, Zybo Z7-20. This board was chosen for its multiple configurable input channels, as well as the Zynq-based architecture of the onboard FPGA. Additionally, the use of the ethernet provides 1 GB transfer speeds, which is more than sufficient for the application. Packet data transfer rates have been verified with this readout at stable rates of 10 kHz.

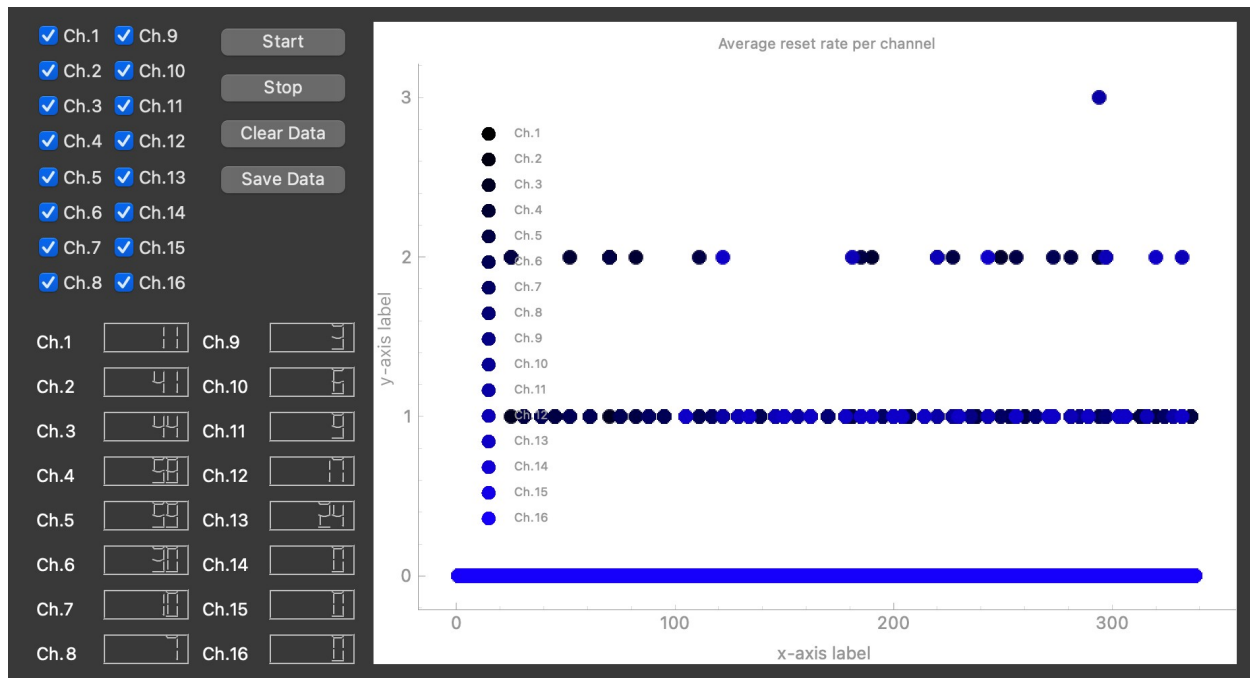


Figure 3.7: The SAQ GUI with real time plotting of incoming resets to the Zybo board.

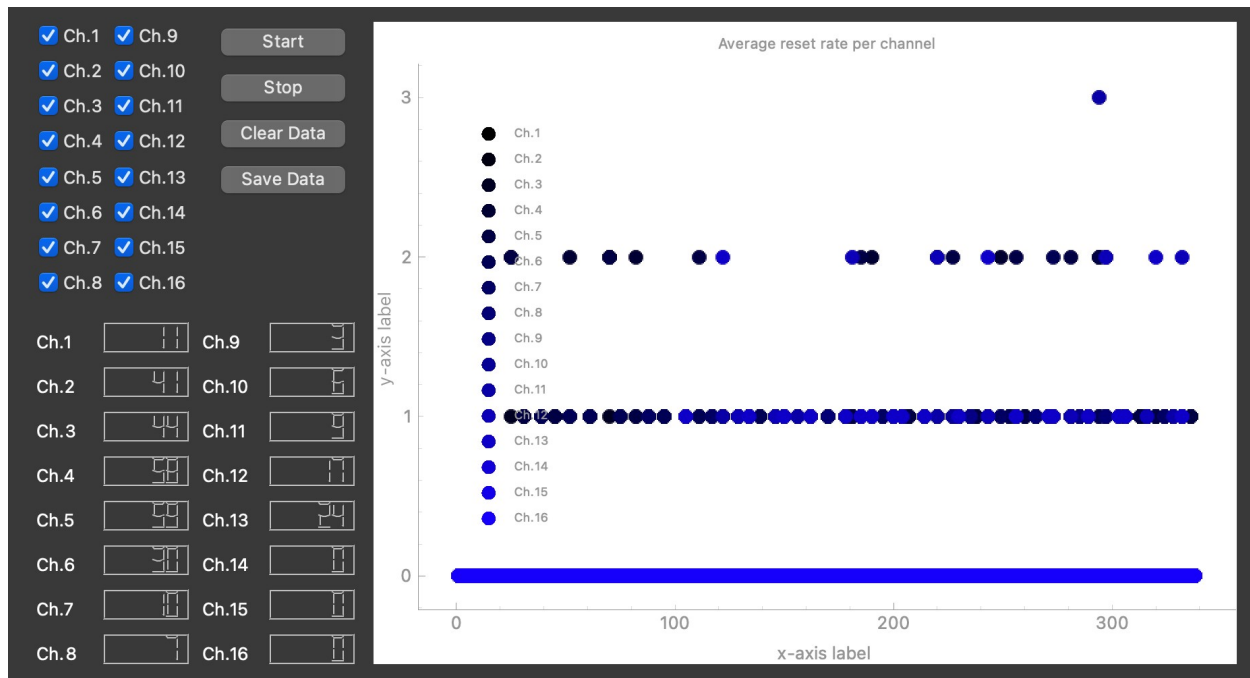


Figure 3.8: Drift Current Measurements to go here.

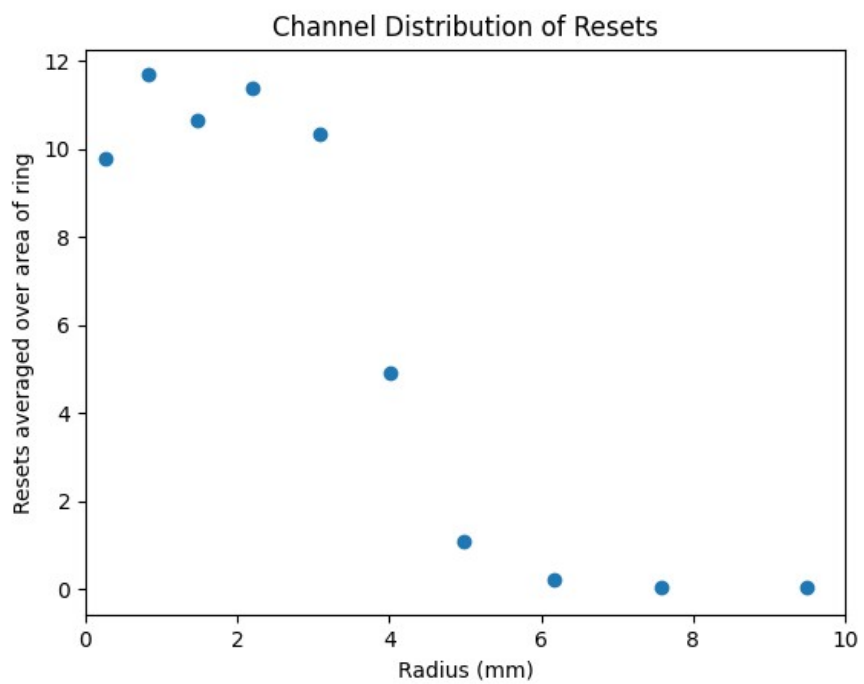


Figure 3.9: First diffusion measurement in P-10 gas performed at Wellesy University.

## *Chapter 4*

# DIGITAL BACK-END VIABILITY STUDIES

In this chapter we describe the overall structure of the digital back-end of the Q-Pix design as well as results from prototype board tests. As described in previous chapters, the digital back-end of the Q-Pix readout is composed of an array of ASICs (FPGAs, here), which we refer to here to as digital nodes. Each digital node in the prototype array is implemented as a lattice ice40UP5k FPGA.

This chapter is divided into two parts. The first part we give a detailed description of the requirements of a successful deployment digital system in a Q-Pix based detector at DUNE APA scales. The motivation is to describe how the digital back-end of Q-Pix based readout would eventually scale into a DUNE-FD LArTPC 10 kT module.

The second part of this chapter is dedicated to the first evaluation boards developed and tested which implement the digital nodes in Lattice iCE40UP FGPAs [83]. The second part also outlines the design of the PCB on which these FPGAs are implemented, as well as results, which are motivated from the first part of this chapter.

The Lattice Semiconductor FPGAs [83] were selected because of the small form factor, pin out, availability, as well as low power consumption. There are planned tests for future, but not presented here, to indicate its viability of over-the-counter FGPAs in LArTPc. If such cheap and available FPGAs were shown to be reliable use in a LArTPC environment, that could influence future detector development and the selection of the digital chip for the Q-Pix readout.

All results presented in this chapter are my own individual work.

### **4.1 Digital Design Overview**

The digital system of the Q-Pix readout begins when the first digital data are recorded. This occurs during the collection of a recorded timestamp in response to the logic reset pulse sent from the integrating analog front-end. This record happens in response to output reset-pulse sent from any one, or more, of the pixels. Then, the timestamp record is the value of a local 32-bit counter at the time the node receives the reset pulse. When a reset occurs the data recorded are the reset values of each pixel, and the only data required for a full analysis of all reconstruction with a LArTPC are:

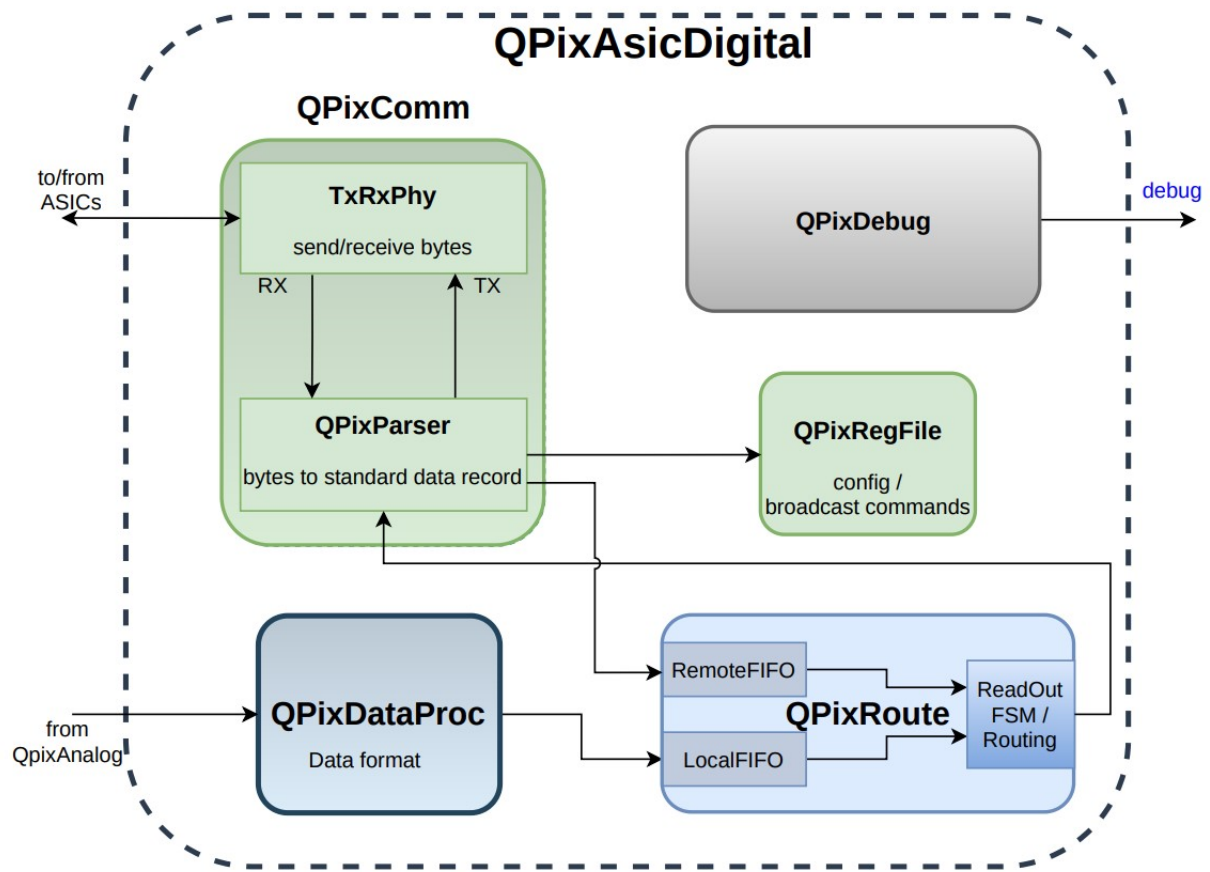


Figure 4.1: Diagram of the Digital node. The controlling sections of the logic for the digital node are QpixComm, QpixDataProc, QpixRoute, and QpixRegFile. The Comm layer is responsible for routing packets between the physical layer and handles the parsing of incoming data packets. The DataProc layer is responsible for recording timestamp data during a reset from the analog front-end. The RegFile contains configuration information, such as routing. QpixRoute determines the controlling state machine that, based on register configurations, determines what packets are sent to which neighboring nodes.

Each of these remote ASICs are running on free-running independent clocks, designed with a frequency of 30 MHz.

## Communications

The QpixComm module controls incoming and outgoing packet logic.

The logic responsible for identifying how an incoming packet is handled is defined in QPixParser. When a valid 64 bit packet has been received, a valid signal is thrown high. The packet is handled based on the bits within the header of this packet. How the packet is handled is determined by the packet header [4.1](#).

Packets are only comprehensible for types if the same region of the 64 bits are ubiquitous. For this purpose all packets use or reserve the same 20 bits, with four bits reserved for the packet type:

- Unused, 60–63
- Header, 56–59
- X Location, 36–39
- Y Location, 32–35

If the packet originated from the aggregator node then this packet is treated as a broadcast. Broadcast commands record unique numbers associated with this request and are also sent to all connected neighborhoods except from the direction that the broadcast is received. A unique broadcast number is used to avoid registering the same request.

If the packet was not from an aggregator node, then this packet is treated as remote data from a neighbor node. All data transfers of any kind are treated so that all communication happens between individual nodes and an aggregator node. Therefore, any packet that originates on a node that isn't the aggregator node will be sent to the aggregator node. The direction of that this packet is sent is determined by a configuration register.

## The Structure of a Data Word

Each digital node responds to a successful transmission of a 64-bit packet. We choose that each packet, regardless of type, be 64-bits to reduce the overall packet checking complexity on each node. The type of the packet then is selected by the word type, which is reserved for a static 4 bits within each 64-bit word. This allows for a total amount of 16 unique packets each of which may be handled differently.

A successful transmission of a data word is indicated by the protocol when the correct number of bits have been read (see Section 4.1). When a correct packet is filled a single flag is raised to indicate that the word is valid, and then the appropriate logic parses the header bits of the packet and determines how the packet should be handled.

There are two main types of packets that a digital node would receive, a register request or a data word from another node. In the first case, the register request indicates that this packet originated from the aggregator node and may either go to a specific node or a broadcast to the entire array. Whether or not the register request is a broadcast is checked against another bit, and the packet is handled accordingly. If the packet is a broadcast, the receiving node records an identification number associated with the broadcast, which it uses to ignore additional packets it may receive that correspond to the same broadcast.

The second kind of packet the digital node may receive is a data type word. In the case of data words, there are also two main types: a word which contains the 32 bit timestamp or an event end word. The 32 bit timestamp data word are the words which must eventually make it to disk for analysis. The data words must also encode the row and column position of the original nodes.

## Configuration

The configuration of the digital node is handled through local registers. These registers are described within QpixRegFile module, shown in Figure. 4.1. These registers include the ability to control routing of data packets, reset, enable, and channel masking. The Table ?? describes the implemented register addresses and their functions:

The composition of any register word is shown in Table 4.1.

## Local Data Collection

The digital node is responsible for collecting and storing local timestamps in response to pixel resets as well as being able to communicate these data with neighbor nodes. The node must be able

Address	Name	Function
0x01	Command	Used to broadcast type or trigger
0x03	Routing	Allows selection between manual or dynamic routing.
0x04	Channel Mask	Selection of mask prevents triggers from masked channels.
0x05	Position	Allows configuration of X and Y coordinates of node.
0x06	Disable	Selection of which neighbor node inputs are ignored.
0x08	Local Disable	Selection of which input and out neighbor nodes can be ignored.

Table 4.1: The address values are not sequential because some registers have become deprecated through development.

Bit Location	Name	Function
0–15	Data	Excess bits
16–31	Address	Excess bits
40–43	Y Position Transfers	Next Y position in tile.
44–47	X Position Transfers	Next X position in tile.
48	Source Flag	Single Bit flag to indicate whether or not packet originated from aggregator.
49–52	Request ID	Identifier bits to specify broadcast.
53	Destination Flag	Identifier bit to specify if broadcast is meant for a specific node.
54	Read Flag	Identifier flag to specify if register request is a read.
55	Write Flag	Identifier flag to specify if register request is a write.

Table 4.2: Description of the bit values within the register request word.

to buffer data so as to prevent packet loss during transactions. The separation of the remote and local packets are contained within two different FIFOs, as shown in Figure 4.1.

There are two conditions which must be met in order for a timestamp to be recorded. First, an incoming reset pulse must be supplied from one of the pixels. Second, at the time of this incoming reset the corresponding pixel mask must not be set in the channel mask register (See Table 4.1). When both conditions the value of the local reset is recorded into a 32 bit wide FIFO shown in QpixRoute in Figure 4.1.

The composition of the data word is shown in Table 4.1.

Bit Location	Name	Function
0–31	Timestamp	Basic Datum which records the local counter at the time of the reset pulse.
32–35	Y Position	Assigned Y position in tile.
36–39	X Position	Assigned X position in tile.
40–55	Pixel Mask	Pixels which were issuing a reset at this time.
56–59	Word Header	Header value, which is command to all packets.
60–63	Reserved	Unused bits for all packets.

Table 4.3: Data word composition.

## The Local Data Packet

The transmission of the reset data from the local FIFO to adjacent neighbor nodes begins when an incoming register request from the aggregator is received. This request is supplied as register request to the command register ( 4.1). This request may be considered either a “hard” or a “soft” interrogation command.

The difference between the two types of an interrogation command is whether or not the event end packet is created. In the case of a “hard”–interrogation, the event end packet is always created, regardless of the local FIFO. In the case of a “soft”–interrogation, the event end packet is created only if the local FIFO is not empty.

The use of two different types of interrogations allows the aggregator control flexibility in how many packets are created during an interrogation. Interrogations may happen on timescales much more quickly than expected resent pulses ( $O(10^1$  s), Chapter ??). The ability to request data only if available prevents an over abundance of packets which prevents needless data transfers, reduces remote FIFO buildup, and conserves power.

## The Event End Packet

The event end words perform multiple functions. First, they may used as checksums to indicate at the aggregator node, or on disk, that this node has successfully transmitted all of its data. Secondly, the event end word, since it is necessarily 64 bits long, may also transmit its own timestamp with the excess bits. The timestamp that the event end word carries is the time that the time that the node received the broadcast. This timestamp is used in the frequency calibration of the node; the

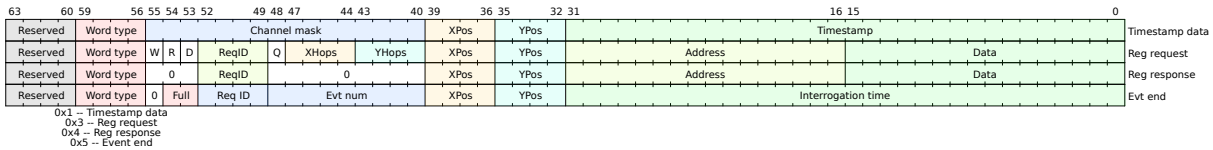


Figure 4.2: Example of Datum words and their allocation as currently implemented in the simulation and first prototypes.

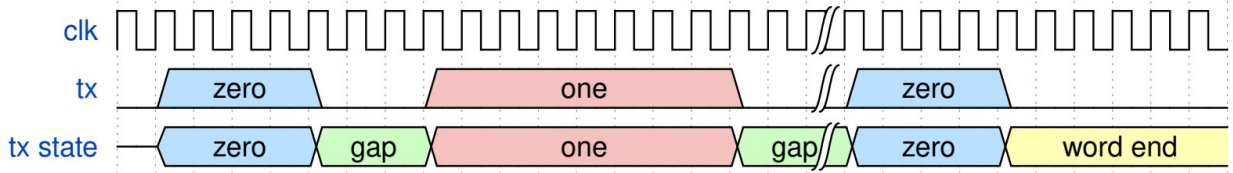


Figure 4.3: Diagram of the endeavor transmission (Tx) protocol.

method for calibration is described in greater detail in Section 4.6.

### Debug and Future ASIC Prototypes

Finally, The last block in Figure. 4.1 is the QPixDebug. This portion is used to expose certain ports to the physical pins in a digital ASIC design. This design will be the first prototype of the digital ASIC, and is beyond the scope of the work presented here, but will be discussed in the final section of this thesis.

### Inter-Node communication via endeavor protocol

The Endeavor protocol is a bi-directional serial communication protocol which allows communication between asynchronous devices. The asynchronous communication is achieved by extending the length of time that each bit is sent between the two devices. In this protocol the way that the receiving node (RXN) identifies the correct logic value of the current bit is by counting the number of clocks that the incoming signal is logic high. The incoming bit is either a logic low, if held high for fewer clocks than it would be if it was an incoming logic high. The number of clocks which correspond to high and low must be programmed beforehand and are tunable parameters.

## **Basic System Requirements**

The sheer number of pixels required for an APA (and the 10 kT entire module) require an effective means of charge and time calibration, stable buffer depths, and protection against single-point failure (SPF). Resets are records of a local counter at the current node and are recorded in response to a reset pulse sent from a pixel.

## **Comments on Data Rates and required Computing**

Based on the minimum number of bits for each RTD ?? we can estimate minimum data rates based on tile size.

## **4.2 The Digital Finite State Machine**

The Finite State Machine (FSM) of the digital ASIC outlines the designed behavior response to input. Figure 4.2 shows a representation of the different states as well as the conditions to enter or leave each state.

There are two different kinds of prompts that an ASIC can receive: packet transactions from neighbors and resets from pixels. When an ASIC receives a packet from a neighbor, the packet data are written on the remote FIFO There is one special packet

- Idle, Acquisition State
- Transmit Local
- Transmit Finish
- Transmit Remote
- DONE

### **Idle**

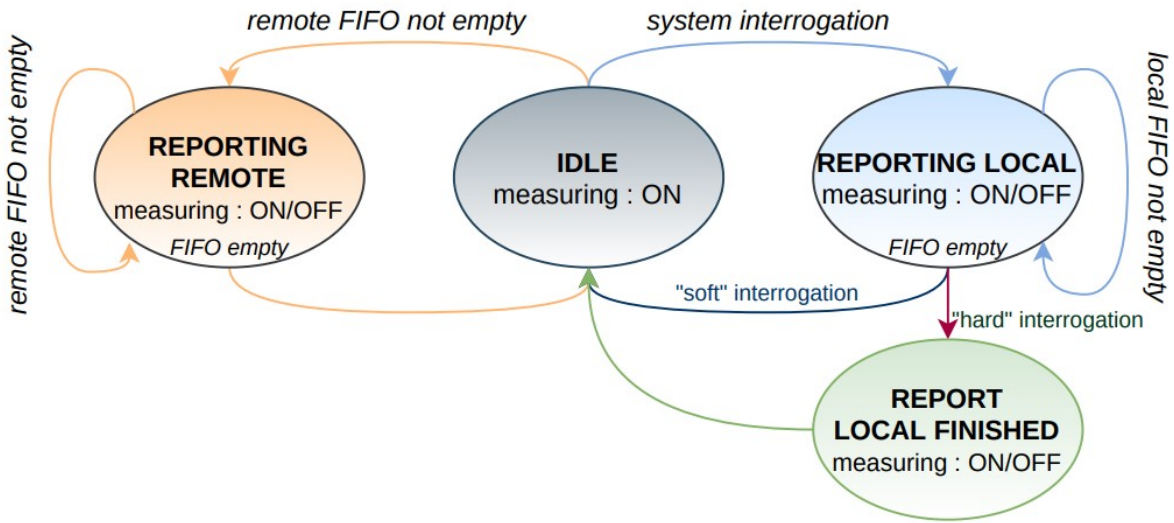


Figure 4.4: Diagram of the Digital node's FSM which determines how to respond to incoming packets.

## Transmit Data

### Transmit Remote

## 4.3 The Parameter Space of the Digital System

The digital back-end design

### Buffer Depth Requirements

The required buffer depth of each node in an array is the maximum number of timestamps the node can store in memory before overflow (dataloss). Each node requires some buffer memory to record local data as well as separate storage for remote data. The remote data which can be sent can come from any of the adjacent connected nodes, and may of any type: data words, register request, etc. Since the remote

The ice40 FPGAs have a total of 20 Embedded Block Ram models (EBRs) which allow for a total of 64xTODO memory depths allocated in each node.

Name	Function	Value Range
Zero	Controls how many clocks to send a logic high to transfer a low bit	1–3
One	Controls how many clocks to send a logic high to transfer a high bit	2–5

Table 4.4: The address values are not sequential because some registers have become deprecated through development.

### Endeavor Packet Stability at Different Scales

We test two different scales for the endeavor protocol. This protocol maintains a relative relationship between the number of high signals used to send either a high and low bit. The convention to send a high bit is to pulse a logic high signal for twice as long as is done for a low bit.

The number of bits used for to send a high bit are either

### The Push and Pull Architectures

#### 4.4 The Digital Back-end problem

The main objectives of the digital back-end are to correctly measure the data presented to it by the analog front-end and ensure lossless transport of that data to disk. More simply, the goals of the digital portion of the Q-Pix readout are to record and send data. We note that the successful completion of these two objectives to be goal of these simulation studies.

#### The Basic Datum

We begin with a discussion of the basic datum and mention initial design choices at the physical connection interface. The structure of this datum determines the buffer widths and depths required to store the data at the local ASIC level as well as the protocol used to transfer this data between ASICs and eventually out of the detector.

The minimum data which needs to be recorded are the timestamp, the relative location of the digitizing ASIC within the detector, plus any channels which were responsible for this reset. Each of the number of bits assigned to recording these parameters are a design consideration. We choose the number of bits for the timestamp ( $N_T$ ) to be 32, which prevents frequency wrap-around based on a fast clock frequency (Equation ??). We choose as the number of bits to assign a location ( $N_{loc}$ ) to be 8, which provides a maximum possible number of unique positions before aggregation

to be 256. Next, since the number of pixels (required by analog front-end design) is 16 we choose this number as the number of bits to represent a “mask” ( $N_{bits} = 16$ ). We need to record all of the channels during each reset since it is technically possible (even if less likely) for multiple analog channels to provide a reset within the same clock window.

We calculate the minimum number of bits per datum to be:

$$N_{bits} = N_T + N_{pix} + N_{loc} = 32 + 16 + 8 = 56 \quad (4.1)$$

Since buffer memory addresses and widths are normally characterized by powers of two, we can construct the basic datum size above the minimum number of bits provided by 4.4 to get  $N_{datum} = 64$ . The remaining bits are useful for constructing different types of packets to be used by the digital ASICs for additional uses such as register configuration or to provide packet identification.

## Communication of the Datum

There exist many asynchronous protocols of communication of digital information. Most of the differences between protocols exist based on the number of connections between devices and whether or not one pin is allocated to share a clock, etc.

Our design considerations for this readout include reduction of SPF risk, low power, and minimal routing. Partly for these reasons, the design choice for communication relies on only two connections between ASICs. One connection is defined as a data receiver (Rx) and the other as a data transmitter (Tx). This choice of interface dramatically limits a choice of possible protocols. Here, we describe the difference between two that we tested: Universal Asynchronous Receiver-Transmitter (UART) and Endeavor. We discuss and test only these two protocols for simplicity, and find it instructive to compare a proven and custom protocol (Endeavor) with a very common one (UART).

The importance of choosing a correct protocol is to ensure lossless data transmission. Since there are free running clocks, an asynchronous communication protocol is required. The way to ensure that data can be moved between clocks of different speeds is to stretch the signal or to repeat bits. The more the word is stretched in time, the larger the allowable difference in frequency between the two devices. However, this lengthening can't proceed forever, obviously, otherwise data transmission time could exceed data capture rates.

It is another important design consideration, then, to ensure that transactions proceed as quickly as possibly without data loss. Additional concerns of long data transactions include the use of more clock cycles which use more power and increase the risk noise to leak to the analog front-end.

## Endeavor

This protocol is slower than UART, but allows for approximately double the frequency difference:  $\approx 20\%$ .

The endeavor protocol relies on repeating the value of a high-bit, (digital '1' value) for an integer number of clock cycles. The receiver continually samples in incoming data transmission and counts the number of clock cycles that the signal was high for. The longer the signal was high, the more likely it is the the transmitter was attempting to encode a high bit, and vice versa.

The number of clock cycles which accompany either a high bit transmission or a low bit transmission then represent a possible design choice for the protocol. The actual number of bits which should be used ultimately depend on the similarity of the frequency between adjacent digital channels; the more similar the frequency (and relative phase) the lower these numbers can be.

- Start Bit
- High Bit
- Low Bit Send
- Stop Bit Send

## 4.5 Constraining the digital back-end Design

Section 2.2 describes in detail how a Q-Pix based hardware readout architecture could fit within a single DUNE-APA. Here we extend this discussion and use those constraints as the starting point for a search for a solution to the digital back-end architecture. The first problem to solve is how to aggregate the all timestamp data supplied by the large number of channels within a DUNE-FD APA.

A Q-Pix architecture would likely use either a high-performance FPGA or a custom ASIC to aggregate the large number of ( $O(10^7)$ ) channels. The number of aggregated digital channels

determines the required capabilities of the aggregator node and the selection of an FPGA or ASIC. Since each additional aggregator node represents an additional SPF risk, our design goal suggests that the optimal configuration is one that produces the least number of aggregator nodes. Therefore, the goal is to design a routing architecture which is responsible for as many digital channels as possible for each data aggregator node which still allows for accurate timing calibration and lossless data acquisition.

However, as one increases the number of digital channels per aggregator node one also increases the amount of local oscillators per aggregator, each of which must be calibrated. Additionally, since each digital channel requires extra communication time (as discussed in section 4.4) the introduction of more channels negatively affects the precision of timing calibrations and potentially increases SPF risk of digital channels. We consider then that an optimal number of digital channels per aggregator node is one that maximizes the number of digital channels but still maintains the required timing calibration (Sec. ??) and transmits lossless data.

We refer to the total number of digital channels collected from one pathway to an aggregator as a tile. In a fully realized design an aggregator might in fact be responsible for multiple tiles, which need not necessarily be the same size. The requirements of an aggregator node is completely determined by the composition of tiles it is connected to. Then, a parameterization of the data requirements imposed by each tile can be extended to describe the requirements of the aggregator node. Finally, we reach the conclusion that the required parameterization of the back-end system relies on the parameterization of the tile.

A tile is composed of inter-connections between digital channels. The LArTPC design suggests that each digital channel have a maximum of four connections since the collection of charge happens on a flat two-dimensional anode plane. Therefore, a two-dimensional routing requires at least two independent communication channels, which if we require the digital channels to allow bi-directional communication, the minimum number of channels is four. We use this number as a starting point for the digital channel design. These four connections per channel immediately creates a rectangular connection structure for a tile.

We note here that in order to meet other physical design requirements to fit into a pre-existing APA frame, the capability of the aggregator nodes could be increased to be responsible for more tiles, which would reduce the cable and hardware engineering considerations. However, further consideration here is beyond the scope of this work.

## Tile Routing Considerations

??

A tile is a rectangular composition of digital channels which must provide a path to all digital channels and send lossless data to the aggregator. Since there is one connection between a tile and the aggregator, there is one special node within the tile that connects to the aggregator. This special node we refer to as the “base-node” as all data and instruction commands, regardless of routing, must pass through this node. The symmetry of the rectangular tile allows any corner node to be the base node, and we choose the upper-left to define a convention. An example of a tile with a Corner base-node is shown in Figure 4.5.

We do not consider possible configurations where an aggregator might be connected to a digital channel within a tile since we require that all digital channels are identical and fully connected. We require identical channels as a practical choice due the required number of total channels. We also require the tile to be fully connected to allow as many possible unique paths between the base-node and the other nodes which provides maximum protection against SPF. We address that we discuss why we do not consider base-nodes placed on the outer edge of a tile, but not at the corners more generally in section 4.5. Briefly, base-nodes which are along the outer edge of a FCT but not at the corners simply contain two sub-graphs of FCT with a base-node along the edge. Therefore, an analysis of the constraints of a FCT with corner base-nodes can be mapped to an analysis of FCT with edge base-nodes.

Here we introduce a particular representation (based on graph-theory) for a tile which is useful for simplifying simulations and for analyzing particular routing configurations. The most general tile configuration occurs when we assume that all adjacent nodes within the tile are connected; this creates what we refer to as a “fully connected tile” (FCT). An example of a FCT is shown in Figure 4.5. Any particular choice of an effective routing must then be a subset of this fully connected version.

To elaborate on the adjacency matrix of the FCT we consider an  $2 \times 3$  tile. A  $2 \times 3$  tile has six total nodes, where we consider the upper-left most node to be the base node. Then, the unweighted

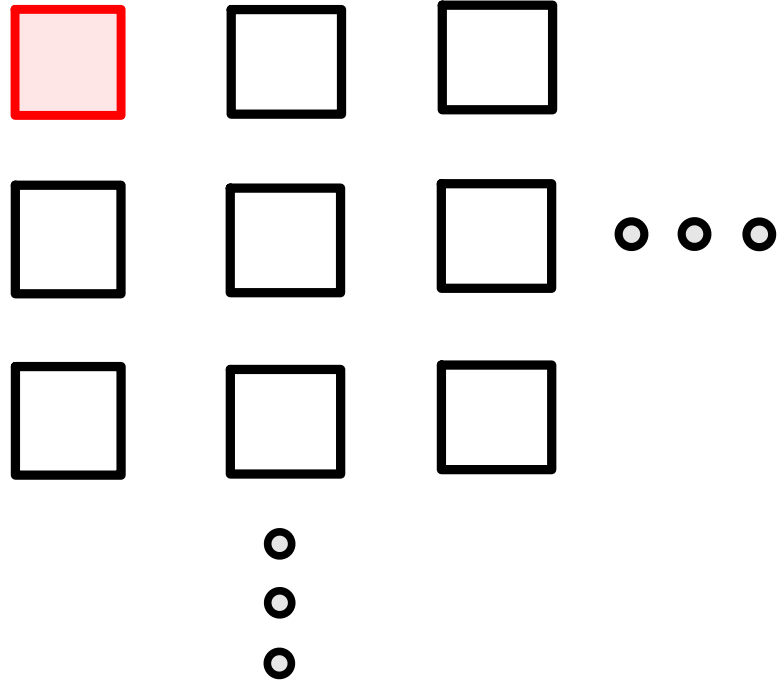


Figure 4.5: Example of an Corner Base-Node configuration. The base-node is colored and highlighted in red.

adjacency matrix has dimensions  $6 \times 6$  of the form:

$$M = \begin{pmatrix} 0 & 1 & 0 & 1 & 0 & 0 \\ 1 & 0 & 1 & 0 & 1 & 0 \\ 0 & 1 & 0 & 0 & 0 & 1 \\ 1 & 0 & 0 & 0 & 1 & 0 \\ 0 & 1 & 0 & 1 & 0 & 1 \\ 0 & 0 & 1 & 0 & 1 & 0 \end{pmatrix} \quad (4.2)$$

Where each non-zero value of  $M_{ij}$  represents a connection between nodes  $i$  and  $j$ . As an unweighted, undirected graph this is a symmetric matrix.

In practice each digital channel within a tile is actually controlled by a unique, free-running oscillator. Therefore, we can define the length of each edge between nodes as the length of time to send of a packet of data between two nodes ( $T_{i \rightarrow j}$ ). With this we can extend the model the adjacency matrix as a weighted and directed graph if we recognize that the non-zero elements of

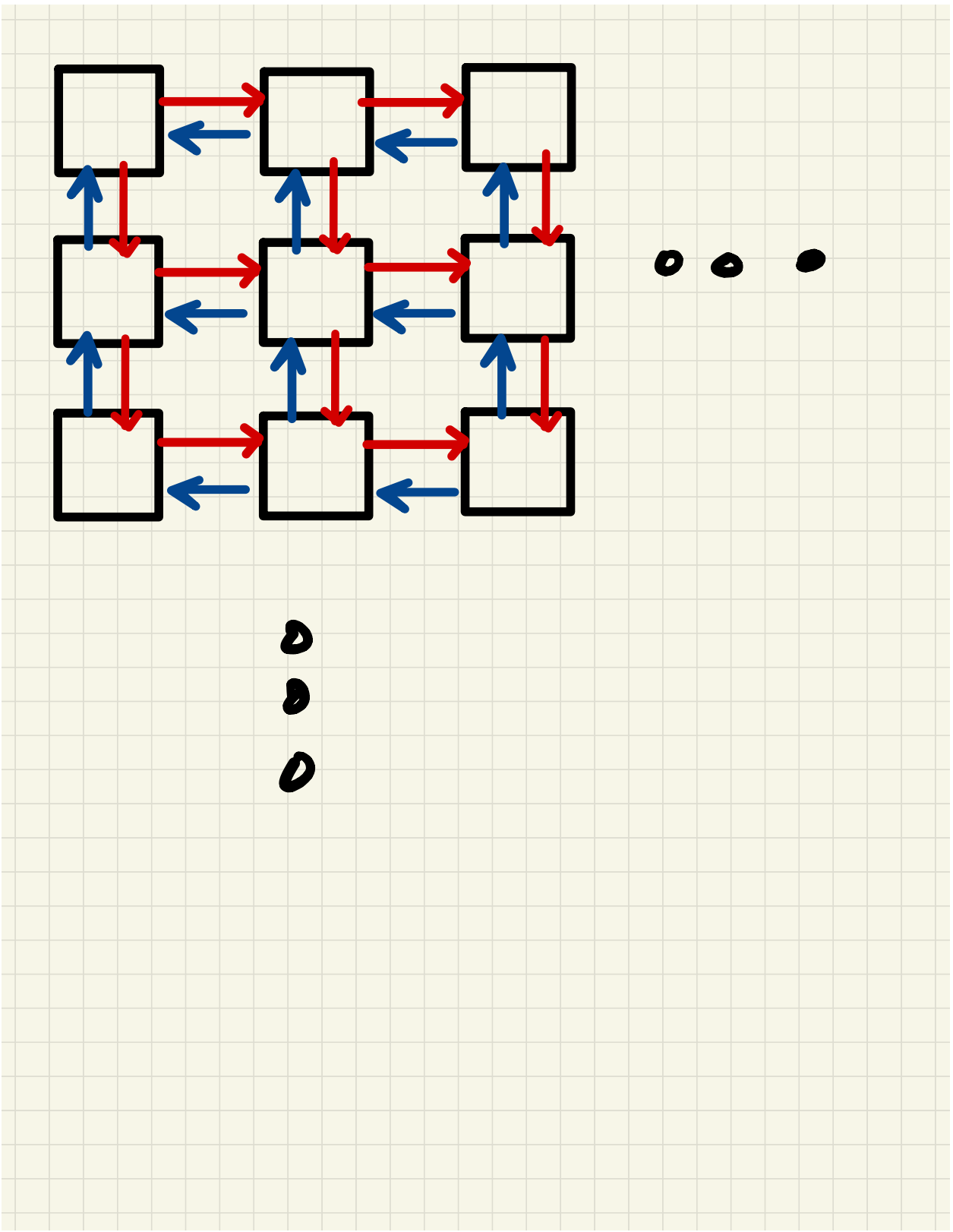


Figure 4.6: Example of the fully connected routing configuration for a tile (FCT). Each Node represents a digital channel which must be aggregated, and the red and blue connections distinguish directions of communication. The red connection lines indicate pathways away from the base node, whereas the blue lines represent connection paths towards the upper-left.  
65

$M_{ij}$  become  $T_{i \rightarrow j}$ , or the length of time it takes for the  $i^{th}$  local oscillator to transmit a packet to node  $j$ .

We can generalize this matrix in terms of an arbitrary number of rows ( $r$ ) and columns ( $c$ ). We define a convention of numbering nodes within the tile in terms of increasing column number followed by increasing row number. With this convention we obtain the general adjacency matrix with values defined by:

$$M_{ij} = T_{i \rightarrow j} (\delta_{i,j=i \pm 1} + \delta_{i,j=i \pm r}) \quad (4.3)$$

An adjacency list can similarly be constructed from Equation 4.5 where the non-zero connections are given by the kroniker-deltas factors.

The length between the nodes represents the time it takes for a packet to transact from one node to the next. This is determined by both the number of clocks to be sent in the communication protocol ( $N_{bits}$ ) and the period of the transmitting and receiving oscillators,  $T_i$  and  $T_j$ , respectively. Unlike the transmitter, the receiver only affects the transaction time with a single clock cycle, as the protocols we test here, (UART and Endeavor), each conclude a packet transaction when the receiver records the last bit transaction from the transmitter.

The full length between two nodes,  $i$  and  $j$ , connected by an edge is represented by:

$$T_{i \rightarrow j} = N_{bits} T_i + T_j(t) \quad (4.4)$$

where  $T_j(t)$  represents the time dependent fractional part of one nominal clock period of the receiving node. The expectation value of  $T_j(t)$  is half of the nominal window so that mean Equation 4.5 is:

$$\bar{T}_{i \rightarrow j} \simeq N_{bits} T_i + \frac{T_j}{2} \quad (4.5)$$

Since the transaction time of a packet is much larger than a single clock cycle ( $N_{bits} \simeq O(10^2) \gg \frac{1}{2}$ ), we can approximate Equation 4.5:

$$\bar{T}_{i \rightarrow j} \approx N_{bits} T_i \quad (4.6)$$

This representation is also useful to model certain SPF where a node becomes inactive. Dead or inactive nodes are ones in which all of their connections are effectively disconnected. This is equivalent to setting their transaction lengths to zero:  $T_{SPF} = 0$ .

We comment that although it is possible to construct tiles where more than one node connects to the aggregator, we observe that this configuration simply produces two effective tiles. These distinct tiles then are the data paths which are unique to each base-node. In this graphical representation a packet of data can follow one, and only one path from the origin node to the base-node unless there was duplication of packets. We emphatically avoid designs which might depend on data duplication for redundancy; these two base-nodes are in unconnected graphs.

Additionally, it is possible to connect non-rectangular tiles, but these tiles are effectively a larger rectangular tile with disconnected nodes to produce the desired shape. Since every node is designed to be robust in the full version, it will be robust in the subset.

We can apply this same argument to base-nodes which do not lie at the corners of the rectangular tile. In the case where the base-node is selected along the edge Therefore, we conclude that the analysis of the tile with the above adjacency matrix and a selection of the base-node at the corner of a rectangular corner provides the basis problem to the tile configuration.

### The SPF Cost

We define the average SPF cost as the amount of nodes that will be lost during a transaction as the number of digital channels at a height below the failed digital channel. For example, the number of nodes which are lost if a leaf-node fails is one since no other channels are between it and the data node. Likewise, the number of nodes which are lost in the event of a base-node failure is the total tile,  $N$ .

We can then calculate a mean cost SPF,  $C_{SPF}$ , :

$$C_{SPF} = \frac{1}{N} \sum_{node} \frac{n_i}{N} = \frac{1}{N^2} \sum_{node} n_i \quad (4.7)$$

### Minimize Occupancy

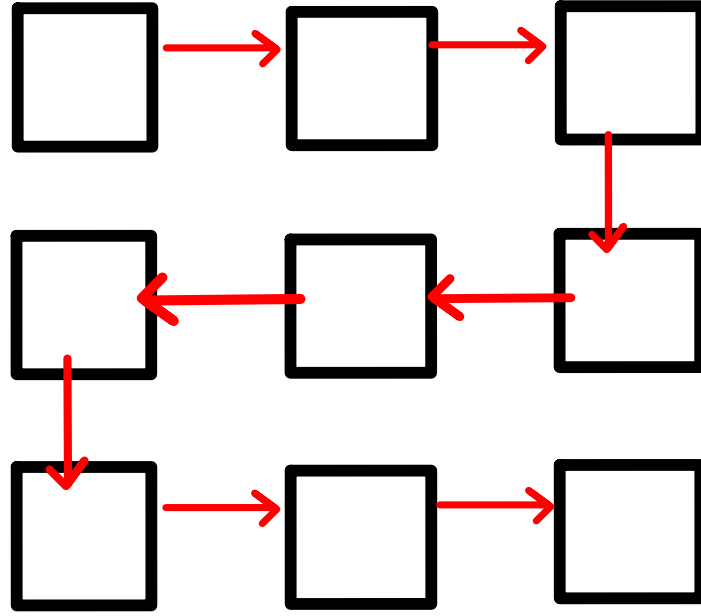


Figure 4.7: Minimal Occupancy Path of a FCT. This routing path ensures that the number of input connections equal the number of output paths for the node.

One of the goals of a successful digital design is to ensure lossless data transfer. One point of failure on the digital side is an overabundance of data arriving at a single layer within the tree. This data loss occurs when data are sent to a node faster than the data leaves the node, and persists for long enough such that the buffers of the node overflow. This creates a horrible loss of data which can't be recovered.

A routing scheme which minimizes the overall occupancy in the tree depths is shown in Figure 4.5. We refer to the style of routing as "Snake"-routing (SR), because this is also the longest possible routing scheme for a square tile.

We inspect the SPF risk from this routing scheme with Equation 4.5, where we notice that the  $n_i$  of each node is simply a running sum from the leaf to  $N$  at the base node.

$$C_{SPF} = \frac{1}{N^2} \frac{N(N+1)}{2} = \frac{1}{n} \frac{N+1}{2} = \frac{1}{2} + \frac{1}{2N} \quad (4.8)$$

Equation 4.5 tells us that the SPF risk of this routing configuration converges to half as the size of the tile grows. Intuitively, this makes sense, since it is equally likely to select a node close to the base-node as it is far away, which implies that the sum should converge to half the tile size for large  $N$ .

Although this routing scheme provides the most lax constraint on the required buffers at each digital channel, it provides the longest average path between the base node. The longer the transaction delay between the base-node and other nodes increases the reconstruction time uncertainty. Therefore, a natural alternative routing scheme is one that minimizes the communication scheme.

### Minimize Delay

For any given node in an edge FCT with location  $(R_i, C_i)$ , the shortest path to the base-node is simply the sum of its coordinates:  $R_i + C_i$ . An example of such a routing configuration for a tile is shown in Figure 4.5.

We can calculate  $C_{SPF}$  for this routing configuration if we identify that there are a  $C$  number of rows which sum from one to  $R - 1$ . Likewise, the far-left column in Figure 4.5 shows that the number of rows,  $R$ , sum from one to  $C$ . We can rewrite the sum over all nodes in Equation 4.5 as:

$$\sum_{node} n_i = C \sum_{i=0}^{i=R-1} i + R \sum_{i=0}^{i=C} i \quad (4.9)$$

We simplify the running sum of each term in Equation 4.5:

$$\sum_{node} n_i = C \frac{R(R - 1)}{2} + R \frac{C(C + 1)}{2} = RC(\frac{R + C}{2}) \quad (4.10)$$

Using this result we obtain  $C_{SPF}$  by identifying  $N = RC$ :

$$C_{SPF} = \frac{1}{N^2} \sum_{node} n_i = \boxed{\frac{R + C}{2RC}} \quad (4.11)$$

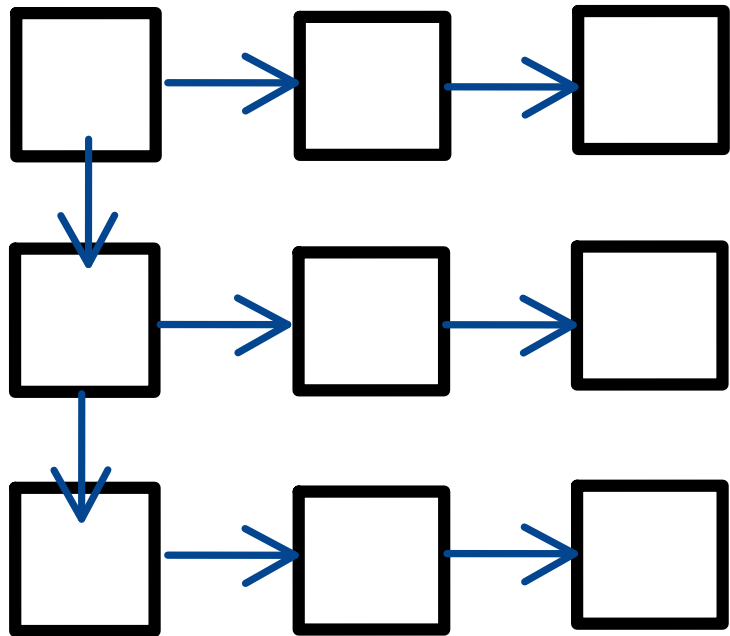


Figure 4.8: Minimal Delay Path of a FCT. This routing path ensures that the minimum number of transactions occur from every node in the FCT to reach the base-node. For any node along any column this is equivalent to the sum of the row and column of that node.

This result informs that relative cost of losing a node tends to zero as the size of the tile grows. Again, this result can be obtained intuitively, since as the number of columns (or rows) grow in size, the probability of a single failure occurring on the aggregator column is increasingly less likely.

### Broadcasts to avoid SPF

In order to protect against SPF we only consider designs which implement the FCT, since SPF can occur on any node the most robust connection scheme is the FCT. A FCT allows searches to probe all possible paths to any node via a “broadcast” produced from packets sent by the aggregator to the base-node. Therefore the broadcast algorithm can be represented by a complete circuit which begins at the base-node and proceeds to a target node with no repeated nodes until the target node

is reached. The backward path is then completed in reverse by following the edges (connections) between each node until arriving finally again at the base-node.

In practice, we encode the broadcast packet with a special header, to differentiate it from a request packet. To differentiate broadcasts an identification number is also included in the packet. Then, any node which receives a broadcast packet will record the identification number of the most recent broadcast, which it uses to discard repeated broadcast packets that arrive with the same identification number.

In the event that a particular node becomes inactive it will “block” data coming from the nodes along its path. In this case, there must be some sort of “broadcast” originating from the base-node that would allow information to traverse regardless of the effective routing path.

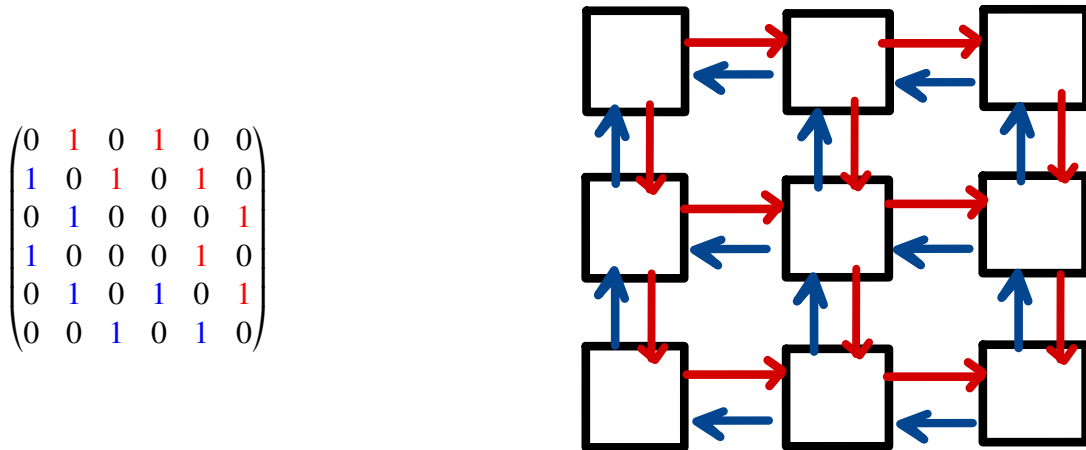


Figure 4.9: Minimal Routing Path of a FCT. This routing path ensures that the number of input connections equal the number of output paths for the node.

### Comments on the Edge Base-node and Other Routings

We discuss here the case of a FCT with an edge base node. An edge base node (EBN) is a digital channel that connects to the aggregator and to three other digital channels within a tile. Like before, this base-node must provide a unique path during data transmission to all digital channels within the tile. In this configuration the adjacency matrix is still the same as given in Equation 4.5.

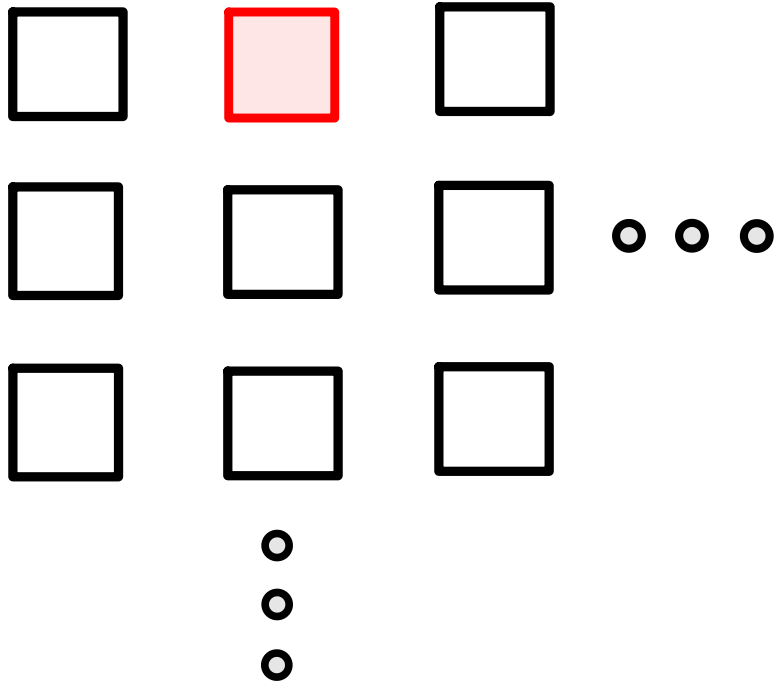


Figure 4.10: Example of an Edge base-node configuration. The base-node is colored and highlighted in red.

Also, as before, we wish to inspect different routing scenarios for a tile of a given square dimension of  $R$  rows and  $C$  columns. We can proceed by dividing the FCT graph into two subgraphs,  $S1$  and  $S2$ , where  $S1$  represents the rectangular section of the graph below and to the left of the EBN, while  $S2$  are the remaining channels.

We identify that while the number of columns ( $C$ ) in tile is equal to both subgraphs, the total number of rows  $R$  of the tile is equal to the sum of the rows from these two subgraphs:  $R = R_1 + R_2$ .

The EBN then is actually just a composition of two subgraphs which are each equivalent to The tree characteristics which determine requirements for the digital channels are the tree height and total occupancy at each level. Therefore, since the EBN provides no difference in either of these characteristics and is a suposition of two fundamental CBN, an analysis of an EBN is equivalent to the analysis of a CBN.

However, we do remark comment that the average difference of the relative weights of each node

in a SPF analysis are different in a EBN compared to the CBN case. This should be obvious since the relative weight of each node is determined by the running sum of the path length between the base-node and its leaf. For a fixed row dimension,  $R$ , the EBN offers a smaller average tree height for each of its component radii  $R_1$  and  $R_2$ .

Therefore, in a EBN tile, with two subgraphs of radii  $R_1$  and  $R_2$  where the base-node is on the  $R_1$  edge. The total sum of the weights of all nodes in the tile are the sums of the two subgraphs plus  $CR_2$ , which is the average weight of the nodes from the subgraph  $R_2$  when it connects to  $R_1$ .

$$\sum_{node} n_i = \sum_{R_1} + \sum_{R_2} + CR_2 \quad (4.12)$$

Equation 4.5 gives the general formula for calculating the SPF risk for a EBN case, depending on the routing methods of subgraphs  $R_1$  and  $R_2$ . We can treat these sub-graphs as in equation 4.5 to obtain:

$$\sum_{R_1} + \sum_{R_2} + CR_2 = \frac{R_1 C(R_1 + C)}{2} + \frac{R_2 C(R_2 + C)}{2} + CR_2 \quad (4.13)$$

We use this result to obtain the relation of the general  $C_{SPF}$ :

$$C_{SPF} = \frac{1}{N^2} \left( \frac{R_1 C(R_1 + C)}{2} + \frac{R_2 C(R_2 + C)}{2} + CR_2 \right) \quad (4.14)$$

if we identify that  $N = C(R_1 + R_2)$  and use  $R_2 = R - R_1$ :

$$C_{SPF} = \frac{1}{2CR^2} (2R_1^2 - 2R_1R + R^2 + CR + 2(R - R_1)) \quad (4.15)$$

## 4.6 Frequency Calibration of Local Oscillators

The Q-Pix calibration requirements are described in detail in Section ???. The important parameters which must be calibrated for each pixel are the charge per reset and the frequency of the local oscillator. An aim of this work is to demonstrate an additional frequency calibration method using the minimal required connections between each digital node.

Any method of a frequency calibration must synchronize time measurements between all digital nodes within a tile and the aggregator. There are several possible methods to achieve this, but ultimately the data that are recorded must be some time at the aggregator,  $T_a$ , and the time at any specific node,  $T_j$ .

A direct method is one where the aggregator distributes its own clock to all nodes in the tile. This scenario removes the need for a calculation of the frequency of each node altogether since the clock of each node is already known from the aggregator. This is the simplest case for timing calibration: remove all free running oscillators. However, this method also introduces complex routing and power requirements within every tile.

A distributed clock network indeed removes ambiguity of the remote oscillator frequencies, but at the cost of hardware complexity. Whether or not this design choice is preferred is entirely detector dependent, but likely increases in difficulty with the scale of the TPC.

We comment, however, that we ignore this scenario because it may altogether be unnecessary depending on future ASIC performance. In the event that frequency calibrations of sufficient precision ( $\bar{f} \approx 1\text{ ppm}$ ) are possible occur on free-running local oscillators future detectors would need only to acquire these ASICs and place them with minimal cost in terms of both time and money.

Another simple scenario is one where the aggregator itself connects directly to all nodes within a tile via a single connection which can be used as a reference trigger. This means that some trigger from the aggregator would issue directly into each node at the same time:  $T_a = T_n$ . To calculate the frequency in this manner, the controller would issue two triggers from the aggregator with a known time separation,  $T_o = T_{a2} - T_{a1}$ . The remote nodes would each record and send their timestamps back to the aggregator, where the time difference would be calculated as:

$$T_o = T_{a2} - T_{a1} = T_{n2} - T_{n1} \quad (4.16)$$

this is rewritten in terms of frequency as follows:

$$f_n = \frac{T_{n2} - T_{n1}}{T_o} \quad (4.17)$$

This calibration method extremely simple but introduces an additional connection to each node between itself and the aggregator. For a large scale system such as Q-Pix even this simple connection scheme introduces  $\approx 60 \times 10^3$  hardware points of failure per APA.

Both of these scenarios are valid implementations of a Q-Pix readout system. In both of these scenarios, however, there is added complexity into the hardware design of the system in the form of additional routing where each route which represents a possible point of failure.

In a world of perfect hardware and costless routing in terms of both time and money these routing schemes would clearly be sufficient. However, no hardware is perfect. Therefore we introduce and discuss a calibration technique which relies on no additional routing and could be optionally implemented even in the above schemes in the event of a failure. Therefore, even if not the primary implemented calibration technique, since this calibration introduces no superfluous routing it could still be used regardless of the actual future hardware implementation.

## A Minimal Connection Calibration Procedure

As stated in the previous section, any frequency calibration records a reference time at the aggregator ( $T_a$ ) and an event time ( $T_n$ ) at a node within a tile.

the time calibration procedure presented here requires only the minimal routing required in any Q-Pix readout system, where we assume time-dependent free-running local oscillators at each node within the tile.

The calibration procedure begins at a time ( $T_0$ ) where the aggregator sends a calibration packet.

Next, the packet propagates through the tile to some remote node,  $N_j$ . This node receives the packet later at some time  $T_{n1}$ :

$$T_{n1} = T_o + T_{f1} \quad (4.18)$$

Where  $T_{f1}$  is the propagation time of the packet from the aggregator to the  $N_j$  node.

This remote node then sends the packet with its time ( $T_{n1}$ ) back to the aggregator.

The aggregator will wait some calibration time ( $T_{cal}$ ) before issuing another calibration packet. This wait period ( $\mathcal{O}(10^{0-2})$ ) can be long compared to the full transaction time to the  $N_j$  node ( $\mathcal{O}(j * 10^{-5})$ ).

After the wait period, the aggregator will issue a second calibration packet to be sent to a remote node at time:

$$T_1 = T_{cal} + T_0 \quad (4.19)$$

Similarly to the first packet this packet will propagate to  $N_j$  with some new time  $T_{f2}$  where  $N_j$  will record time  $T_{n2}$ :

$$T_{n2} = T_1 + T_{f2} \quad (4.20)$$

Now, we define  $\Delta T_j$  as the difference in the two time measurements from the two packets sent from the aggregator. The time difference is related to the number of clocks that occurred between the two different measured values of the clock,  $T_{n1}$  and  $T_{n2}$ .

$$\Delta T_j = T_{n2} - T_{n1} \quad (4.21)$$

We use the known relationships for  $T_{n2}$  and  $T_{n1}$  to obtain:

$$\Delta T_j = (T_1 + T_{f2}) - (T_0 + T_{f1}) = (T_1 - T_0) + (T_{f2} - T_{f1}) = T_{cal} + \Delta T_f \quad (4.22)$$

Where we defined  $\Delta T_f$  as the difference in forward propagation times from the packets sent from the aggregator node at  $T_1$  and  $T_0$ .

We arrive at the result which compares the measured time at the aggregator  $T_{cal}$  and the time measured at each node,  $\Delta T_j$ :

$$\Delta T_j = T_{cal} + \Delta T_f \quad (4.23)$$

A perfect reconstruction of the nodal frequency would follow if  $\Delta T_f = 0$ . But it is sufficient to note that the wait period happens on the order of seconds, whereas  $\Delta T_f$  is on the order of  $\mu s$  or at least a six order of magnitude difference. We then use  $\Delta T_f \ll T_{cal}$  to obtain:

$$\Delta T_j \approx T_{cal} \quad (4.24)$$

We convert time into frequency with the difference of the timestamps measured and a known aggregator frequency ( $f_a$ ):

$$\frac{\Delta N_j}{f_j} = \frac{\Delta N_a}{f_a} \quad (4.25)$$

or,

$$f_j = \frac{\Delta N_j}{\Delta N_a} f_a \quad (4.26)$$

Where  $\Delta N_j$  and  $\Delta N_a$  are the differences in the timestamps of the 32-bit clocks at the remote node and aggregator, respectively.

## Packet Transaction Time

We next examine the approximation that  $\Delta T_f \ll T_{cal}$  and consider its contribution to the error in the reconstruction of  $T_j$ . This analysis also provides a constraint on the duration of  $T_{cal}$  to ensure an accurate measurement of each  $T_j$  in a tile. We begin by discussing how long it takes for a packet to traverse a tile.

The time it takes for each packet to be received by the next node is given in Equation 4.5. The value,  $N_{bits}$ , is the number of clock cycles used for the packet and is protocol-dependent. Since the protocol must be deterministic for each packet,  $N_{bits}$  must be the same for each transaction on the path from the base-node to the remote node.

As an example, the time it takes for a packet to go from the base-node,  $N_1$ , to a remote node,  $N_3$ , via the path  $1 \rightarrow 2 \rightarrow 3$  is determined by:

$$T_{1 \rightarrow 3} = T_{1 \rightarrow 2} + T_{2 \rightarrow 3} \approx \frac{N_{bits}}{f_1} + \frac{N_{bits}}{f_2} = N_{bits} \left( \frac{1}{f_1} + \frac{1}{f_2} \right) \quad (4.27)$$

Where,  $f_i$ , is the frequency of the clock at sending node. The approximation is within a single clock cycle of the receiving digital node ( $\approx 33$  ns).

Therefore the time it takes for a packet to go from the base-node to any remote node is proportional to  $N_{bits}$  multiplied by the sum of the edges in the full adjacency matrix given by Equation 4.5.

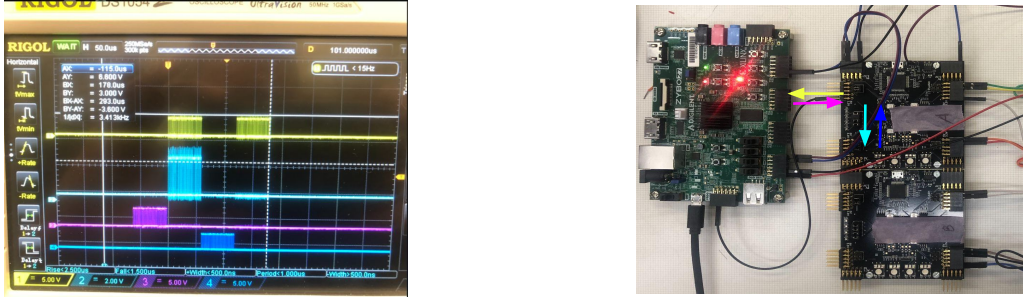
We generalize Equation 4.6 to represent the time it takes a packet to go from the aggregator ( $i = 0$ ) to any remote node,  $N_j$ :

$$T_f = T_{0 \rightarrow j} = N_{bits} \sum_{i=0}^{i=j-1} \frac{1}{f_i} \quad (4.28)$$

We require that every calibration packet on the protocol uses the same number of clocks ( $N_{bits}$  is constant) and follows the same path.  $\Delta T_f$  becomes:

$$\Delta T_f = N_{bits} \sum_{i=0}^{i=j-1} \frac{1}{\Delta f_i} = N_{bits} \sum_{i=0}^{i=j-1} \Delta T_i \quad (4.29)$$

We recognize  $\Delta T_i$  as the nominal time-dependent clock drift of the each local oscillator in the path between the base-node to the remote-node. We can provide an order of magnitude estimate for  $\Delta T_f$  if we assume a (very poor)  $\approx 1\%$  drift in each of the remote clocks within the tile during a period



((a)) Waveforms caught on an oscilloscope. The((b)) Example of arrows depicting the direction of the packets shown in the other image  
timescale is 50  $\mu$ s.

Figure 4.11

of  $T_{cal} \approx 1$  s. In this approximation we also assume that the mean of the periods of the nodes are the designed value ( $\approx 33$  ns) for which a 1% error gives  $\sigma_{T_f} \approx 3$  ps. If we assume that all of the clocks (for whatever reason) drift have error which drifts int he same direction (the sum doesn't cancel) then for 100 transactions with 1000 clocks per transaction, we obtain for  $\Delta T_f$ :

$$\Delta T_f \approx 1000 * 100 * 3 \times 10^{-12} \approx 30 \text{ ns} \ll 1 \text{ s} \simeq T_{cal} \quad (4.30)$$

## 4.7 The Digital Prototype Design

This section marks the second part of this chapter. We describe the design of a modular digital back-end prototype board. The results presented here construct a tile 4×4 array of Lattice ice40UP5k FPGAs. Each FPGA is programmed with the logic described in the previous sections.

These nodes are used to test the control logic, communication stability, buffer requirements, and calibration procedure which will be tested in the future Q-Pix digital prototype ASIC. The most important quantity to be calibrated for the digital nodes is the frequency of the local oscillator. The Q-Pix reconstruction for both time and z position are dependent on this parameter, see Chapter 2.

Future implementations of the digital back-end for Q-Pix may, of course, use different oscillators. However, these results are still beneficial as a proof of concept for the frequency calibration, as well as tests to the packet loss susceptibility. Packet loss is a function of relative frequency drift between neighbor nodes.

FPGA Position	Mean	STD	$\frac{\delta f}{f_o} * 1e6$ (ppm)
(0,0)	30000245.543	2.379	0.079
(0,1)	30000190.646	2.979	0.099
(0,2)	30000153.908	3.334	0.111
(0,3)	30000248.831	3.843	0.128
(1,0)	30000192.729	2.860	0.095
(1,1)	30000210.905	3.405	0.114
(1,2)	30000116.212	3.984	0.133
(1,3)	30000159.824	4.158	0.139
(2,0)	30000351.431	3.685	0.123
(2,1)	30000193.845	4.285	0.143
(2,2)	30000200.278	4.071	0.136
(2,3)	30000152.633	4.263	0.142
(3,0)	30000183.359	3.954	0.132
(3,1)	30000209.788	4.561	0.152
(3,2)	30000192.277	4.169	0.139
(3,3)	30000171.302	4.538	0.151

Table 4.5: FPGA calibration results based on hard interrogations at a frequency of 4 Hz.

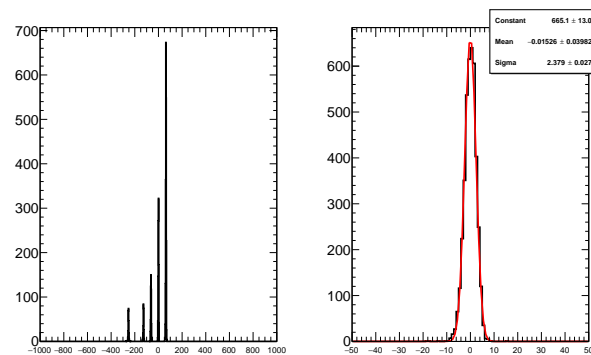


Figure 4.12: Example of frequency calibrations for the FPGA Adjacent to the Zybo.

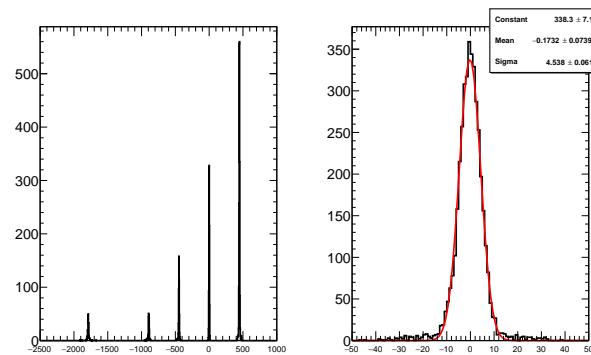


Figure 4.13

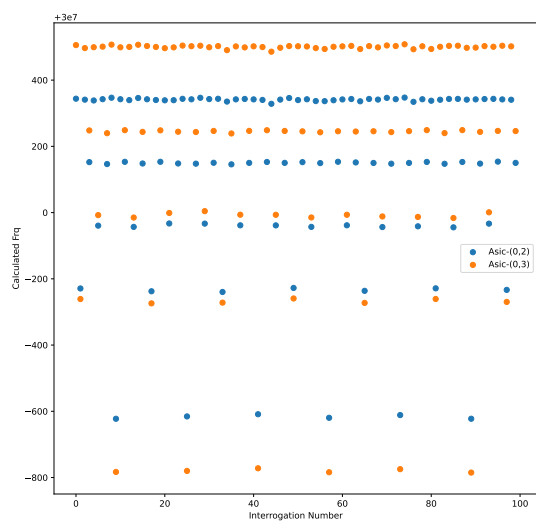


Figure 4.14

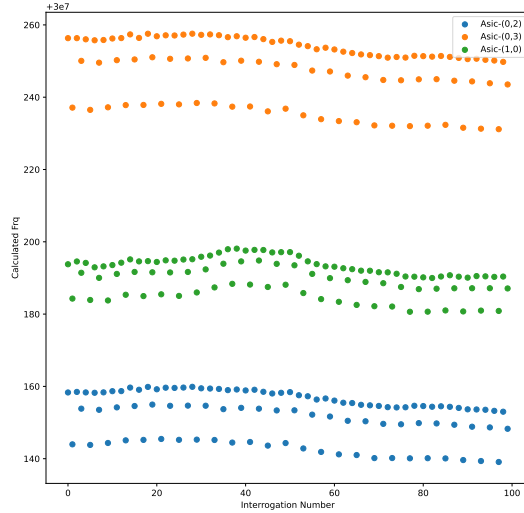


Figure 4.15

FPGA Position	Mean	STD	$\frac{\delta f}{f_o} * 1e6$ (ppm)
(0,0)	30000245.543	2.379	0.079
(0,1)	30000190.646	2.979	0.099
(0,2)	30000153.908	3.334	0.111
(0,3)	30000248.831	3.843	0.128
(1,0)	30000192.729	2.860	0.095
(1,1)	30000210.905	3.405	0.114
(1,2)	30000116.212	3.984	0.133
(1,3)	30000159.824	4.158	0.139
(2,0)	30000351.431	3.685	0.123
(2,1)	30000193.845	4.285	0.143
(2,2)	30000200.278	4.071	0.136
(2,3)	30000152.633	4.263	0.142
(3,0)	30000183.359	3.954	0.132
(3,1)	30000209.788	4.561	0.152
(3,2)	30000192.277	4.169	0.139
(3,3)	30000171.302	4.538	0.151

Table 4.6: FPGA calibration results based on hard interrogations at a frequency of 0.1 Hz.

## **Frequency Calibration of each Node**

### **4.8 Timing Stability**

We describe here the methods of measuring a stable time for different configurations of the nodes. We also comment on the results of the timing with respect to the minimum required timing sensitivity in order to have accurate timestamp reconstruction.

### **4.9 Power and Current Characteristics**

There are test pads on the PCBs used to measure the voltage stability of the different FPGA voltages. For each voltage, there is also a single  $1\ \Omega$  probe-resistor. This resistor is used to measure the relative current drawn from each of the voltage sections on the PCB.

### **4.10 Analysis of Systematics for Different System Implementations**

The essential features of the digital node in the Q-Pix readout are the properties of the local oscillator. The frequency, relative phases, and stability of the oscillator determine the power consumption, packet transaction time, minimum timestamp resolution, which determines maximum current measurements, and affects packet loss probability in larger tile systems. It is not an understatement to say that the successful development of the digital node relies on the development of the local oscillator.

### **4.11 Towards the Integration of the Aggregator Node**

In the studies presented here, The aggregator node which was used was the Zybo Z7-20.

### **4.12 Comments on A Super-DAQ-Node**

Each APA module within a larger DUNE module must ultimately be interconnected so that the entire module can be readout. As described above, a single modular tile is controlled by an individual DAQ node, where many constitute a complete APA. Therefore, we refer to the device that digitally multiplexes all of the DAQ node data as the "Super DAQ Node" (SDN). Then, we imagine the final multiplexing stage for an entire DUNE module as an array of SDNs, each of which consists of an array of DAQ nodes, where each DAQ node is a 2-D array of Q-Pix based ASICs.

The total number of request SDNs within the full dune module depends on the final size of a DAQ-node controlled tile.

### **4.13 The Back-End Summary**

## THE Q-PIX BACK-END AND SIMULATION STUDIES FOR FUTURE Q-PIX PROTOTYPES

This chapter explores the requirements of a Q-Pix based digital back-end readout targeted at a DUNE-FD module.

The first part of this chapter describes the digital simulation used to evaluate the possible designs presented in the previous chapter. The Q-Pix readout (Chapter 2) relies on several key factors which promise possible improvements over a traditional MWPC readout: automatic calibration from quiescent radiogenic background, an overall reduction in volume of data collection, and simpler analysis chain and vertex reconstruction, to name a few. However, this novel readout technique not only changes the front-end analog structure but also dramatically increases the number of digitization channels. The increase of the number digital channels and required ASICs creates the need for a new digital back-end design.

The second part of this chapter presents results from a physical simulation framework based on radiogenic backgrounds in LArTPCs as well as high energy ( $\approx 10\text{GeV}$ ) neutrino events. We use this physical simulation framework to address a number of design choices, since any sufficiently complicated design offers an intractible number of possible choices each of which can significantly alters the performance of a detector. A few examples of crucial design choices for the digital back-end are: the use of free-running local oscillators, the selection of an inter-ASIC communication protocol, the choice of inter-ASIC connections or routing profiles, and the buffer sizes of FIFOs to store charge-reset data. The goal of the simulation is to parameterize these design choices in order to provide an understanding of functional design targets and analysis of design tradeoffs.

The final part of this chapter synthesizes the results of the physical and digital simulations and provides a description of the effects of the most important parameters determined from these results. We use as inputs to the simulation the expected input charge from radiogenic background and beamline neutrino interaction over a  $2.3\text{m} \times 6.0\text{m}$  LArTPC. The characterization of the analog front-end, namely the charge characteristics per channel, is an on-going collaborative work whose results can be able to be applied here.

All results in this chapter are my own individual work.

## 5.1 The Tile Simulation Framework

The previous chapter introduced the digital back-end as well as discussed different design choices, namely tile size, routing configurations, and the effects of the aggregator position. Here we describe how we simulate events of interest for these different configurations.

A successful design is able to record and send loss less data for all events of interest. In a DUNE-FD LArTPC these sources range in intensity from sub-MeV-scale radiogenic backgrounds native to the LAr to 10's of GeV scale of beam neutrinos or atmospheric neutrinos. We consider the back-end design to be successful if and only if it provides the ability to fully capture and transmit of all collected resets from these sources.

We note that while it may be shown in the future that some resets may in fact not be needed for a reconstruction of particular events, we still assert that since Q-Pix is a novel readout, it is not yet possible to claim all scientific goals for which it may be used. For this reason we demand that no data be lost for any reason due to the digital back-end design.

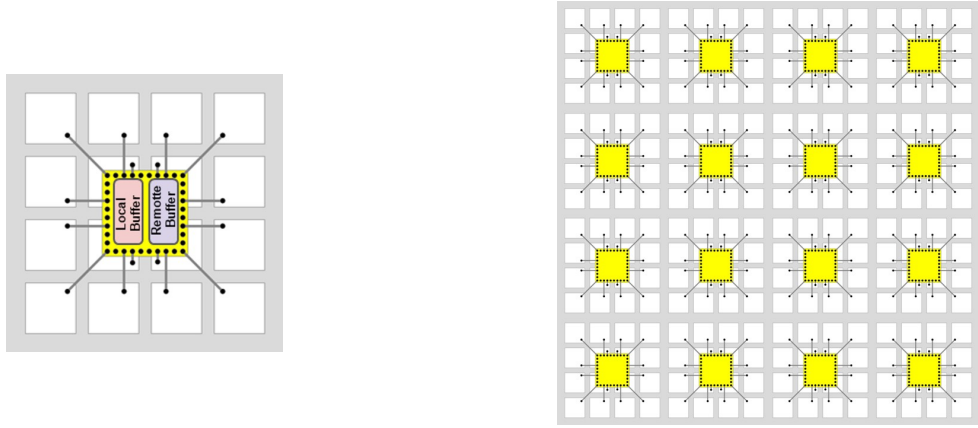
### The Tile Representation

We model a tile (a group of digital nodes, or ASICs) based on the description given in Chapter 4. A tile is then represented in software (Python 3) as a linked list of nodes which store pointers to the adjacent nodes or neighbors.

We note a distinction between the nomenclature used here. The term "node" refers to the simulated back-end ASIC whereas our use of "ASIC" refers to the first digital prototype.

Every node in the tile holds two FIFO objects which store local and remote data. The local and remote FIFOs keep track of the total number of resets or packet transactions, respectively. If a node records a new reset the local FIFO is then written to, and the local FIFO transaction counter increases. Similarly, the remote FIFO's transaction count is increased when a write occurs on this FIFO, which happens every time a digital node receives a packet from a neighbor node, including the aggregator node.

In the current Q-Pix digital ASIC design (see Sect. 4.2) all packets sent between neighbor nodes, with the exception of broadcasts, are written on the remote FIFO. At the beginning of a simulation step each node first checks to see if its received an interrogation request. If the node has received a soft interrogation request (see Sect. 4.5), and has data in its local FIFO, it will first send its data in the local FIFO, followed by the event-end packet. If the node receives a hard interrogation request,



((a)) Individual node with local and remote FIFOs.

((b)) Tile of node objects.

Figure 5.1: Composition of an example  $4 \times 4$  tile. Each node in the tile represents a digital ASIC which contains two FIFOs. One FIFO is used to store timestamps from reset data, which we refer to as the local FIFO. The other FIFO we call the remote FIFO and is used to store all packet transactions from neighbor nodes. The local FIFO is 48 bits wide, where 32 bits come from the timestamp and 16 bits are from the pixels. The remote FIFO is 60 bits wide, since it must store all relevant bits for the 64 bit packet word, where there are 4 unused bits.

the node will send local data, if any, and will send an event-end packet regardless of whether or not the local FIFO had any data. If the node's local FIFO is empty, and it has not received an interrogation, it will check the empty status of the remote FIFO. If the remote FIFO is not empty, this packet will be read and transmitted to its neighbors accordingly, otherwise the node remains in its idle state [4.2](#).

There are two types of remote data to send: broadcasts and responses. A broadcast is a register request sent to a digital node, which can only be created and sent from the aggregator node. The responses include all other kinds of packets sent from neighbor nodes which include: data packets, event-end packets, and register response packets.

The communication packet object is a custom struct object which uses an enumerated type to differentiate the kinds of packets that the digital node can read from its remote FIFO. Each simulated node's behavior to these incoming packets is mirrored to the digital FSM, shown in Fig. [4.2](#). When a node reads the packet from the remote FIFO it reads the enumerated type to determine how to communicate the packet to its neighbors, just as is done in the physical ASIC.

Also tested in these simulations are tiles which have a "push" architecture. This architecture

changes the condition for a node to leave its idle state and send local data whenever the local FIFO is not empty. For this reason the push architecture is also more time consuming to simulate since each node can send a packet at any time, provided that it will inject a hit into its local FIFO following the procedure described in the next section. Nodes which require an interrogation in order to send local data we refer to as the "pull" architecture.

## Injected Resets

In order to speed up the execution of the python simulation reset events are precalculated and loaded into separate list containers for each node. At the beginning of every simulation time step every node checks its injected resets list against the new simulation step time. If the new time step is larger than any of the timestamps in its resets list, the resets are then removed from this list and are written to the node's local FIFO.

Resets from simulated data whether radiogenic or neutrino data can occur at any pixel and at any time. The digital node (and the ASIC) is capable of recording multiple resets from multiple channels at the same time. This means that it is possible for multiple different pixel resets to only contribute to one local FIFO write. Therefore, extra care must be taken when adding injected resets with channel information.

In this simulation we consider the best case timestamp measurement for each reset, which is that each digital node can record a unique reset for each channel on every new clock cycle. Then, procedure for combining resets from multiple channels calculates the clock cycle (timestamp) for which this node would record a timestamp for a particular channel. If a reset has already been recorded for this channel, the uninjected timestamp is incremented by one clock period for this node. The above procedure then repeats until all channels have had all of their resets recorded on unique timestamps for the digital node, where only different channels can be recorded on the same timestamp.

## The Simulation Procedure

Upcoming sections will discuss values derived from simulating the readout of the tile. Here we briefly describe the simulation procedure and how the results are obtained. The procedure is also graphically demonstrated in Figure 5.1.

## Simulation Stepping Procedure

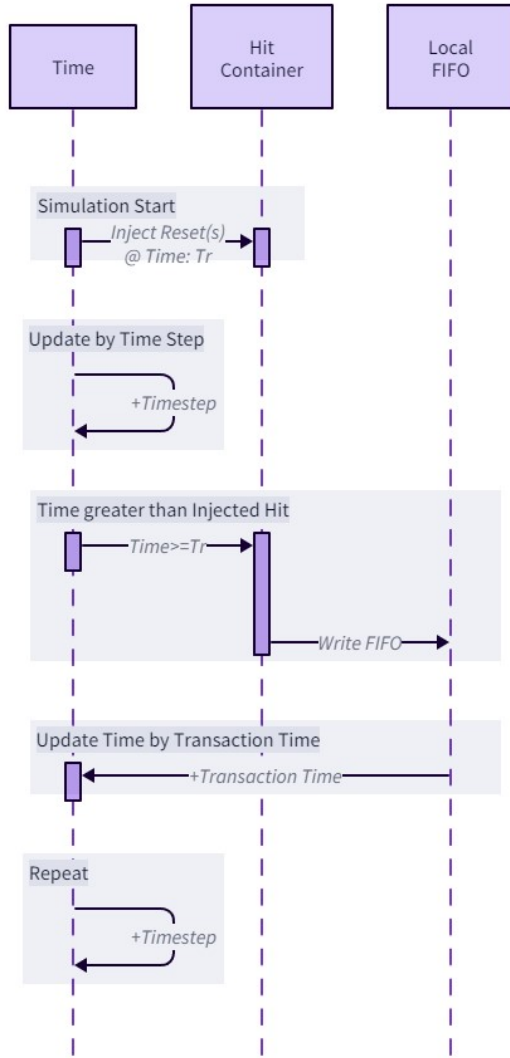


Figure 5.2: Example timeline for simulation time steps and injected hits. Before the simulation begins hits are added into a Hit Container for each node. When the simulation begins the time is incremented by a single time step ( $\tau = 1\mu s$ ). The time increments until it is larger than the time of any of the injected hits. The values of the timestamps are then moved from the Hits container into the Local FIFO, where the timestamp that is recorded is the soonest clock cycle after the "true" time of the injected hit. When the data are ready to be transmitted from the Local FIFO, the time is then updated by transaction time. An example of this procedure is shown in Figure 5.3.

The simulation loop iteratively processes a single transaction from a queue of transactions and then processes all nodes in the tile at incremental timestamps. The timesteps used in the simulation results used here are steps  $1\ \mu\text{s}$ . It is not necessary to perform smaller time steps than this, as packet transactions themselves are on the order of  $\approx 50\mu\text{s}$ , based on the endeavor protocol. If any processed node generates a new transaction(s), this transaction(s) is added to the transaction queue.

A transaction represents a 64-bit packet that is transferred between two nodes (Sect. 4.1). The sending node is responsible for calculating the true time when this transaction would complete. The receiving node records this byte onto its remote FIFO and performs the state check based on this packet according to Fig 4.2. Then the receiving node updates its time to its soonest clock cycle after this transaction completed. Next, each node in the entire tile is processed one forward timestep. If nodes are in the push state and receive a hit within this timestep window, they create a new outgoing packet, and add this packet to the transaction queue. We note that it is only possible for processed nodes which did not receive the transaction packet to create a new packet if they are in a push-based architecture.

The simulation is complete when all nodes have been processed up to the final requested time and no transactions are left in the queue. In the results presented here we process the tile for one second longer than any injected resets to ensure that the tile is fully read out.

## 5.2 The Tile Parameters

One goal of the simulations presented here is to parameterize different design choices in constructing both the digital nodes and the tiles. The different parameters which we test are described in Table 5.2.

There are a total of four parameters to test: frequency stability, tile size, routing, and architecture. Of the four parameters, we note that the frequency stability is the one parameter determined by the ASIC's physical design. Therefore, special care must be taken into account when designing the local oscillator for the ASIC. The other variables: routing, architecture, and tile size are either programmable registers or easily configurable in hardware layout.

It is intuitive (and the results indicate) that improved frequency stability leads to a more stable design. Nevertheless, we find it enlightening to demonstrate how remote buffer depths are affected in the case of a 5% (0.5%) clock deviation. When a tile is created with 5% (0.5%) frequency deviation each node within the tile is created by randomly sampling from a gaussian distribution with a mean of 30MHz and a standard deviation of 5% (0.5%). Since many ( $\approx 10^4$ ) events are

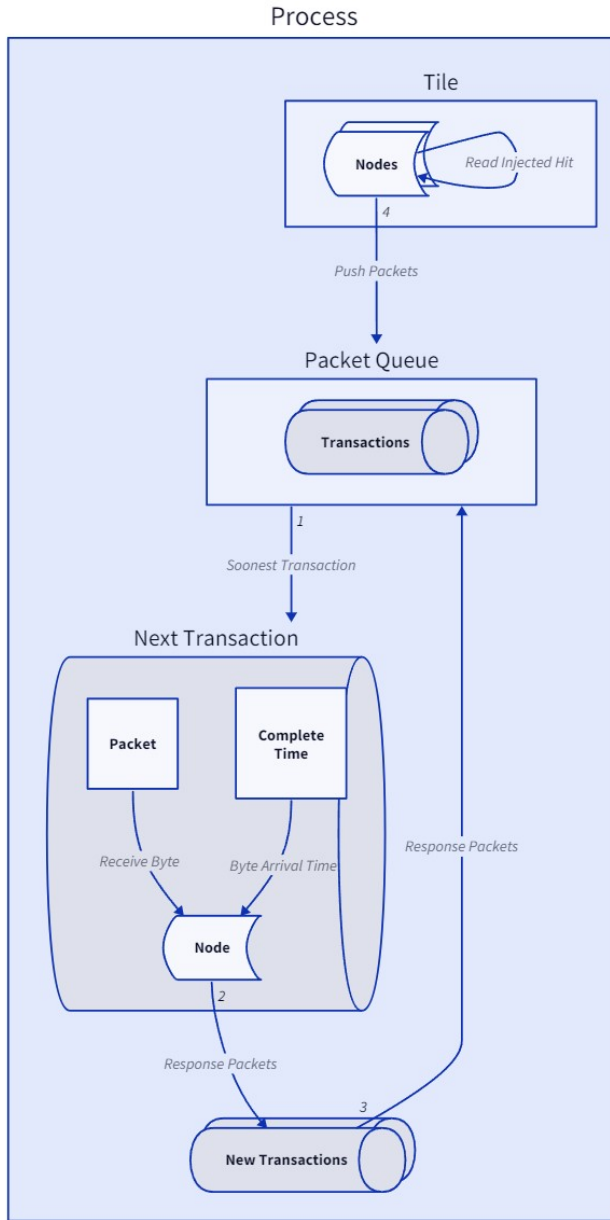


Figure 5.3: Flow chart of the simulation process method which occurs for every simulation time step. The simulation contains a queue of packet transactions. The queue is sorted by ascending time, so that the earliest transaction completed time is processed first. Each transaction contains a packet, a node, and the time the packet arrives. When the node receives the packet, it can optionally create more transactions, depending on the node's state and the packet. Any additional transactions are added to the simulation queue, and are time sorted. The simulation then increments the time for all other nodes within the tile. This procedure repeats until all nodes in the tile reach the designated time (11 seconds).

Parameter	Values Taken	Description
Oscillator Frequency	0.5%, 5%	High variance causes packet buildup or drift within the tile depending on whether packets are sent from slow to fast, or fast to slow clocks.
Tile Size	4×4, 8×8 10×14, 16×16	Affects total number of resets which must be routed to aggregator.
Routing	Snake, Left, and Trunk	Tiles with different routing are effectively different graphs which affect packet buildup (4.5). Different combinations of edges between nodes can cause packet buildup if nodes have more input edges than output edges.
Architecture	Push, Pull	Describes conditions for when node enters transmit-local state. 4.1. The push architecture allows individual nodes to transmit data when data are received, whereas pull architecture only send data upon receiving a special request packet from the aggregator.

Table 5.1: The different tile parameters that are used for the effective tile search. The frequency drift relates the relative distribution of the frequency of adjacent oscillators. The tile size determines how many digital nodes are within a single tile. The routing configurations are described in detail in the previous chapter, and refer to how local data words are sent to the aggregator. The two different architectures define how the node enters the transmit local state. The push architecture enters whenever a new reset is acquired, whereas the pull architecture enters only when a data request is received from the aggregator.

performed per tile configuration each tile is created with a random seed to ensure that each node is created with the same frequency for each test.

The other design parameters are readily configurable in either hardware (tile size) or through register configurations of the digital node (routing and, possibly, architecture). Tile size is mostly an engineering and cost constraint. Larger tile sizes mean the full design would require less aggregator nodes and require less tiles to parameterize. We show results for small tile sizes to indicate possible connections portions of larger tiles could configure. The largest tile size we tested was  $16 \times 16$  as the current limit in the Q-Pix digital prototype only allocates four bits for each x or y coordinate in a tile.

The routing and architecture parameters help guide the digital design efforts design of the digital ASIC. In practice it is all but certain that implemented routing for a digital tile will take on a

combination of the routing styles described here. The reason for this is simply that is likely that some digital nodes will fail (for whatever reason) in the life time of a DUNE-FD 10 kT module. Therefore, future tiles that contain hybrid routing we suggest to those users to individually analyze the sub tiles with appropriating routing and frequency distribution and determine if the buffer depths are appropriate.

### Oscillator Frequency and Drift

Two different oscillator frequencies are tested, as shown in Table 5.2. These different frequency variances indicate mean differences in oscillator frequency between adjacent nodes. An example of the 5% oscillator variance is shown in Figure 5.2. The values plotted in this figure indicate relative factors above or below the expected 30MHz mean.

Local oscillator drift was not included as a testing parameter since transactions occur over small time scales compared to any likely meaningful oscillator drift. If these drifts occur on time scales much longer than the interrogation time than the oscillator, the frequency could be continually re-calculated with the method shown in the previous chapter. If these drifts are periodic about a mean frequency and on time scales much smaller than the interrogation time window then the drifts would average out. In the event that clock drift timescales are on the interrogation timescale ( $\approx 1\text{s}$ ), then this is equivalent to a frequency uncertainty for the entire transaction cycle. This would mean that an oscillator has a  $\approx 5\%$  uncertainty in its frequency on each interrogation. Such a node would not be able to reconstruct timestamps, and therefore not be able to reconstruct the z-position of charge with the required 1ppm estimated uncertainty for Q-Pix clocks [6].

### 5.3 Simulating The Tile Readout

The tile simulation is performed by injecting hits from two known sources: radiogenic backgrounds and beam neutrinos. All results presented in this chapter are based on 11 seconds of simulated run time. Radiogenic data are collected and used to occupy 10 seconds of background noise resets. The higher intensity neutrino events are offset so that interaction occurs at  $t = 5.1\text{s}$ . The simulation is run for a total of 11 seconds, instead of 10, to ensure that all of the packets are collected by the aggregator node. In practice, there would be additional resets from backgrounds which occur in that final second of data. However, the number of resets from the radiogenic events are much smaller (by about two orders of magnitude) than the neutrino events.

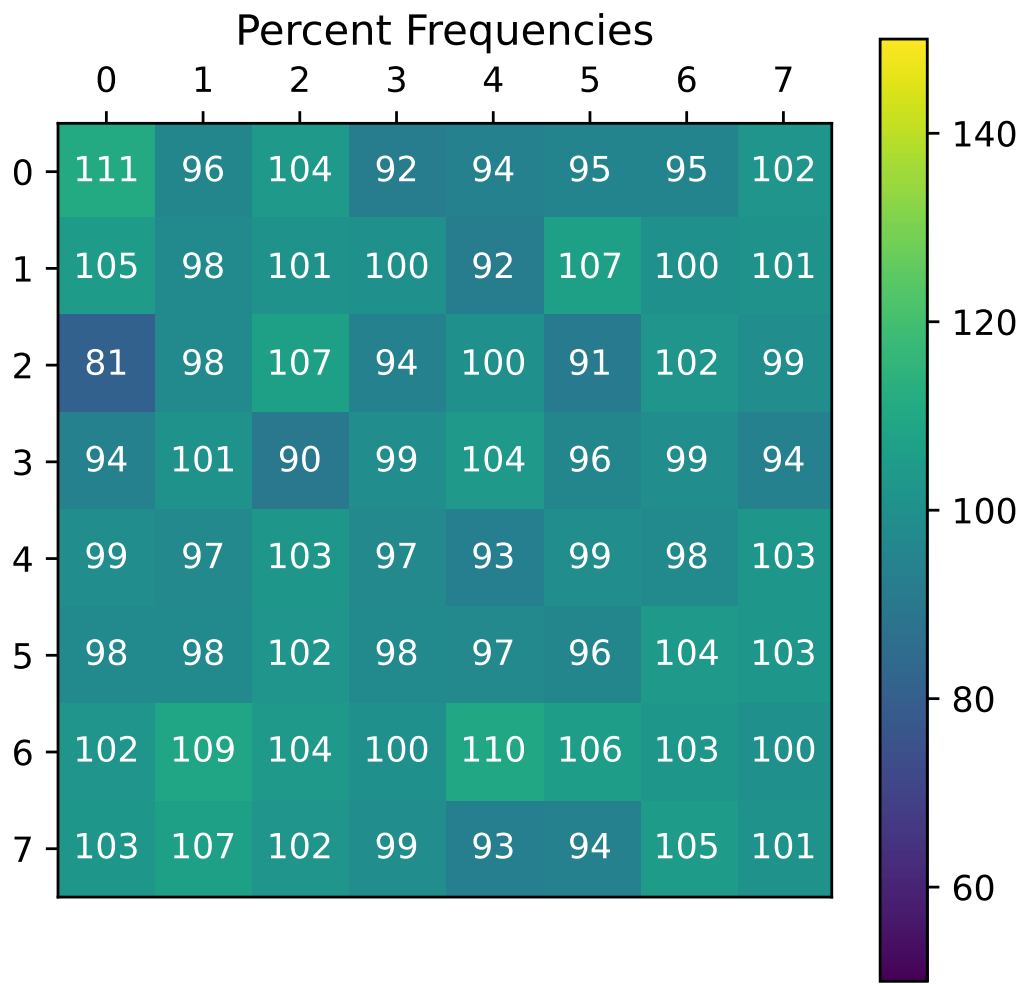


Figure 5.4: Distribution of ASIC frequencies used in the  $8 \times 8$  tile, and in the example FIFO buffer depths for this chapter. The numbers plotted above each ASIC row and column indicate the relative frequency of this ASIC compared to the nominal 30MHz mean. For example, a number of 112 indicates an ASIC which is 12% faster than 30MHz, a frequency of  $\approx 33.6\text{MHz}$ .

The full readout of the tile occurs based on the number of packets times the average transaction length.

$$T_{readout} \approx 50\mu s \times N_{maxpackets}$$

If we set  $T_{readout}$  to 1 second:

$$N_{maxpackets} \approx 20000$$

Since the simulation is run six seconds longer than the origin time of the neutrino events all reset events are accounted for if neutrino events cause less than  $\approx 120000$  resets. There are no simulated neutrino events which create these number of resets since this would require an energy of  $\approx 15\text{GeV}$  deposited into the LAr.

The configuration of each node and the tile happens before the beginning of the simulation. The frequency and the routing directions are configured for each node during its creation.

### **Simulation Timing**

The purpose of the simulation is to examine the communication behavior of digital nodes at different frequencies which communicate via packets of variable time width. For this reason special care is taken to ensure that the timing of packet transactions in the simulation are accurate. The behavior of each node is determined by its state machine properties, as described in Fig. 4.2. Therefore, an accurate measure of timing for each node is equivalent to ensuring that timing of ASIC state transitions are accurate.

Not shown are times when an ASIC receives or responds to a broadcast. Broadcast packets are uniquely handled by ASICs. An ASIC, instead of writing the request to the remote FIFO, immediately handles a broadcast by sending this packet to all neighbor ASICs, excluding the direction from which it received the broadcast. This means that an ASIC's state does not change during a broadcast. This is handled by the simulation by tracking packet times on the ASIC connections. The broadcast packet is sent starting at the soonest available time on each connection. The full broadcast procedure is described in Section 4.5.

### **Snake Timing Example**

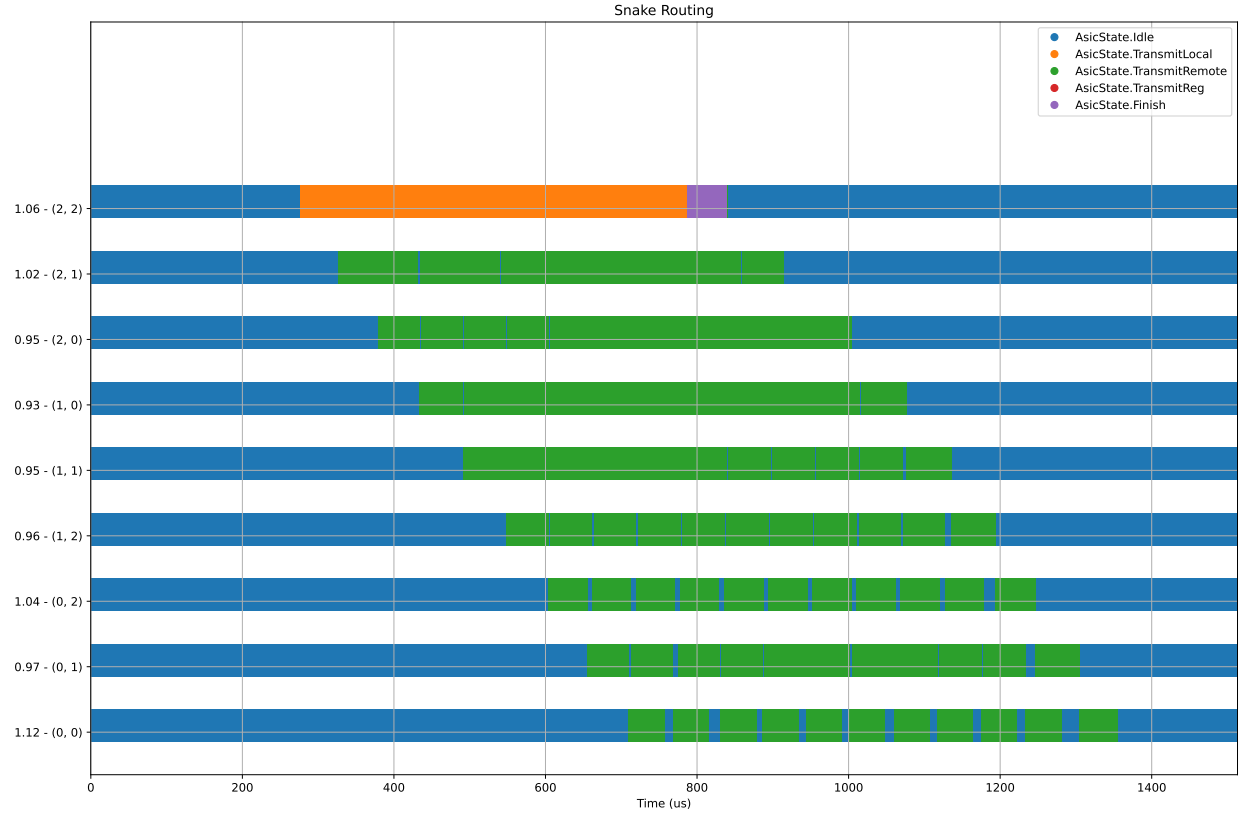
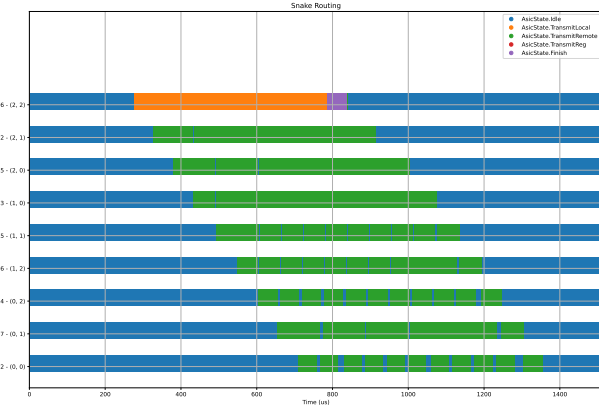
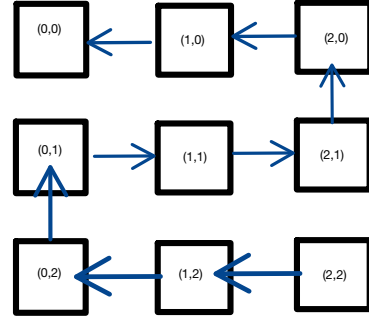


Figure 5.5: Example of timing ASIC state transitions in the simulation framework. The x-axis represents time in  $\mu s$ , and the different y-axis labels represent different ASICs within a  $3 \times 3$  tile shown. The y-axis also indicates the relative frequencies of the ASICs in the tile, where the node at (0,0) has the fastest frequency, which is 12% faster than 30 MHz. The blue regions indicate that the ASIC is in the idle state. The first orange state indicates that this ASIC (2,2) received a register request from the aggregator node and is now sending its local data, concluding in the purple state, which is sending the event end word. The Packets drift apart in time as they are sent from slower to faster ASICs. Shown here is the possibility of packet drift due to asynchronous packet transfers that depends on the magnitude of the frequency drift between neighbor ASICs.



((a)) Snake Readout timing Diagram



((b)) Data Path in Snake Readout

Figure 5.6: A snake packet transaction example is shown. The broadcast is received by the further node (2,2) and 10 data words are sent, followed by a event end word. Each packet tranverses through all nodes in the tile where remote packets are sent immediately.

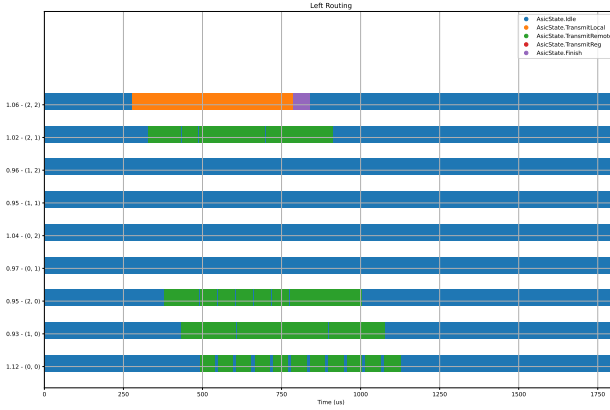
Here we refer to the "snake" routing as the maximmal path routing. This routing is one that minimizes the number of input edges for all nodes within a tile. An example of a packet transfer which uses this routing is shown in Figure 5.3.

Since the snake routing minimizes the number of edges, it also maximizes the number of ASICs responsible for sending remote data in the tile. This increases the number of remote transactions in a tile readout. This demonstrated by the amount of time ASICs are in the transmit remote state shown in Figure 5.3.

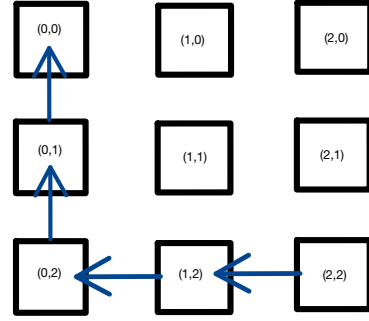
### Left Timing Example

The naming convention for the "left" routing is arbitrary since the tile can be viewed from the opposite direction and the routing would appear "right". By "left" routing we mean a routing configuration in which the routed direction for all ASICs in all rows are in the same direction, except for the nodes which have no neighbor in that direction. These nodes then are routed "up" towards the aggregator. An example of a packet transfer with this routing configuration is shown in Figure 5.7.

This routing configuration minimizes the path length for all nodes in the tile when the base-node is at the corner.



((a)) Left Readout timing Diagram



((b)) Data Path in Left Readout

Figure 5.7: A left packet transaction example is shown. The packet transfers begin with the furthest node (2,2) receives a broadcast from the aggregator. The data are then sent to the "left" and then "up" towards the base node, and finally to the aggregator node.

### Trunk Timing Example

The final routing scheme we simulate we call the "trunk" routing. We name this routing the "trunk" because all data are sent to a central column within the tile and then up towards the edge base node. An example of a simple data transfer is shown in Figure 5.8.

For tiles of widths larger than three there are multiple choices for which column will be the trunk. In for example, a 4×4 tile can have either the second or third columns be the trunk. In all even width cases we test, we choose the smaller row value for simplicity. In the 4×4 case we choose the second column and in the 8×8 case, we choose the fourth (3,0) column insted of the fifth (4,0).

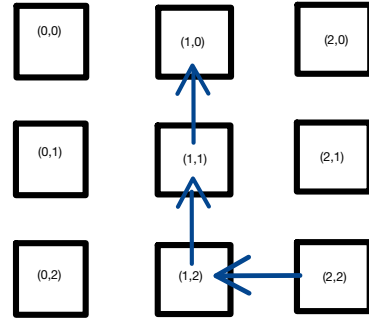
### The Pull Architecture and FIFO Depths

The "pull" architecture describes a tile configuration where data are only sent by ASICs within the tile when they receive a broadcast packet. We describe an example simulation event in this section with the pull architecture and the three routing methods to demonstate which variables are recorded. The example presented in Figure 5.3 stores resets accumulated over ten seconds from both radiogenic backgrounds and a 3GeV  $\nu_e$  event. The data shown are the total local FIFO transactions (writes) that occurred in the ten second run.

The figures shown in figs. 5.10 to 5.12 demonstrate how the data are accumulated onto the remote FIFO depths for the snake, left, and trunk routings respectivey.



((a)) Trunk Readout timing Diagram



((b)) Data Path in Trunk Readout

Figure 5.8: A trunk packet transaction example of two data words and a single event end word is shown. This routing method allows for the fastest possible transaction time since it minimizes the edge lengths between the base node and all other nodes within the tile. In this  $3 \times 3$  example shown, the base node is at (1,0), or in the middle.

Routing	Local Max	Remote Maximum	Ratio of Remote:Local
Snake	153	208	1.36
Left	153	312	2.04
Trunk	153	306	2.00

Table 5.2: Example results obtained from the three simulation examples for the pull architectures shown in the previous figures. The value of interest in determining the required remote FIFO depths for each ASIC is the maximum depth that occurred on any node. A memory optimized routing configuration is one that would introduce the least strain on the remote buffer depths for a given local buffer depth input.

The following figures demonstrate why it is important to design all ASICs within a tile to meet the same specifications. Future Q-Pix ASICs within a tile will be exposed to events at or above these energy scales, and there is no guarantee (until the ASIC is in hand) what the frequency of its oscillator will be, or its location within a tile. In all three routing examples shown it was not the base node which experienced the most strain on its buffer depth, but the ASIC along the route path which had the lowest frequency.

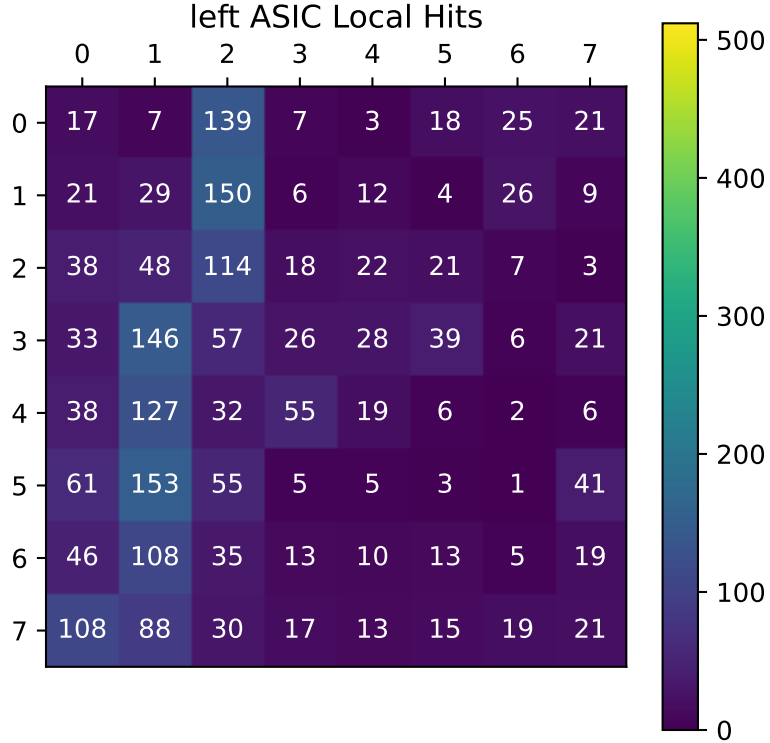


Figure 5.9: Example local FIFO distribution of a  $\approx 3\text{GeV}$   $\nu_e$  event. The numbers over each tile represent the total number of writes which occurred to each local FIFO in the array. Even with the lowered resolution (each ASIC accounts for 16 pixels), different tracks are noticeable based on the FIFO depths. The maximum scale for the heatmap is chosen to be 512 resets.

### The Push Architecture

The final simulated parameter to describe is the push architecture. Since the push architecture allows individual nodes to determine when packets can be sent all nodes must be inspected at each time step to check if a reset occurs before this new time window. If a reset occurs at a time before the next simulation timestep, then the reset is removed from this node's hit list and is written to the node's local FIFO. The node will then see at this simulation timestep that the local FIFO is not empty, and leave its idle state to send this packet. An example of this process is shown in figure 5.3.

Every simulated time step is shown and recorded along the x-axis. The distance in time between simulation steps increases during packet transfers since the nodes state is fully determined during

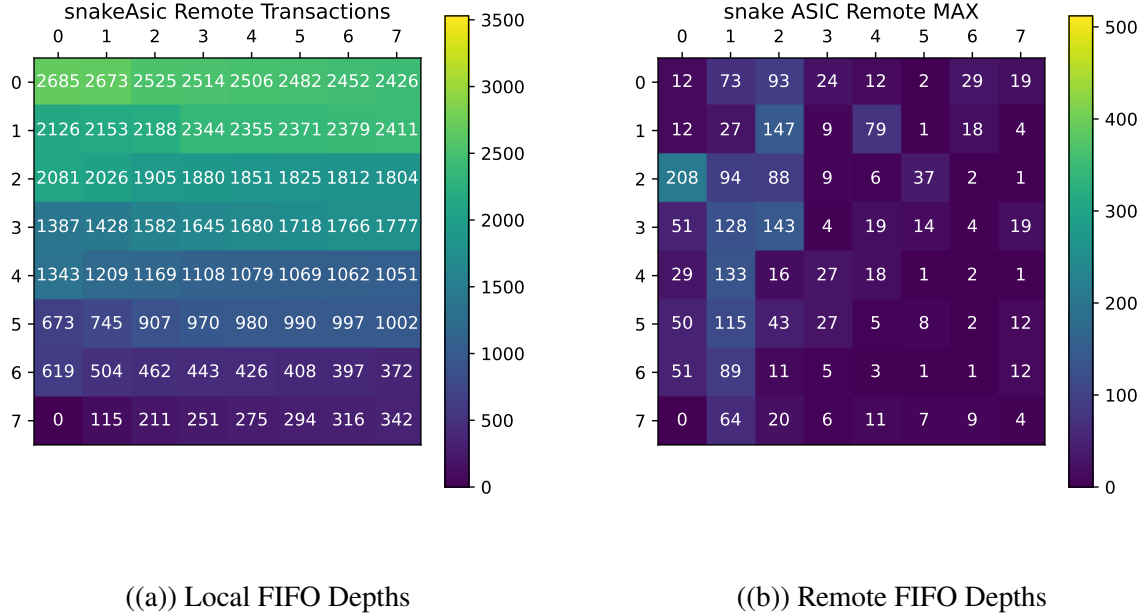


Figure 5.10: Example of local (a) and Remote (b) fifo depths of the example neutrino event from 5.3 after processing. The colorbar to highlight the maximum number of transactions is used to indicate remote transactions which were happening for 2% of the total readout time of 10 seconds. The node which has the largest remote buffer depth corresponds to the ASIC with the slowest frequency as shown in Figure 5.2. The reason for this excess of buffer depth is due to packet buildup on the slow ASIC.

this time. This simplification is performed to speed up simulation run time.

## 5.4 Physical Simulation Studies

We now discuss the methodologies of the physical simulations used as input to the digital tile simulation described in the previous section.

## Radiogenic Backgrounds as a Calibration Source

In this section we comment on the ability to the auto-calibration of the reset loss per charge. The full charge calibration procedure is beyond the scope of the work presented here, due to intricacies that depend on the final implementation of the reset circuit as well as the replenishment circuit of the final Q-Pix ASIC. This analog front-end ASIC currently exists and these features are currently

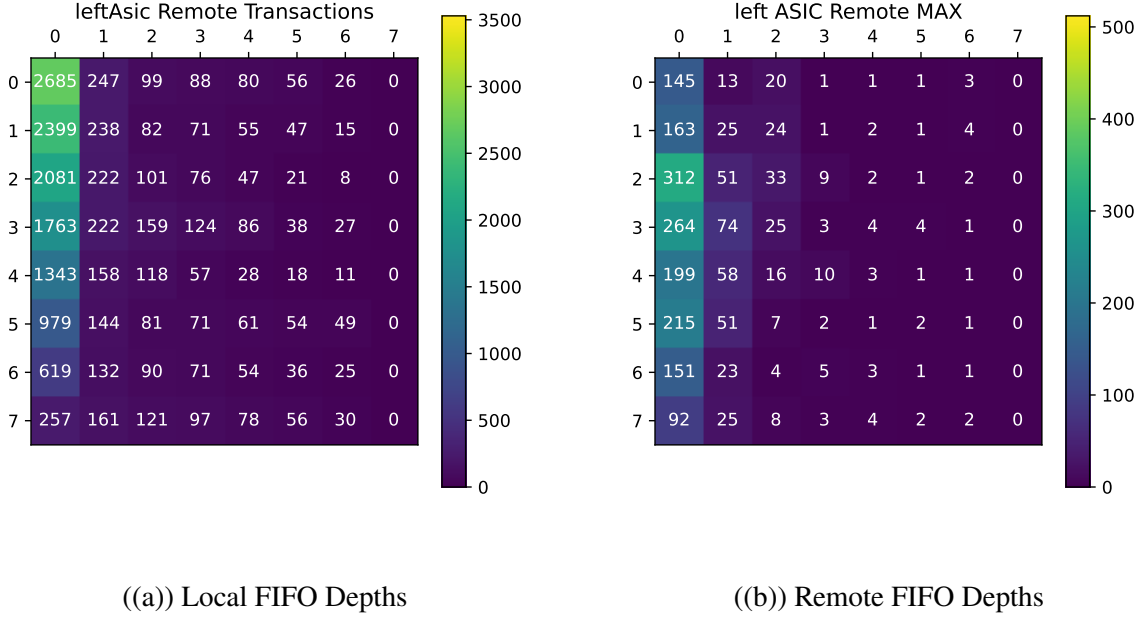


Figure 5.11: Example of local (a) and Remote (b) fifo depths of the example neutrino event from 5.3 after processing. The ASIC which has the largest remote buffer depth also corresponds to the ASIC with the lowest frequency as shown in Figure 5.2.

being explored. Nevertheless, we describe the relevant portions to the problem here since the charge calibration along with the frequency calibration and timestamp measurements determine Q-Pix's z-position reconstruction.

The main idea behind the auto-calibration of charge at the pixel level relies on using the known (and near constant) input current from the radiogenic backgrounds (mostly  $^{39}\text{Ar}$ ) in the detector. If a perfectly known and constant input current ( $I_o$ ) source was input to a pixel it would produce resets separated by a constant time ( $\tau_{rtd}$ ). It would be a straight forward matter to calculate the charge per reset:  $Q_o = I_o * \tau_{rtd}$ .

Then, to analyze the ability for an auto-calibration procedure for Q-Pix it is important to analyze and understand the long-running charge accumulation (resets) from backgrounds present in the LAr. We use the following list of radiogenic sources of 10 distinct runs of 1000 seconds each. Further details on radiogenic backgrounds in LAr can be found at [7, 84, 85]

The well-known C++ based Geant4 [80] simulation toolkit is used to simulate particle decay and ionizing particle interactions within the LAr volume. We use the energy deposited along the track

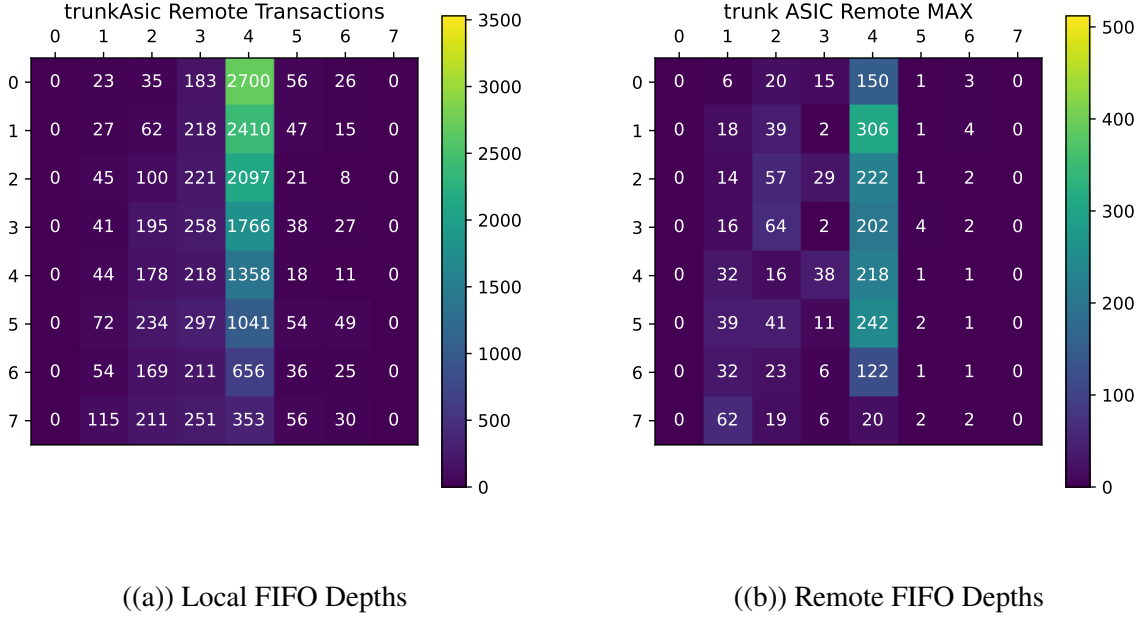


Figure 5.12: Example of local (a) and Remote (b) fifo depths of the example neutrino event from [5.3](#) after processing. The ASIC which has the largest packet buildup occurs at (4,1). This ASIC also corresponds to the ASIC which has the lowest frequency along the trunk column as shown in [Figure 5.2](#).

from each ionizing particle with the W-value for liquid argon (23.6 eV) to determine the number of electrons deposited in the LAr. The resulting number of electrons are then uniformly deposited over the individual track. Then we calculate the probability of recombination for each electron following the "modified box" model [\[86\]](#).

The time and location of drift for each electron is calculated with an applied transverse and longitudinal diffusion with values taken from [Table 1.3](#). The simulations for all particle interactions are run individually with a uniform random sampling of the initial decay time interval within the 1000 second window. All of the hits are then sorted by increasing time, so that the first hits read are the hits which occur the earliest. Sorting the hits by time before accumulating charge ensures that the resets are recorded at the correct time.

This simulation produces  $\mathcal{O}(10^{11})$  hit interactions which produce  $\mathcal{O}(10^{14})$  electrons, which in turn produces  $\mathcal{O}(10^9)$  resets. To reduce the memory utilization of the simulation the electrons are accumulated on a hit-by-hit bases and are subdivided into a pre-determined  $4 \times 4$  cross-sectional area of the detector. Each cross-sectional area defines a pixel. The dimension of the LArTPC

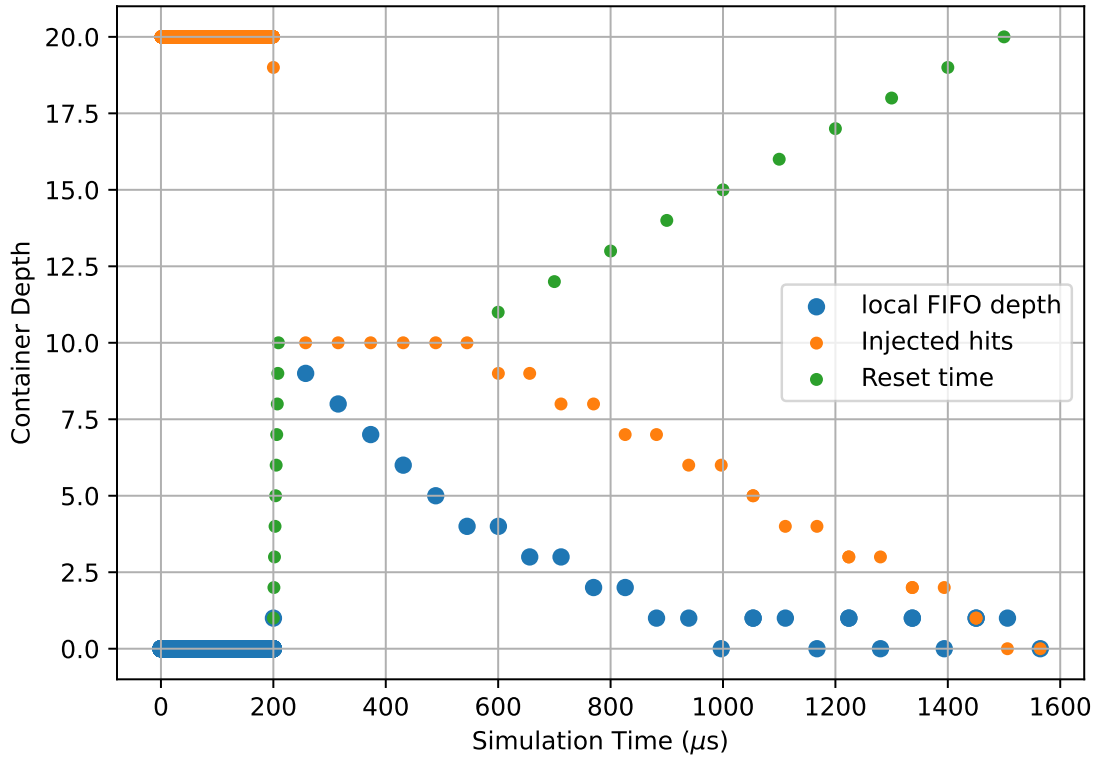


Figure 5.13: A simulated push architecture with 20 injected hits at different times. The time of the injected reset is indicated by the green points. Before the simulation is run a node has its hits injected into a storage (orange) list. Then, at each simulation time step ( $\tau_{step} = 1\mu s$ ) the list is examined to see if a new hit will be written. When a hit is found the relative time of the node can move forward in time to when this packet will be completed in time, while all other writes can occur to the local FIFO. This is why the first local FIFO depth increases initially by one despite 10 nearly adjacent injected hits. On the next time step, the depth then moves to nine; the simulation has sent the first of the 10 packets, and records nine. This example correctly shows a maximum local FIFO depth of nine.

Isotope	Rate [Bq/kg]	Region	Region Mass [kg]	Rate [Bq]	Number of Decays (per 10 s window)
$^{210}\text{Po}$	0.2	PD [Bq/m <sup>2</sup> ]	2.46856	0.493712	5
$^{60}\text{Co}$	0.0455	CPA	90	4.095	41
$^{40}\text{K}$	0.49	APA	258	1,264.2	12,642
$^{39}\text{Ar}$	1.010	bulk LAr	70,000	70,700	707,000
$^{42}\text{Ar}$	0.000092	bulk LAr	70,000	6.44	64
$^{42}\text{K}$	0.000092	bulk LAr	70,000	6.44	64
$^{222}\text{Rn}$	0.04	bulk LAr	70,000	2800	28,000
$^{214}\text{Pb}$	0.01	bulk LAr	70,000	700	7,000
$^{214}\text{Bi}$	0.01	bulk LAr	70,000	700	7,000
$^{85}\text{Kr}$	0.115	bulk LAr	70,000	8050	80,500

Table 5.3: The radiogenic background distribution is the same as that found in previous work [9]. For each 1000 second analysis the pre-rounded values are scaled up by a factor of 100 to achieve the correct normalization of events for each isotope. A key difference between the backgrounds is the origin or source of each background. Of special note is  $^{40}\text{K}$  whose source location is the APA beams, and whose resets can be distinctly seen in Figure 5.4 as the slightly more active (yellow) region of the APA. Due to this source alone, it is likely that precise auto-calibration for charges will likely have to account for the pixel location within the APA.

volume is  $2.3 \text{ m} \times 6.0 \text{ m}$  which divides into 575 pixels in the x-direction and 1500 pixels in the y-direction. There are then a total of 862,500 pixels, which store location and reset information.

As an example, the total resets from 1000 seconds of the simulation are shown in Figure 5.4. The most active pixel receives  $\approx 220$  resets during this simulation time. The bins for the histogram are at the pixel level and represent the  $4 \times 4 \text{ mm}^2$  of each pixel.

Additional information is tracked for each reset to identify the contribution of each radiogenic background for each reset. A reset occurs when 6250  $e^-$  have accumulated on a pixel. The time recorded for the reset is the same as the time the simulation calculates the last of the required 6250 electrons to arrive at the designated pixel region. This optimization was added to the existing simulation framework to separate the unknown analog contribution to the timing uncertainty from the physical simulation.

In practice the analog front-end reset circuit obviously takes time to respond to added charge and to issue a replenishment and reset commands. There will always be some delay between the final electron's arrival, the time of the analog reset, the replenishment circuit, and the time recorded on the digital back-end. However, for the purposes of this analysis, we assume that this reset

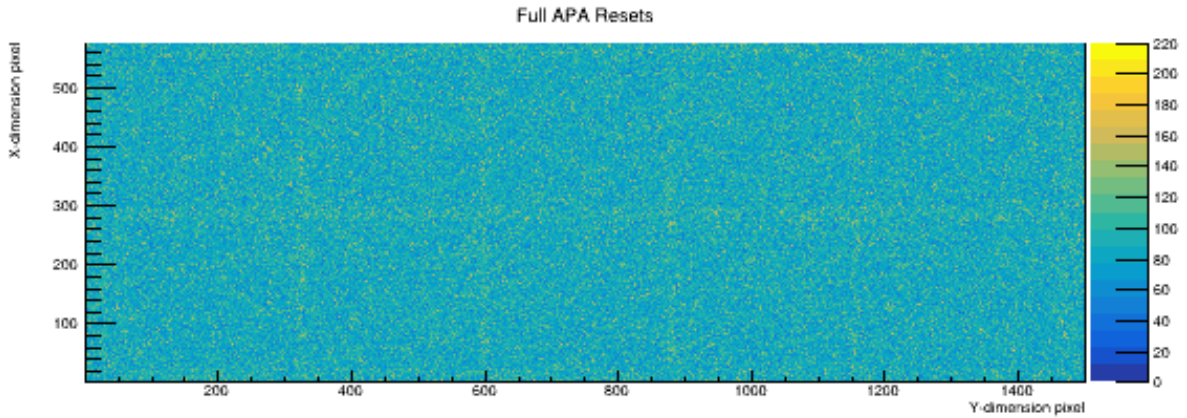


Figure 5.14: Full 1000 second of radiogenic background source simulation input into all pixels within the APA. A close examination of the resets can reveal the additional resets from the backgrounds which are location dependent. The majority of the uneven distribution of resets occur at the location of the APA bars due to the  $^{40}\text{K}$  isotope.

and replenishment circuit activity can happen more quickly than the average local oscillator of the digital back-end. Therefore this analysis assumes the best timing measurement based on the digital back-end. The time measurement is then limited only by the clock frequency of each local oscillator. Finally, we comment that this optimization of the timing of the analog front-end affects only the time values, and by extension, the reconstruction of the particle tracks. It does not affect the total amount of charge, and therefore the total number of resets recorded by each pixel.

Any combination of the backgrounds can contribute some or all of the electrons required to produce a reset. The contribution of the total electrons for each of the radiogenic sources are shown in Figure 5.18. We refer to the contribution of the number of the electrons to the reset as the "weight" of the reset.

The ability to perform a charge auto-calibration using radiogenic events depends on the background to provide a reliable average input current source. We use only the data presented in Figure 5.4 and calculate the mean time between resets for all pixels. For this simple calculation, we simply take the total number of pixels (4096) and divide by the total number of recorded resets (411152) and obtain an average RTD of 9.96 seconds.

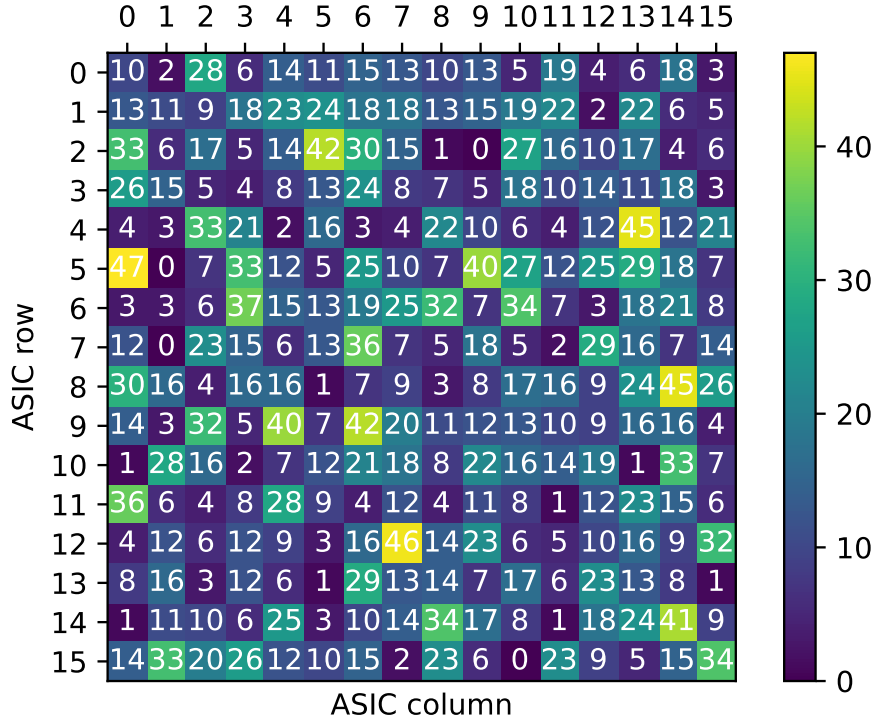


Figure 5.15: Baseline noise input for the digital simulation from all radiogenic sources and background leakage current. This figure shows the total resets in the 10 second window for the  $16 \times 16$  tile. The other tile size configurations ( $4 \times 4$ ,  $8 \times 8$ ,  $10 \times 14$ ) also use these reset data for background noise. All tiles start with the top left node as their origin node.

A very rough expectation of background current is  $I_o \approx 100$  aA. We can then use the following equation to calculate:

$$I_o = \frac{Q_o}{\tau_{rtd}}$$

solving for  $Q_o$  with  $\tau_{rtd} = 9.96$  and  $I_o \approx 100$  aA, we obtain:

$$Q_o \approx 100 * 10^{-18} * 9.96 / 1.6 * 10^{-19} \approx 6225$$

Calibration results from the first analog prototype and a more sophisticated analysis will be needed for pixel level charge calibration. The contrived derivation above assumes equal capacitance and charge replenishment on all pixels, which in practice is not necessarily true. Additional tests can likely be done for each pixel by comparing the peak of the distributions as shown in Figure 5.4.

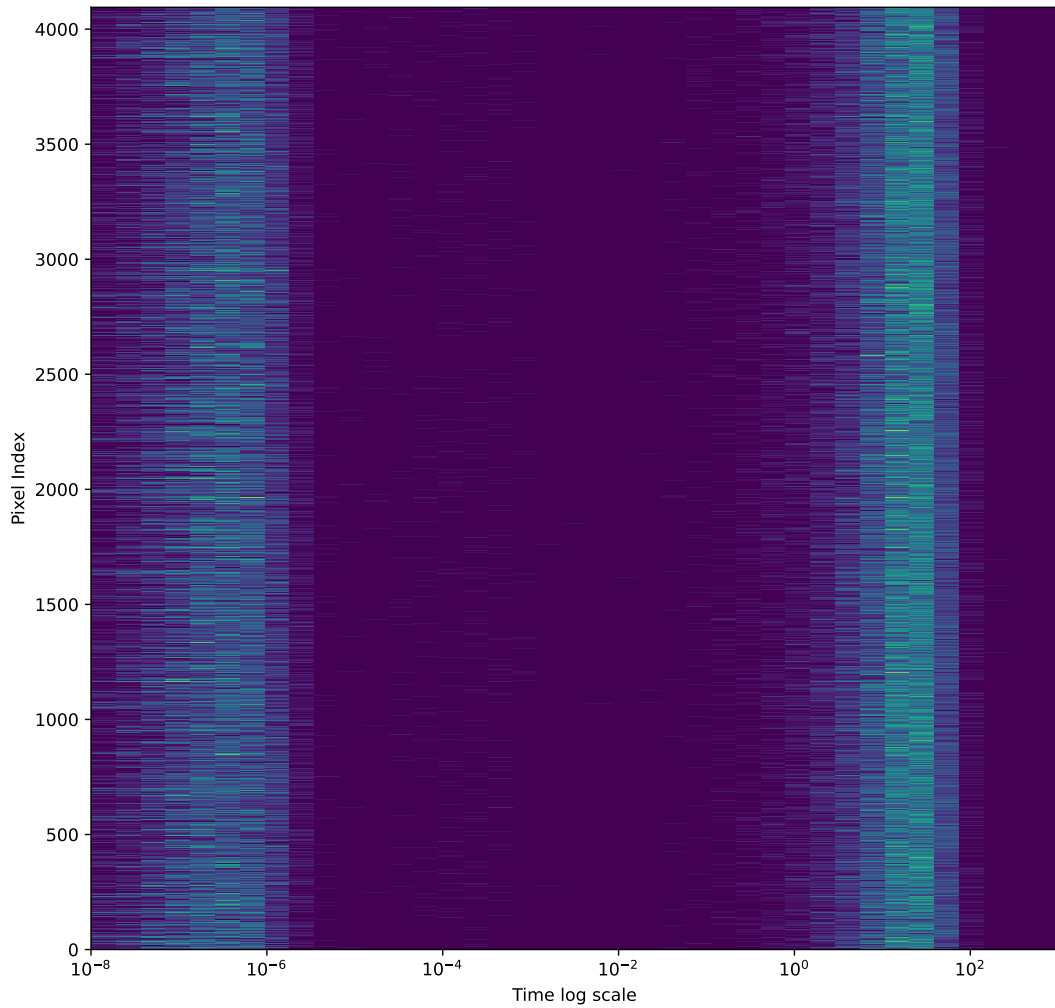


Figure 5.16: All 4096 pixels in the  $16 \times 16$  tile for 1000 seconds of radiogenic data. The y-axis represents a different pixel, and the x-axis is a log-scale time axis with even bin widths. There are two clusters of resets for different time intervals. The first large cluster of resets occurs at  $\approx 10^{-7}$  seconds and is due to a single radiogenic decay event causing additional resets. The second large cluster of resets occurs at  $\approx 10$  seconds. This second cluster of resets is caused from the first reset of a new radiogenic decay event. The ability to perform a charge calibration per pixel may depend on accurately resolving the mean for this "long period" RTD.

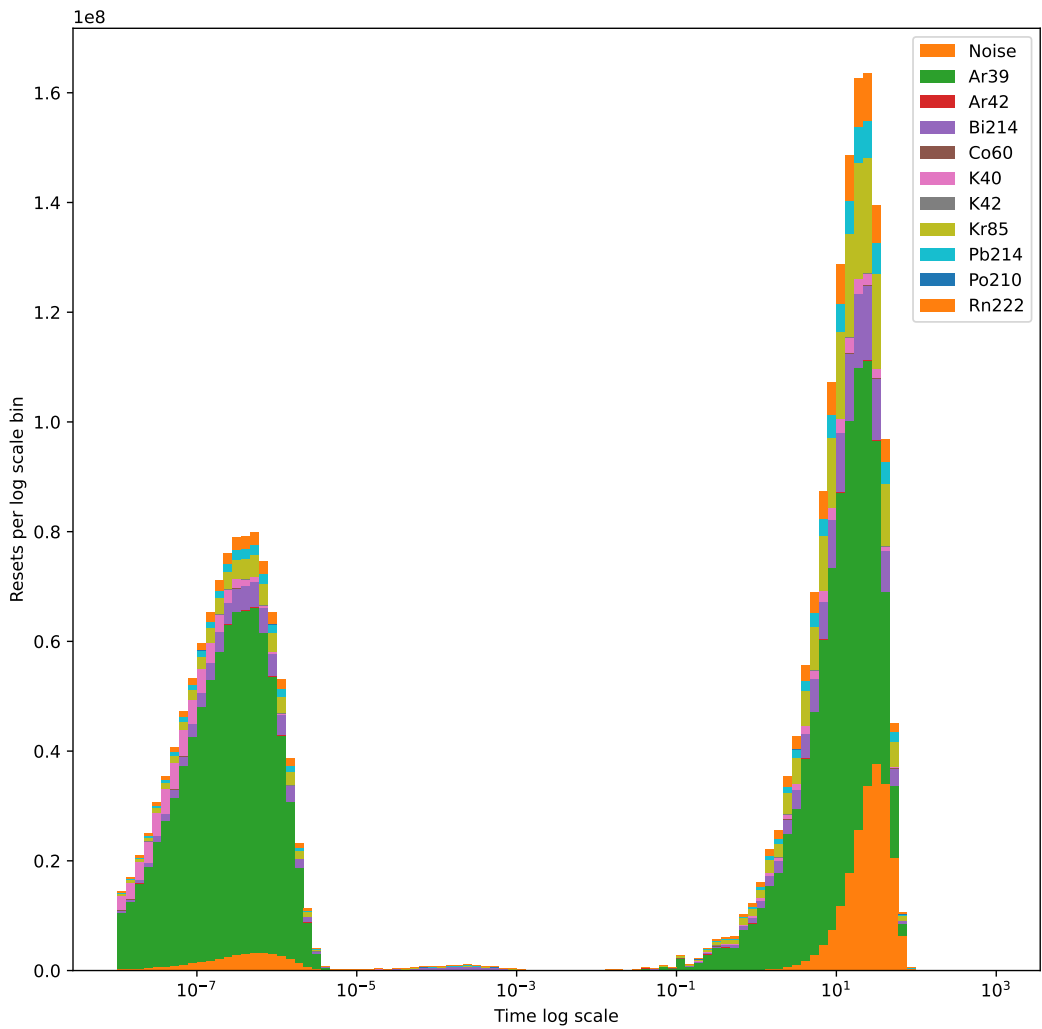
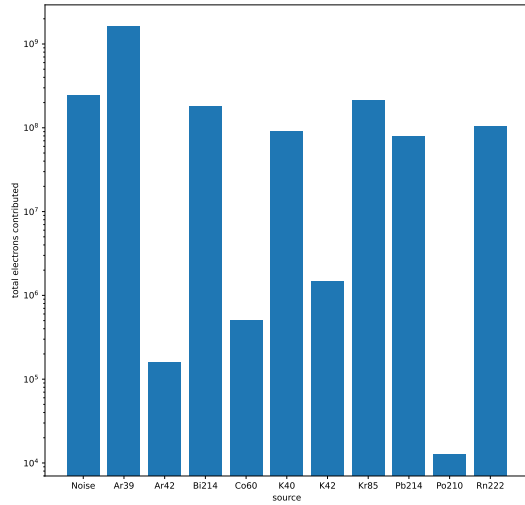
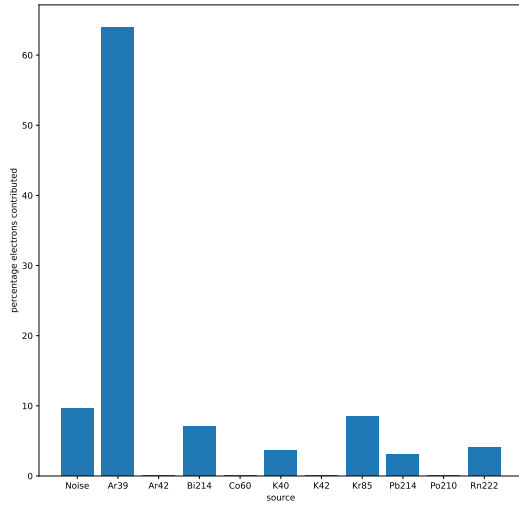


Figure 5.17: All 4096 pixels in the  $16 \times 16$  array for 1000 seconds of radiogenic data. These data are the same as those shown in Figure 5.4, where all pixel RTDs are binned together. There are two clusters of resets on two different time scales. The first cluster of resets near at  $\tau_{rtd} \approx \mathcal{O}(10^{-7})$  is due to events which produce more than one reset. The second cluster of resets near at  $\tau_{rtd} \approx \mathcal{O}(10^1)$  are from a "waiting" period where there is no charge buildup from decays and only background noise. The dominant source of electrons on each pixel is from the  $^{39}\text{Ar}$ , with a non-zero contribution from leakage. The leakage current value used in this simulation is 10 aA.



((a)) Contribution of total electrons.



((b)) Contribution of electrons by percentage.

Figure 5.18: Both figures indicate a comparison of the amount of electrons deposited on all pixels in the tile shown in Figure 5.4. Plot (A) represents the total number of electrons on a log scale. As expected,  $^{39}\text{Ar}$  contributes the majority of background charge. The leakage current used is 10 aA, and represents about 10% of the total contribution of electrons. This implies that leakage currents from the front circuit which are  $\approx 100$  aA will contribute nearly as much electrons to the steady-state RTDs as the radiogenic backgrounds.

Such an analysis is not appropriate yet since it is not yet known what the leakage current will be in the Q-Pix ASIC. As shown in both Figure 5.4 and Figure 5.18, the contribution from noise is not negligible. Therefore, any true analysis of the charge auto-calibration ability of Q-Pix awaits studies of both the leakage current and replenishment circuits of the analog frontend.

### Reset Contribution of Radiogenic Sources and Leakage Current

Figure 5.18 compares the total (Plot-A) and percentage (Plot-B) electrons contributed from noise and radiogenic sources. These results highlight the importance of understanding and mitigating any leakage current for every pixel. A leakage current of 10 aA contributes  $\approx 10\%$  to the total background current. What may prove difficult in the auto-calibration procedure of the Q-Pix readout is that while the contribution from radiogenic sources shown in Figure 5.18 may be the same, the leakage contributions may not be.

## 5.5 Neutrino Interaction Studies

Here we discuss the implementation of the digital framework within the high energy regime. For this we use as an input neutrino events from the Long-Baseline Neutrino Facility (LBNF) [5] and take the unoscillated flux of neutrinos which were used in [11]. These neutrino flux are simulated using GENIE [16], v2.12.10. The interaction distributions for both the forward and reverse horn current directions are shown in Figure 5.5.

We do not perform any calculation involving the oscillation on the input neutrino flux. The reason for this is that the digital back-end should be able to fully record data from all possible  $\nu_l$  events regardless of interaction type, not only the intended  $\nu_e$  appearance spectra. It is equally important for a future readout to be able to correctly tag noise ( $\nu_\mu$ , or  $\nu_e$  from the beam, etc.). For example, sensitivity to mass ordering and CP violation rely on the ability to measure  $\nu_\mu$  disappearance in addition to the  $\nu_e$  appearance.

What will be shown in the upcomming sections is that capability of the digital back-end depends on the energy deposited in the volume of the LAr. By the virtue that oscillations change only the flavor (not the energy) of the  $\nu$ , the constraints of the back-end do not depend on if more (or less)  $\nu_e$  are measured compared to  $\bar{\nu}_e$ , provided the back-end is capable of fully measuring both events. Furthermore, by using the unoscillated flux of the neutrinos at the near detector, the neutrinos will be of necessarily higher energy than the expected flux at the far detector. The use of high energy helps in establishing what we will show as the upper-bound for the required local and remote FIFO depths for each ASIC.

### Neutrino Event Parameters

Table 5.5 describes the parameters of each input for the simulation. The parameters used to vary the tiles for these neutrino input energies are shown on Table 5.2.

The Q-Pix readout presented here is designed for use in a LArTPC at the scale of DUNE-FD 10kT module 1.6. In order to test what kinds of requirements this readout will need we use high energy neutrino interactions as discussed in Section 5.5. The different selection parameters for each event are neutrino flavor, neutrino energy, horn current direction, Z-position vertex position, and source neutrino momentum direction ( $\theta_z$ ). We define the beam direction (the direction parallel to the

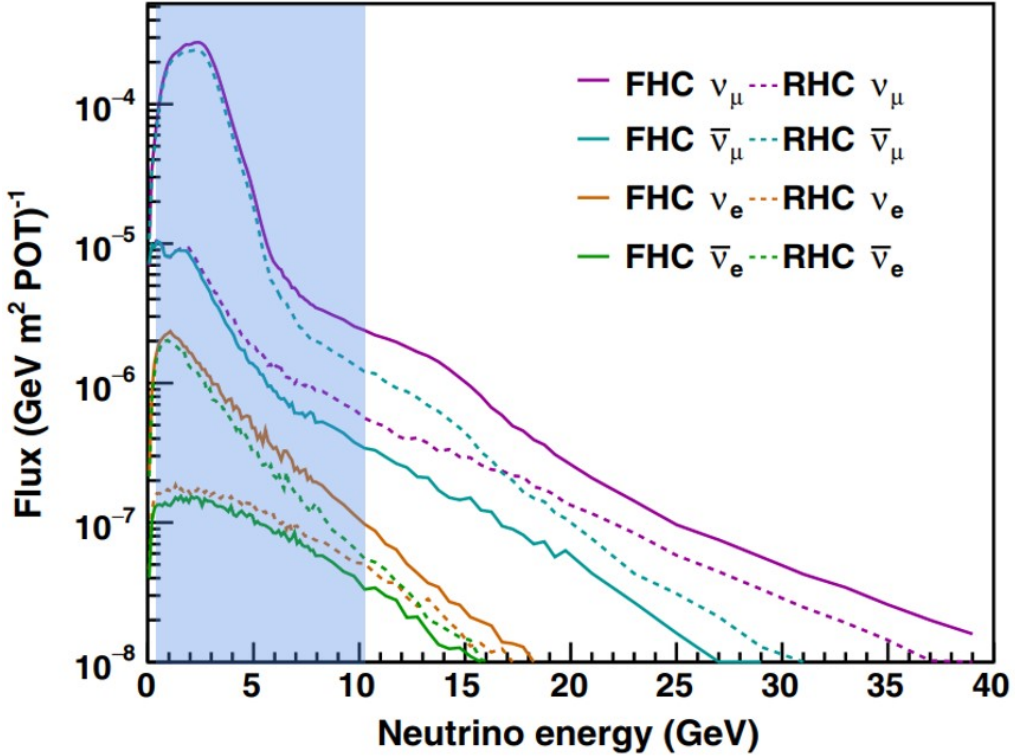


Figure 5.19: Flux spectrum of neutrinos from the neutrino beam used in this study. This figure is taken from [87]. Highlighted in blue is the reconstructed energy range of neutrinos that are used to seed the interaction with the APA LAr’s volume.

surface of the APA) as  $\theta_z = 0$ . The X and Y positions are held constant for all interactions, at X = 120 cm and Y = 3200 cm. The coordinate system we use, as well as a slice of the APA within a module are shown in Figure ??.

The LBNF beam is not the only source of high energy particles DUNE will detect. Other high energy ( $\simeq 10$  GeV) interactions may come from other sources. These other high energy events (such as nucleon decay, cosmic neutrinos) may also deposit energy on GeV scales per interaction. These sources may interact with their net momentum vector pointing in any direction. For this reason we also test  $\nu_e$  and  $\nu_\mu$  interactions at  $\theta_z \pm 90^\circ$ ; this direction causes the secondary ionizing particles to carry momentum along the direction parallel to the pixel’s surface normal. These two momentum directions, though unphysical for beam interactions, still present possible interactions

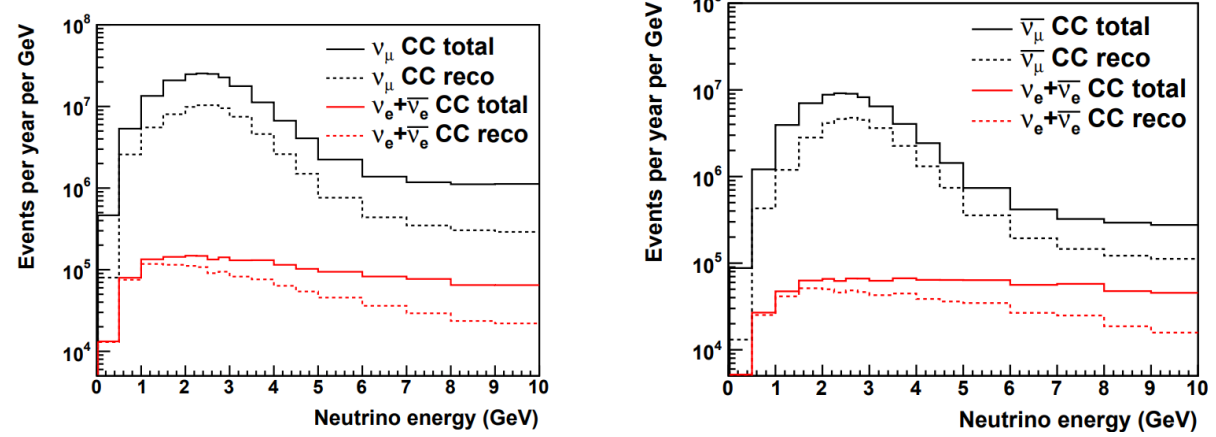


Figure 5.20: Rate of CC neutrino interactions based on flavor as a function of true neutrino energy. Figure is taken directly from [11]. Right is shown the neutrino interaction distribution for the forward horn current. The left image is for the reverse horn current. Both images assume an average exposure rate of 1.2 MW from LBNF beam.

types within the scope of DUNE’s proposed physics program [77].

## Neutrino Event Results

Every simulated neutrino interaction generates some number of resets which are collected onto the pixel plane. The purpose of the study explored by the parameters described in Table 5.5 is to investigate the charge resets these interactions produce; we pay particularly close attention to ASICs where the number of resets (energy deposited) is the largest in a given event.

We bin the maximum number of resets in a  $4 \times 4$  pixel array, or ASIC, for every neutrino event. The plot Figure 5.23-(A) shows a  $\nu_e$  event and Figure 5.5 shows these resets binned into pixels. For every event we take the maximum ASIC value and use that as an entry into a histogram. Next,

Name	Values	Relation
$\nu_l$	$\nu_e, \bar{\nu}_e, \nu_\mu, \bar{\nu}_\mu$	Oscillation measurements require sensitivity to measurements for both $\nu_e$ appearance, and $\nu_\mu$ disappearance.
$\nu_l$ Energy	0.25 GeV to 10 GeV, in steps of 0.25 GeV	neutrino energy determines output secondary energy, which causes more resets and directly affects buffer depths.
Horn Current	Forward and Reverse	Beam horn current direction affects neutrino flux, as shown in Figure 5.5. Additionally, mass hierarchy measurements (according to the MSW effect [72]) require difference in measurements of appearance probability for $\nu_e$ and $\bar{\nu}_e$ .
Z-position	10 cm, 80 cm, 180 cm, 280 cm, 350 cm	Interaction z-position above the anode plane. Interactions which happen further from the collection plane have more time to diffuse or recombine.
$\theta_z$	$0^\circ, \pm 2^\circ, \pm 90^\circ$	Different momentum angles are different Z-positions, in general, direct ionized particle tracks within the active volume.

Table 5.4: The different neutrino simulation parameters which are passed into Geant4 based simulation. The original interaction products are generated using GENIE [16] v2.12.10. The output products of the neutrino interaction produced from GENIE are then configured using the different parameters described above. We select  $\nu_l$  events for different energies in bin-widths of 250 MeV; We follow the same bin width as is done in [12] for their neutrino oscillation analysis. A selection of 100 events for each  $\nu_l$  is taken within each energy bin, for a total of 3900  $\nu_l$  events for each horn current direction, z-position, and  $\theta_z$  selection. Since there are two current directions, four  $\nu_l$ , five z-positions, and five  $\theta_z$  positions, a total of 780,000 neutrino events are simulated.

we take the integral of each histogram as shown in (B) of Figure 5.23 and (B) of Figure 5.24. The value of this integral gives the percentage of fully events a function of local FIFO depth.

## Neutrino Energy Deposit

The true neutrino interaction energy is notoriously difficult to reconstruct. The neutrino itself carries no charge and its track is not directly reconstructed in the LAr. Other effects such as long neutron drift make perfect energy reconstruction of the neutrino interaction impossible by principle. For these reasons we show how the resets and ASIC FIFO depths vary both by the energy deposited into the LAr as well as the true neutrino energy. Figure 5.25 shows the relationship between the

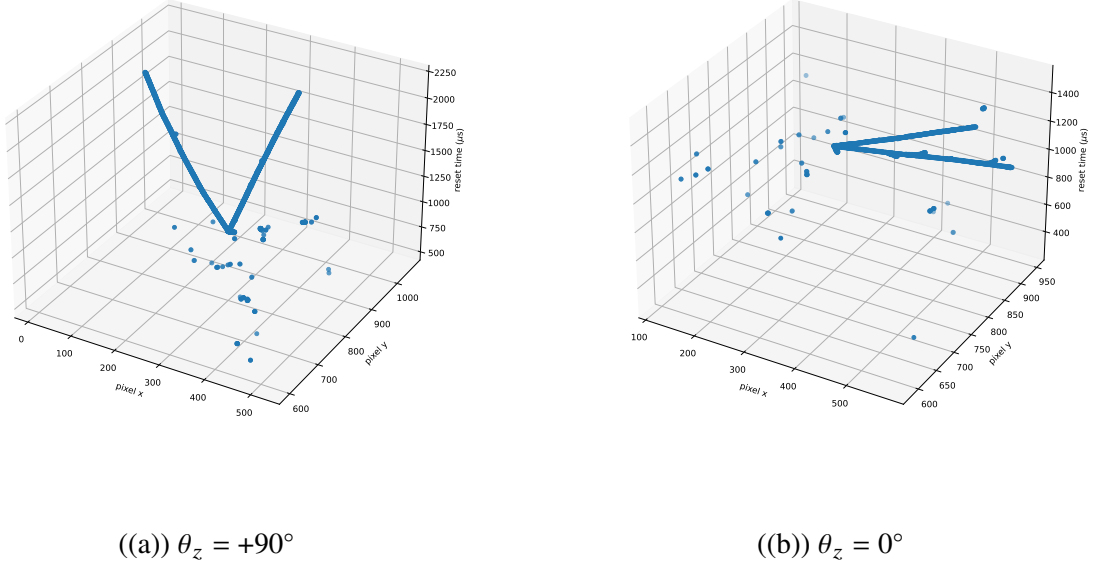


Figure 5.21: Same  $\nu_e$  interaction at Z-position = 180cm, which is in the middle of the drift length of the APA. Image (A) has the incident  $\nu_e$  momentum rotated upwards ( $\theta_z = +90^\circ$ ). Image (B) has the incident  $\nu_e$  had momentum along the beam direction ( $\theta_z = 0^\circ$ ). Since there are five different z-positions, and five different  $\theta_z$  values, each of the 3900  $\nu_l$  interactions are repeated 25 times. These two plots show two of those 25 examples.

true  $\nu_e$  energy and the max FIFO depth as well as the total APA resets. Figure 5.26 shows the same relationships instead as a function of the energy deposited.

One of the key differences of a Q-Pix readout compared to a traditional waveform readout is that the amount of data the Q-Pix readout collects depends on the energy deposited. Since Q-Pix is fundamentally a counting readout, the amount of counts (data) it collects depends on the amount of energy deposited. Therefore, one limit on its bandwidth is the total amount of resets it can measure, which is proportional to the energy deposited as shown in Figure 5.5.

## Local FIFO Depth Results

To predict the required local FIFO depth for the Q-pix ASIC, we perform the integral as shown in Figure 5.23 for each of the parameters described in Table 5.5. Since there are 200 different parameters, there are 200 different integral values.

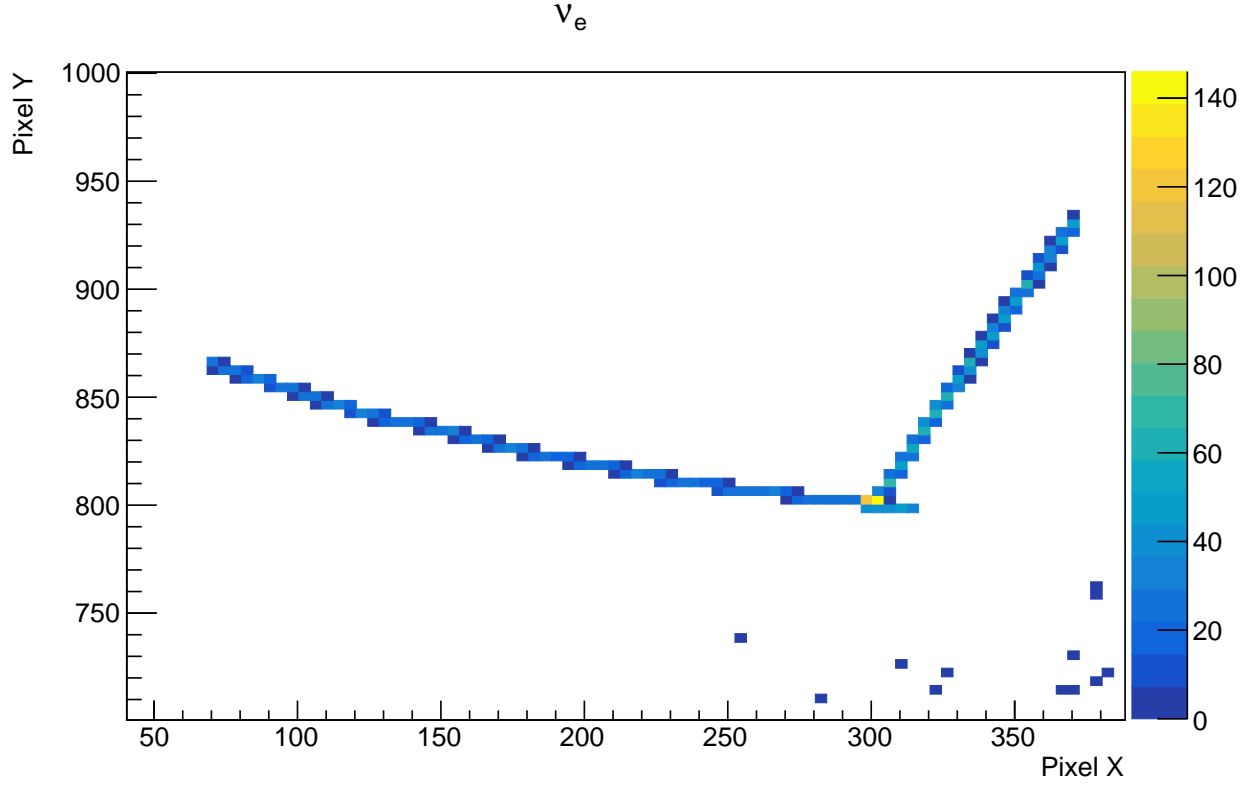
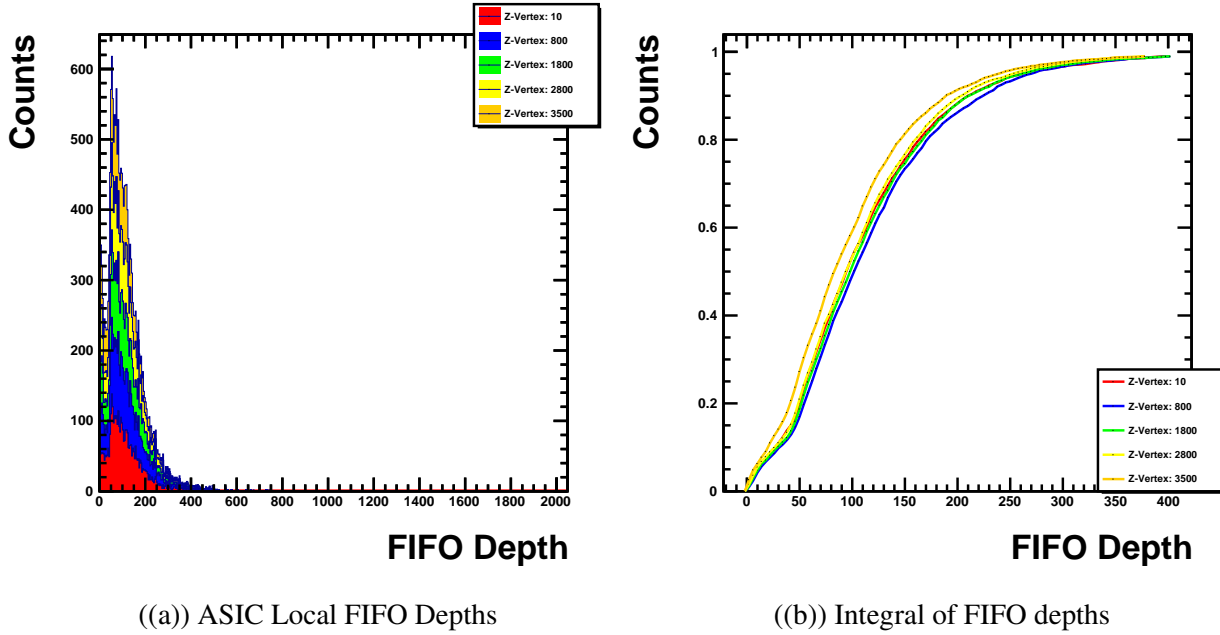


Figure 5.22: The same  $\nu_e$  event as the one shown in Figure 5.21-(A). The plot is zoomed into to the region of interest where the bin widths represent the pixels dimensions in the collection plane. The energy of this  $\nu_e$  was 546.1 MeV, and considering that each reset requires 0.1475 MeV, the maximum number of resets this event could produce is  $\approx 4368$ . The histogram records 3733 total resets. The most active pixel received 144 resets. When the pixels are binned into ASICs ( $4 \times 4$  pixels) the maximum number resets an ASIC received is 347.

Figure 5.30 and Figure 5.5 show the same integral results, but with different labeling. The results show two different distributions of buffer depths: those along the near-beam angle ( $\theta_z \approx 0^\circ$ ) and near the azimuthal angle ( $\theta_z \approx \pm 90^\circ$ ). The Table A.1 shows the complete list of values for the required local FIFO depth for each combination of the 200 parameters for the 95% and 99% capture intervals.

The two different distributions indicate that there are at least two different design specifications for future Q-Pix prototypes. The first capture distribution has a maximum value of 426. Therefore, a Q-Pix ASIC with a local FIFO depth of 426 would be able to fully capture resets for 99% of all neutrino interactions under 10 GeV and momentum within  $\pm 2^\circ$  of the beam axis. In order for



((a)) ASIC Local FIFO Depths

((b)) Integral of FIFO depths

Figure 5.23: Example  $\nu_e$  events for different z-position of the vertex with  $\theta_z = 0$  held constant. Plot (A) bins the maximum value of local FIFO depth for all 3900 events ( $\nu_l$  energies between 250 MeV - 10 GeV) for variable z-position and  $\theta_z = 0$ . Plot (B) shows the running integral for each histogram shown in plot (A). The integral continues until 99% of all events are counted. This process is repeated for all 200 possible parameter choices as discussed in Table 5.5.

Q-Pix to record all resets of the same energy average energy but with momentum near the azimuthal ( $\theta_z \approx \pm 90^\circ$ ) it would require a buffer depth of 1670.

## 5.6 Q-Pix for Neutrino Oscillation Measurements

The LBNF beam flux, neutrino oscillations, and neutrino cross-sections all affect the predicted neutrino event rate at the DUNE-FD. Instead of applying these factors the previous analysis tested neutrino interactions from a uniform distribution of true incident energy. We discuss Q-Pix's back-end requirements and extend our back-end analysis to the expected neutrino (dis)appearance spectra as presented in [12]

To account for neutrino oscillation appearance probability as a function of energy, we weight each neutrino event based on the expected (dis)appearance spectra for each (anti)neutrino flavor as shown in Figures section 5.6. Since both flavors of (anti)neutrino have the peak of the distribution is below 5 GeV, and the previous use a uniform weighting for events up to 10 GeV the required buffer depths are an over estimate. Lower average energy interactions will produce less resets, which will require

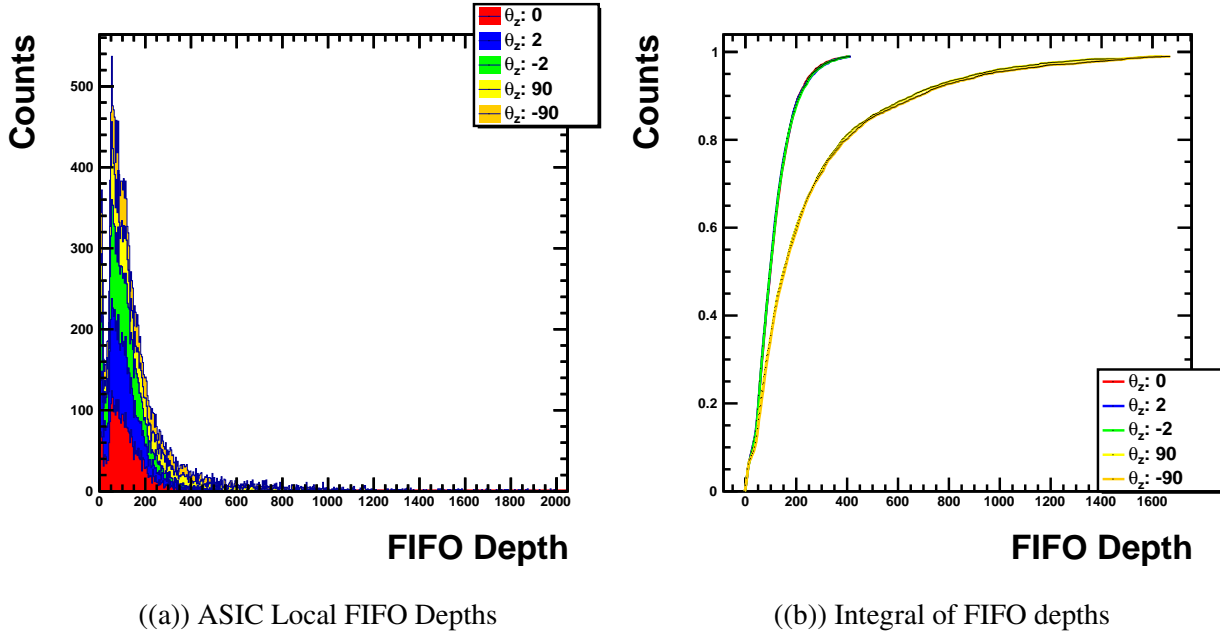
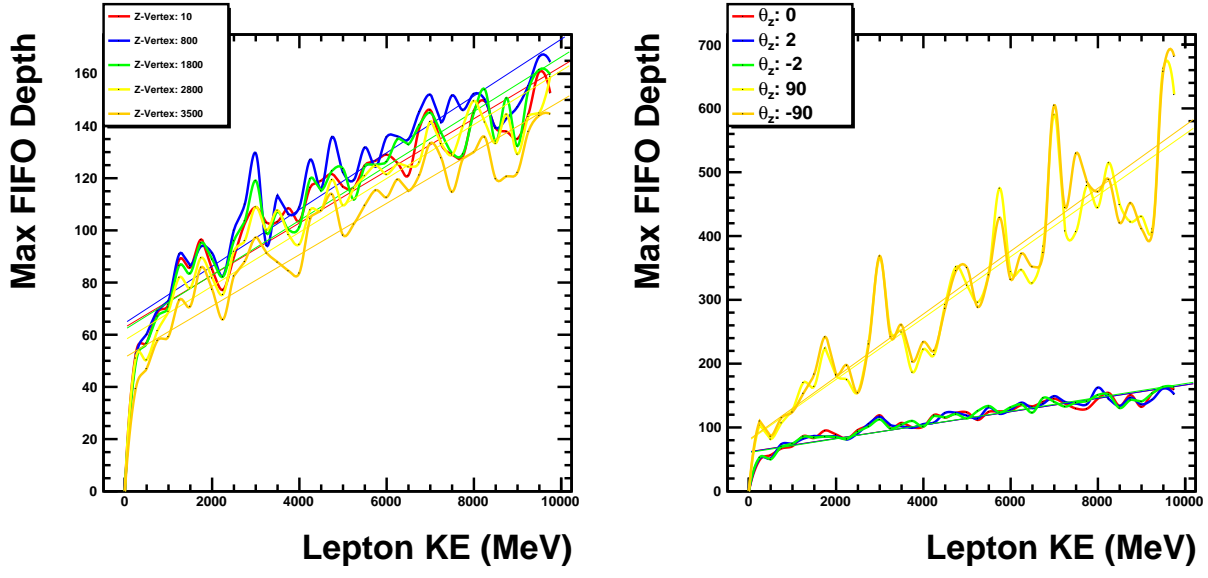


Figure 5.24: Example  $\nu_e$  events for different  $\theta_z$  with the vertex held constant with z-position = 180 cm. This is a similar plot to Figure 5.23 with the exception that  $\theta_z$  is varied and the z-position is held constant at  $z = 180$  cm. A notable difference to note here is the run away effect of the large values of  $\theta_z$ . This effect is intuitive: the initial momentum direction affects the direction of where most charge will be deposited. As more charge is localized an ASICs area, it will collect more resets.

smaller buffer sizes. Figure 5.5 clearly shows the relationship between the energy deposited and the number of resets collected. The FIFO depth requirements for neutrino oscillation measurements at the DUNE-FD are shown in Figure 5.6.

## 5.7 Neutrinos, Backgrounds, and Routing

A valid full reconstruction requires all packets to be collected regardless of neutrino type, energy within the valid range, interaction vertex, and should also be able to accept a range of incoming momentum angles. In this final section of the chapter we combine the results of the neutrino interactions as well as the radiogenic and leakage backgrounds into the simulation framework described in Section 5.1, which is based on the graph developed in Chapter 4. This back-end



((a)) Constant  $\theta_z = 0$  direction.

((b)) Constant Z-Position:  $Z = 180$  cm.

Figure 5.25: Comparison of buffer depths as a function of energy for different parameters of  $\theta_z$  and z-position. There is a large variance between the true  $\nu_l$  incident energy and the actual energy deposited in the LAr. This is the reason why only the means are plotted for each energy bin. Plot-(A) shows that the average z-position has a minor affect on the overall local FIFO depth, where the furthest position has the lowest average reset count. Plot-(B) shows average FIFO depth for varied  $\theta_z$ . The two curves represented by  $\theta_z = \pm 90^\circ$  are similar because they use the same seeded events only pointed up or down, and should have the symmetrical effect since vertex is located in the center of the APA.

simulation framework is also my sole and independent work.

### Combining the Digital and Physical Simulations

To synthesize the results of the neutrino events and the background sources we take a reference 10 second window slice from a 1000 second simulation of backgrounds as described in Section 5.3. We then select a single  $\nu_e$  interaction from the forward horn current direction, where we accept any incoming  $\theta_z$ , z-position, and energy. This event is offset to occur at time:  $\tau_{int} = 5.1$  seconds. We do not perform this readout simulations for all parameters in Table 5.5 as Figure 5.31 indicates that the local buffer requirement does not largely depend on neutrino flavor.

We choose  $\tau_{int} = 5.1$  s so that the interaction occurs just after interrogation request from the aggregator node. This ensures that the entire  $\nu_e$  interaction is buffered onto all local FIFOs in the tile before the request. We note that this time offset is the same for the push architecture, even

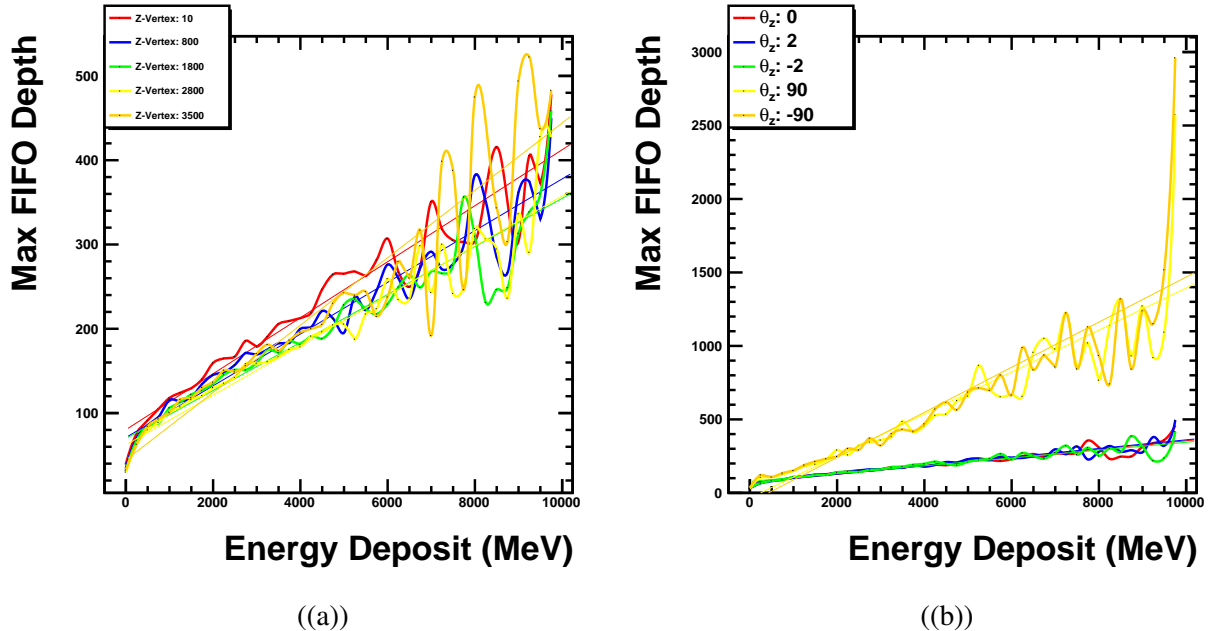


Figure 5.26: A comparison of ASIC resets vs the energy deposited into the LAr. Plot-(B) shows for Z-position=10 cm ends at  $\approx 2$  GeV since no  $\nu_e$  events deposit this much energy into the LAr. Both plots indicate that the

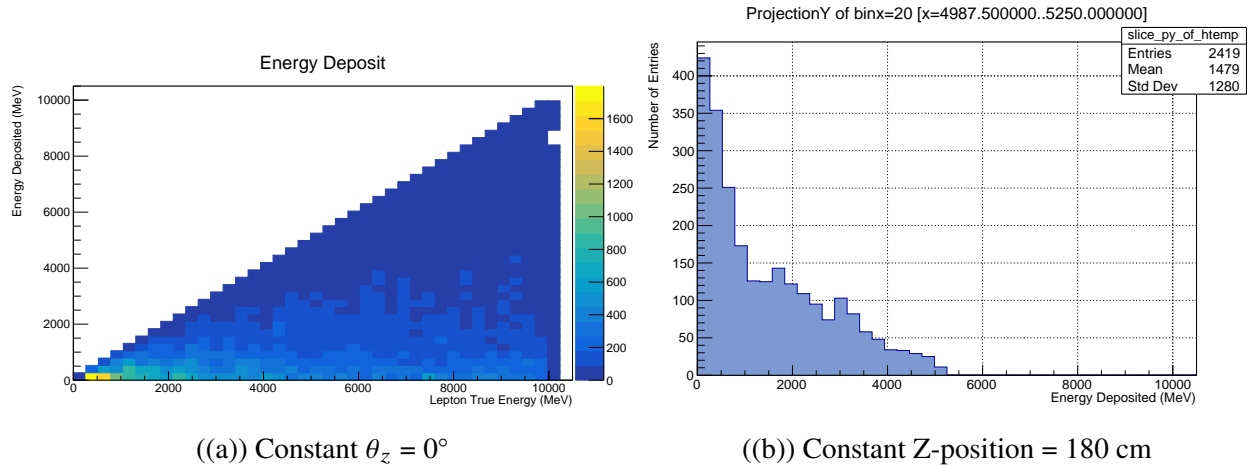


Figure 5.27: Plot-(A) shows a comparison of the energy deposited into the LAr as a function of the input neutrino ( $\nu_e$ ). Plot-(B) shows a projection against the y-axis for a single bin. The maximum allowed total energy deposited is limited to the total energy of the input neutrino. However, the lower bound for all energies is still, obviously, zero. Therefore, as the input neutrino energy increases the upper bound also increases. The mean value of Plot-(B) indicates that even for a maximum allowed total energy of 5 GeV the mean (average) energy deposited per event is 1479 MeV. Most interactions deposit less than 2 GeV into the LAr, as shown in Figure 5.27. Some pileup events are removed, see Figure 5.5.

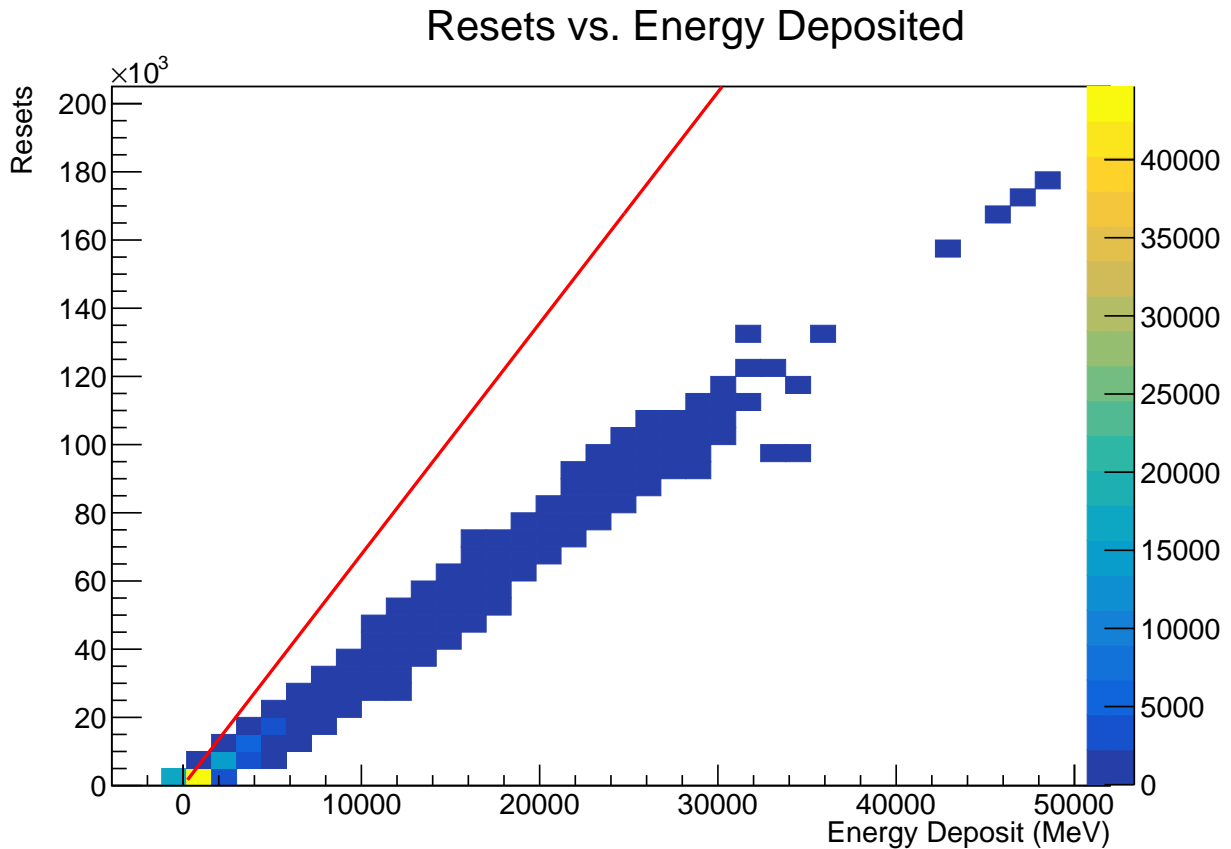


Figure 5.28: A relationship between the total number of resets detected in the APA and the energy deposited for  $\nu_e$  interactions is shown. The solid red line indicates the maximum number of resets that could be measured for a given energy. The small distribution of energies below zero correspond to events that produced no resets. The energy deposited goes above the the threshold limit of 10 GeV. These events carry extra energy from additional leptons which are from pile-up at the DUNE-ND from the FNAL beam. These data are not included in the energy deposited analysis, or in the integrals as shown in Figure 5.21. These high energy deposit events are also not included in the FIFO depth analysis, since these events are beyond the energy range for oscillation measurements. These events are also removed from Figure 5.27.

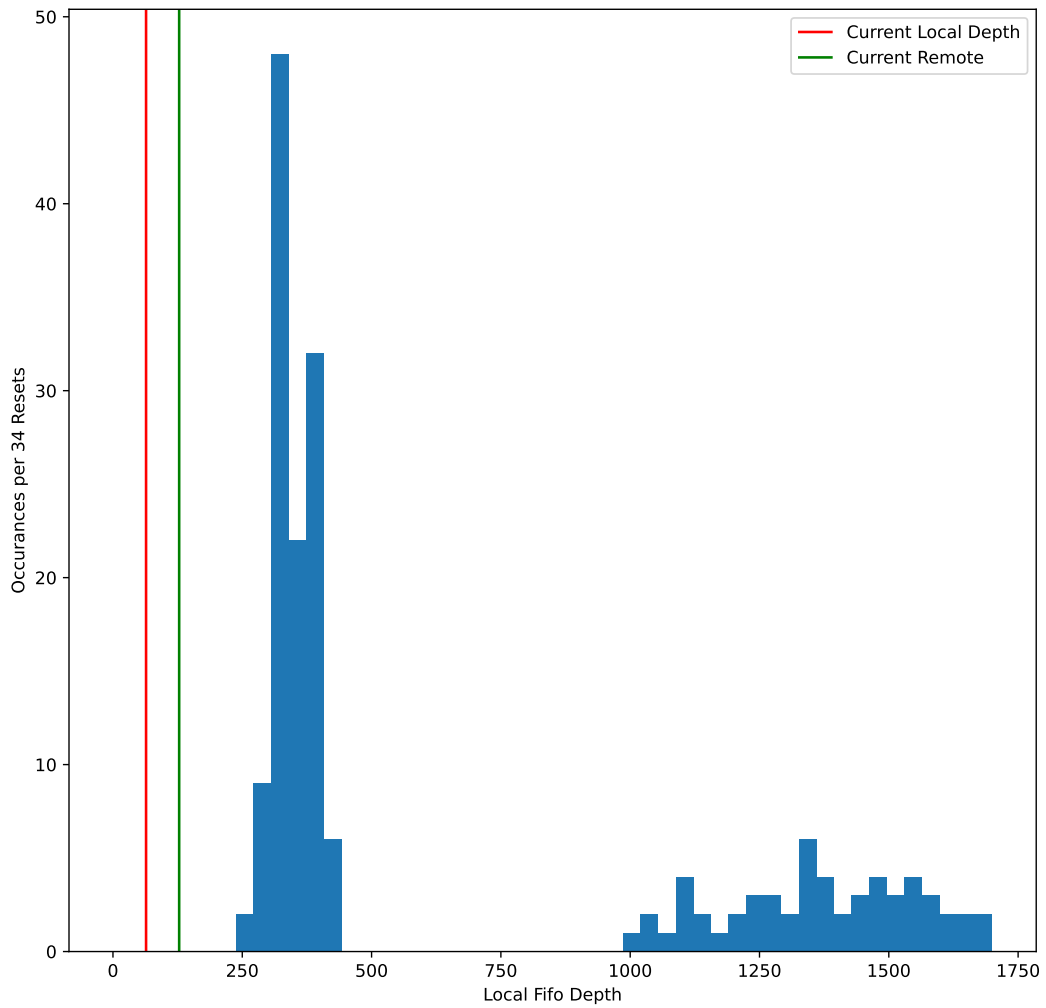
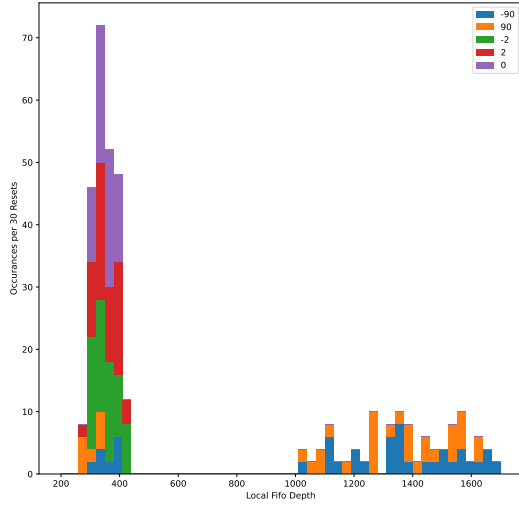
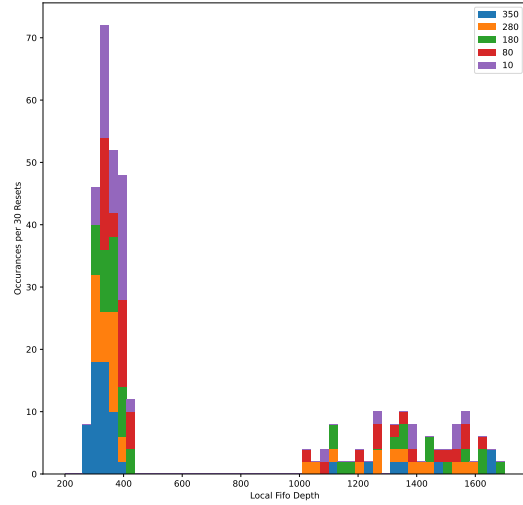


Figure 5.29: Total integral data for all neutrino event parameters described in Table 5.5. The values of the integrals binned in this figure can be found in Appendix A. These data clearly indicate two different distributions of FIFO requirements. The final Q-Pix design will choose some local FIFO depth. The current Q-Pix digital prototype local and remote FIFO depths are also shown by the red and green lines, respectively. The data in this plot required 6520 electrons to produce a single reset ( $C_{pixel} = 1 \text{ fC}$  and  $V_{pixel} = 1 \text{ V}$ ). Should the pixel's capacitance or voltage change, the x-axis of this plot would scale approximately by the same factor.



((a)) Colored by  $\theta_z$  direction.



((b)) Colored by Z-position

Figure 5.30: Comparison of buffer depths integrated over energy colored by different parameters of  $\theta_z$  and z-position. The most important result is shown in Plot-(A), which clearly indicates that only two different parameters account for the distribution of larger local FIFO depths. As expected,  $\theta_z$  affects the localization of charge over individual ASICs which affect the local FIFO depth. Plot-(B) shows the distribution of resets indicated by different z-positions. Plot-(B) differs in that the second distribution of resets contains elements from each of the different z-positions.

though the neutrino reset packets will be sent when they are acquired.

### Remote FIFO Depth Results

Figure 5.35 shows combined results for the remote transactions, remote FIFO depth, and 99% capture requirements. The remote transactions for both the left and trunk routings are much smaller on average than the snake routing for the reasons described in Section 5.3.

The Table 5.5 contains the results for the effect the different routings have on the average number of transactions.

The Table 5.6 summarizes the results of Plot-(B) in Figure 5.35 for the parameters described in Table 5.2.

The Table 5.7 summarizes the linear fit results of Plot-(D) in Figure 5.35 for the parameters described in Table 5.2. The final column of this table indicates the relative fit from the push-based architecture, for which only the snake routing was tested.

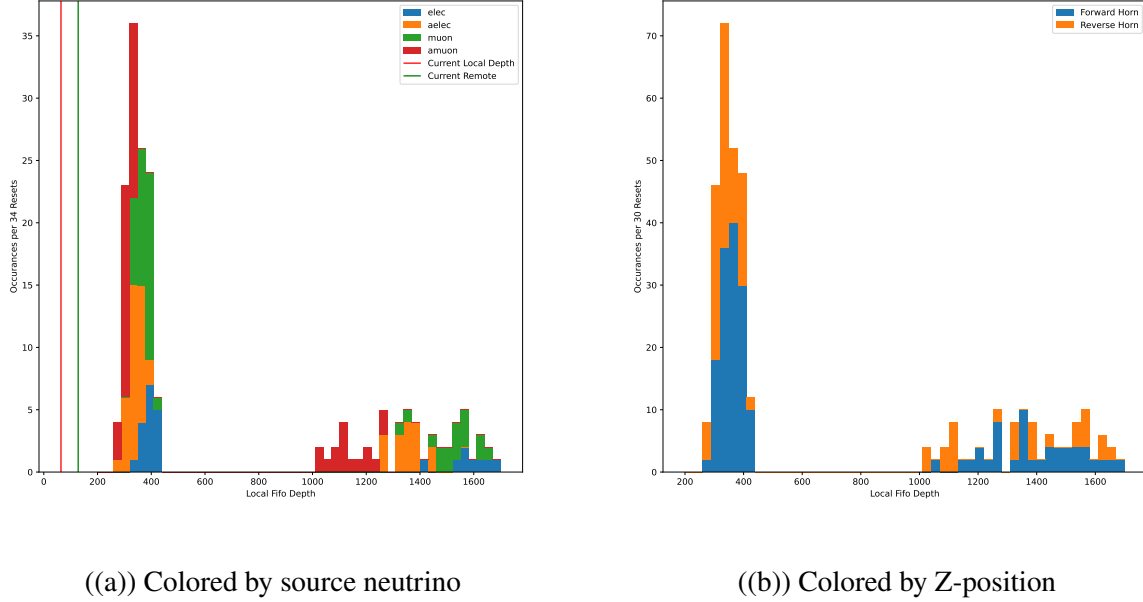


Figure 5.31: Comparison of buffer depths as in incoming prototype and horn current direction from neutrino beam. Plot-(A) indicates that there is not a large average difference between the different neutrino flavors and local FIFO depth. Plot-(B) indicates that the different flux from the two horn currents also do not measurably affect the two different distributions. Plot-(A) however does show a slight difference between  $\nu_e$  and  $\bar{\nu}_\mu$ .  $\nu_e$  has an average local FIFO depth of 394 in the small distribution, where  $\bar{\nu}_\mu$  has an average of 313. Most ( $\geq 65\%$ ) of this difference is accounted for the fact that the selected  $\nu_e$  near-beam ( $\theta_z = \pm 2^\circ, 0^\circ$ ) events deposited more energy, 1894 MeV than the  $\bar{\nu}_\mu$  events 1219 MeV, causing more resets. After the energy correction the mean FIFO depths differ by less than one standard deviation.

Freq.	Tile Size	Avg. Local Hits	S. Tot	S. Per.	L. Tot.	L. Per.	T. Tot.	T. Per.
5%	16	772.001	423.293	42.329	166.403	16.640	138.380	13.838
0.5%	16	829.541	449.861	44.986	177.357	17.736	147.346	14.735
5%	64	2184.255	1332.440	133.244	286.929	28.693	227.595	22.759
0.5%	64	2321.148	1400.794	140.079	301.775	30.178	239.087	23.909
5%	140	3712.921	2298.912	229.891	355.037	35.504	262.448	26.245
0.5%	140	3944.215	2416.778	241.678	373.173	37.317	275.614	27.561
5%	256	6231.886	4020.649	402.065	465.629	46.563	354.405	35.440
0.5%	256	6592.433	4209.196	420.920	487.090	48.709	370.695	37.070

Table 5.5: Transaction Data

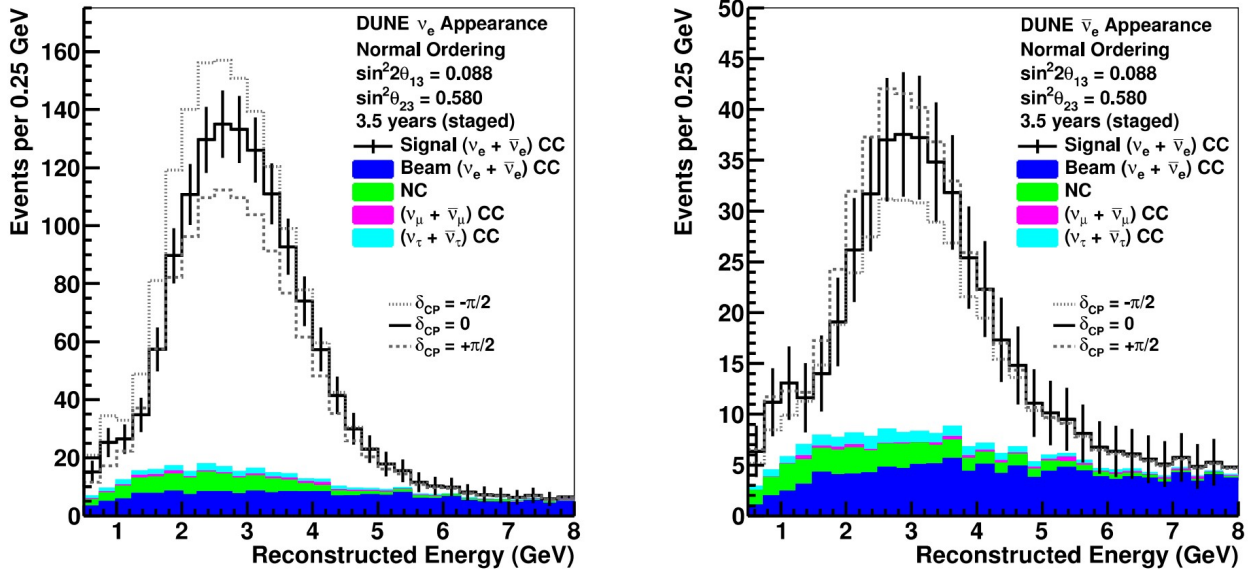


Figure 5.32: Figure is taken from from the DUNE-FD TDR [12]. Images show the  $\nu_e$  and  $\bar{\nu}_e$  appearance spectra respectively. The left image shows the reconstructed energy distribution for the beam running in the forward horn current direction for 3.5 years. The weight of appearance spectra decreases with increasing energy beyond  $\approx 8$  GeV and has a maximum between 1 and 2 GeV.

Freq.	Tile Size	Local Hits	95-S	99-S	95-L	99-L	95-T	99-T
5%	16	939	320	1014	535	1736	607	1971
0.5%	16	1014	322	975	603	1949	652	2125
5%	64	1200	598	2191	1098	4394	975	4295
0.5%	64	1307	403	1328	970	4298	974	4521
5%	140	1182	852	3486	1455	6558	1343	6309
0.5%	140	1393	440	1464	1327	6616	1382	6757
5%	256	1456	1039	3637	2026	7679	2008	8250
0.5%	256	1670	527	1668	1773	7460	1784	7368

Table 5.6: Buffer Data

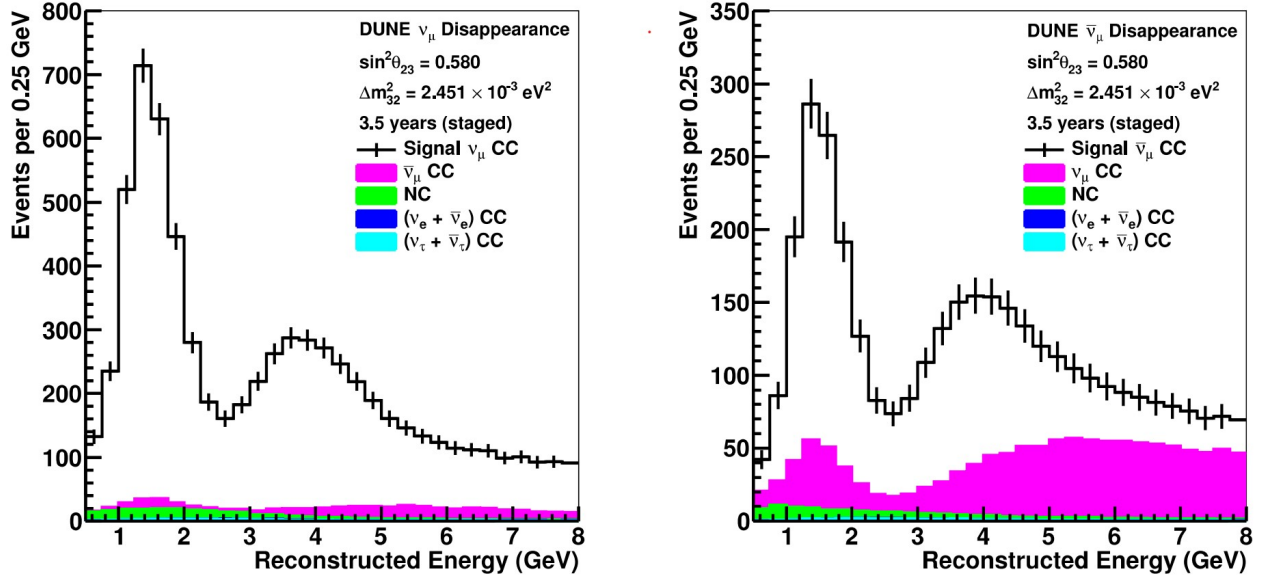


Figure 5.33: Figure is taken directly from the DUNE-FD TDR [12]. Images show the  $\nu_\mu$  and  $\bar{\nu}_\mu$  disappearance spectra respectively. The plots assume normal mass ordering and are also staged for 3.5 years (staged) exposure for the beam running in the forward horn current and 7 years in the reverse horn current. The weight of disappearance spectra decreases with increasing energy beyond  $\approx 8$  GeV and has a maximum between 1 and 2 GeV.

Freq.	Tile Size	Snake Fit	Left Fit	Trunk Fit	Push Fit
5%	16	1.041	1.823	2.082	0
0.5%	16	0.948	1.879	2.039	0
5%	64	1.623	3.176	2.969	0
0.5%	64	1.006	2.514	2.727	0
5%	140	1.966	3.506	3.481	0
0.5%	140	1.021	3.033	3.131	0
5%	256	1.981	3.616	3.913	0
0.5%	256	1.027	3.243	3.336	0

Table 5.7: Transaction Fit Results

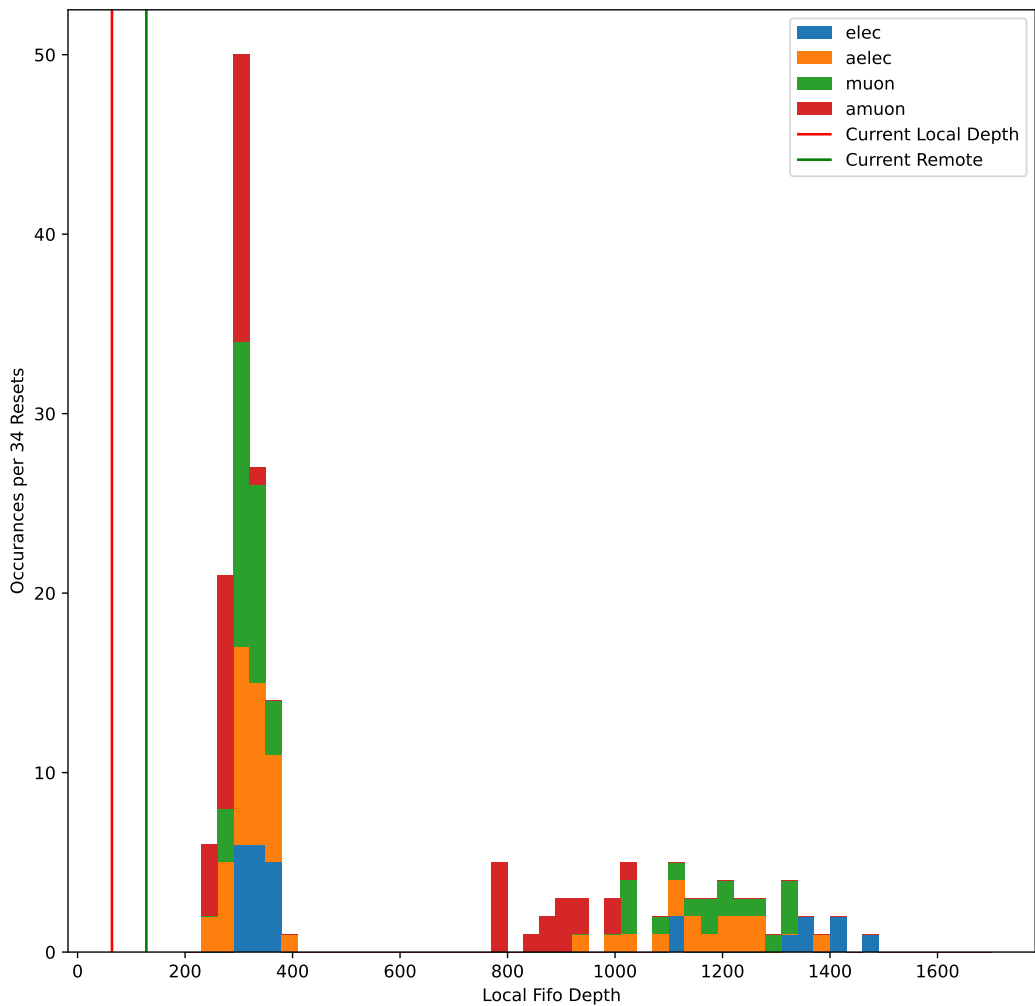


Figure 5.34: Weighted integrals for all neutrino event parameters, with weights drawn from the expected signal curves from Figure 5.6 and Figure 5.6. This plot is similar to Figure 5.5, with the exception that the interaction weights are drawn for the (dis)appearance spectra expected at the DUNE-FD module. The buffer for the oscillation measurements require 394 compared to the uniform interaction energy of 426.

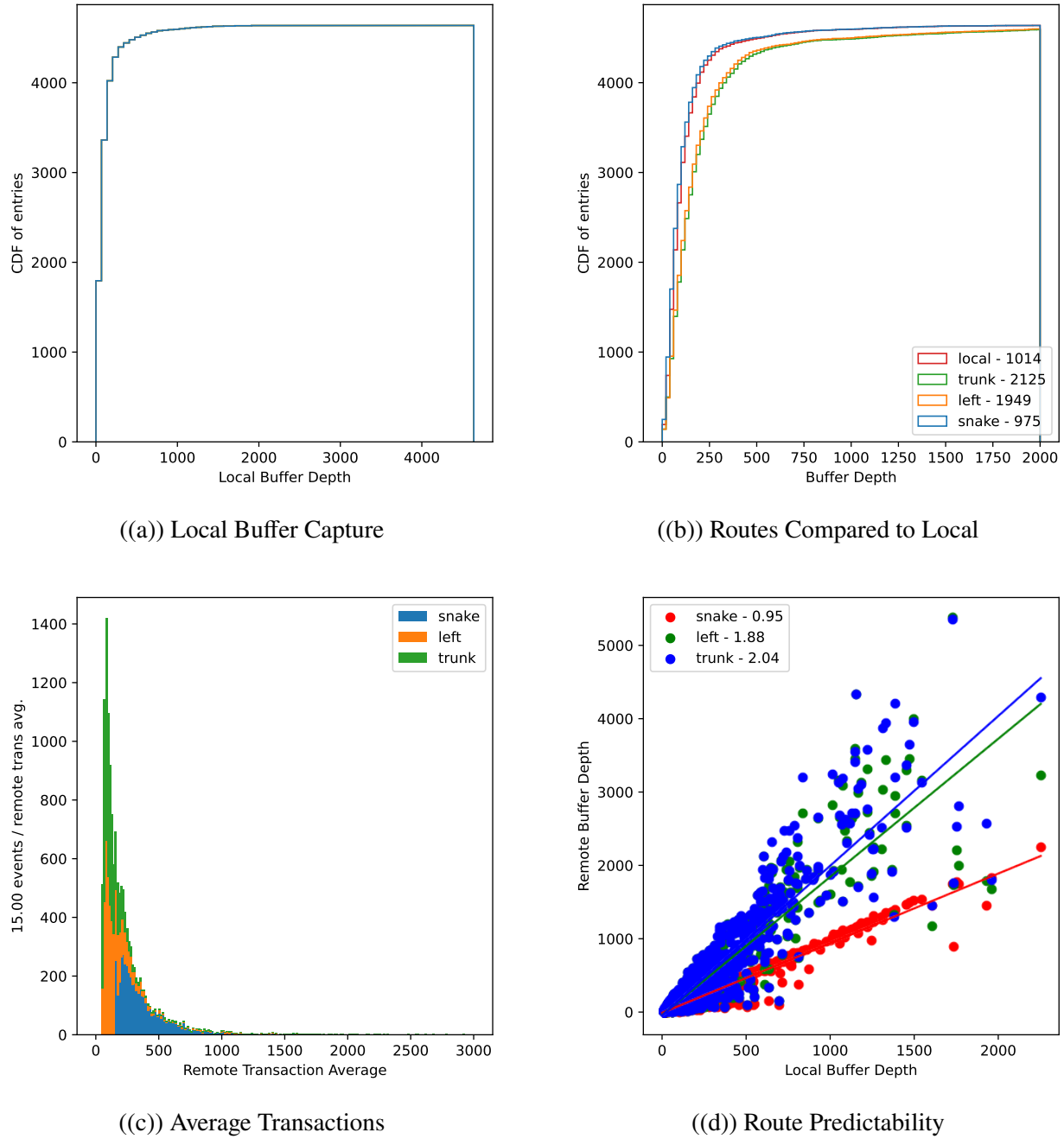


Figure 5.35: The results for a pull-based  $4 \times 4$  tile with 0.5% frequency drift is shown. Plot-(A) shows the cumulative integral of the number of events that are fully captured as a function of the local buffer depth. Plot-(B) includes the three tested routings against the local buffer depth. The "Snake" routing is the only routing which limits the the remote FIFO depth near the local FIFO depth. Plot-(C) shows the relationship of the average number of transactions for all ASICs in each of the events. Plot-(D) is a scatter plot of the remote depth as a function of the local depth. The legend shows the slope values for linear best fits, which help guide the eye to show how the routes scale differently for large input events.

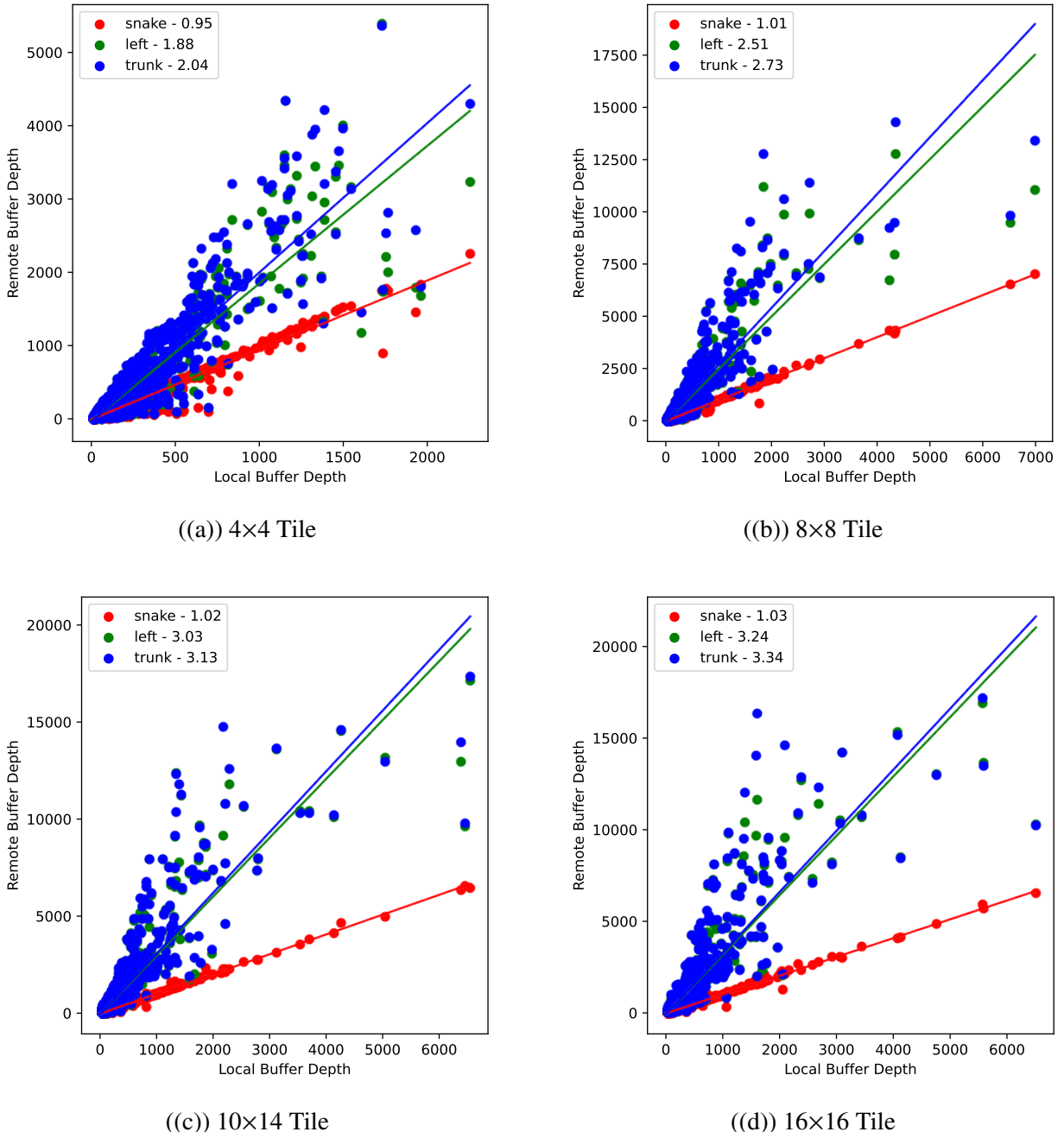


Figure 5.36: A comparison of the remote vs local FIFO depths for different tile sizes is shown. Each plot corresponds to a different tile size with a frequency distribution of 0.5%. Plot-(A) shows that even at small tile sizes (4x4) the remote buffer depths do not predictably scale with the local depths. Both the "Left" and "Trunk" routings slope's increase with the tile size to a maximum value over 3. Only the "Snake" routing maintains a predictable relationship between local and remote depths, as well as unit slope. These data indicate that any future routing for a Q-Pix tile, regardless of size, would need to dynamically route itself into a "Snake" routing in the event of SPF.

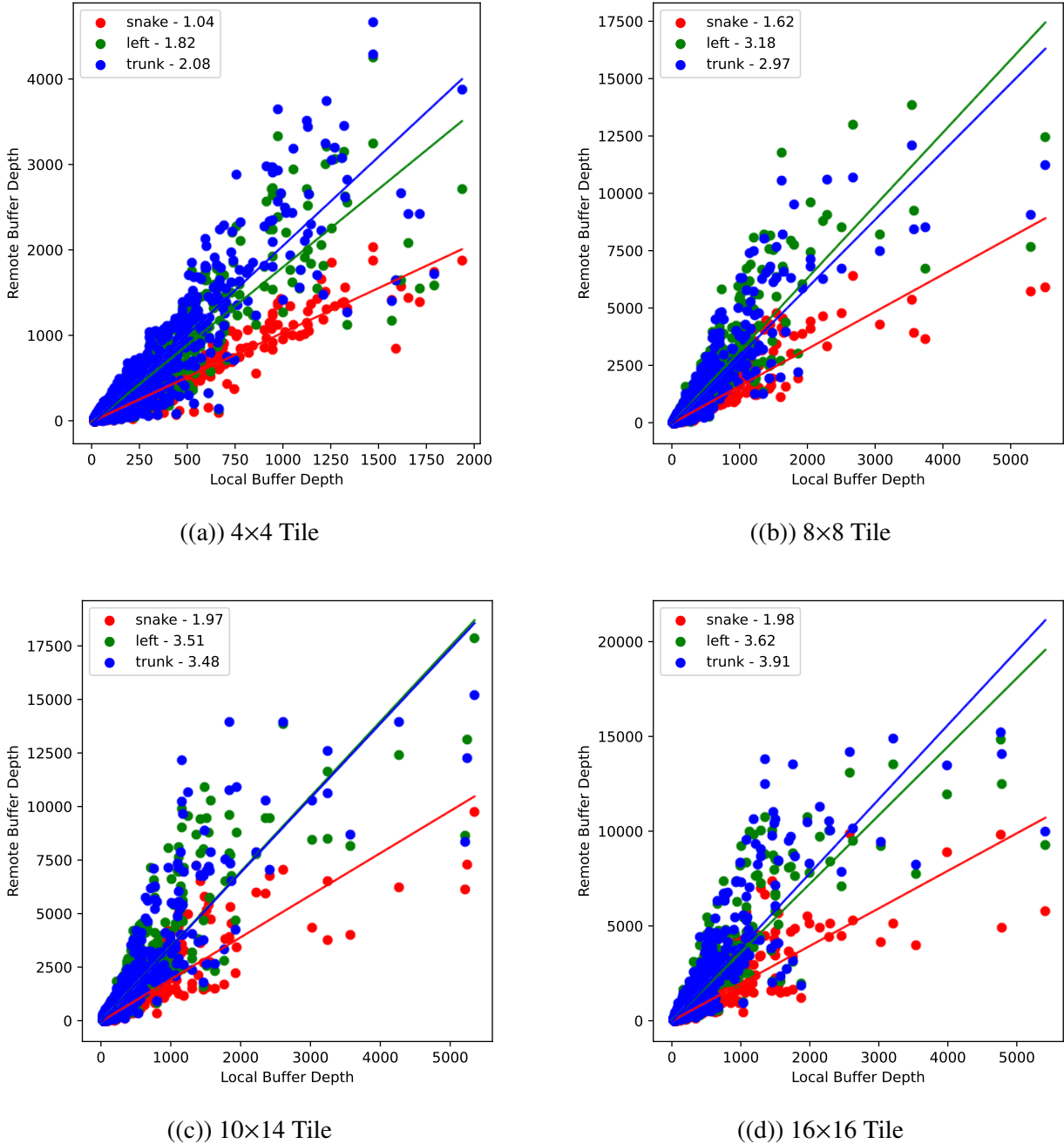


Figure 5.37: A comparison of the remote vs local FIFO depths for different tile sizes is shown. Each plot corresponds to a different tile size with a frequency distribution of 5%. This plot is identical to Figure 5.36, except that the frequency distribution is 5% instead of 0.5%. These results indicate that low frequency variance between neighbor nodes is essential in order to have a predictable remote FIFO depth response based on the snake routing. Not only is the fit poor in Plot-(D) for the  $16 \times 16$  tile, but the slope has also doubled. This means that, on average, the requirement for the remote FIFO depth would be double that of the requirement on the local FIFO depth.

## 5.8 Summary and Further Studies

The results presented in this section provide first physical analysis of the Q-Pix digital readout. Included in the analysis are long exposure to radiogenic background sources, leakage current, neutrino beam events, and the response of the digital back-end ASICs. All events occur in a  $2.3 \times 6.0 \text{ m}^2$  LAr container, with a maximum drift distance of 3.6 m. The parameters of the Geant4 simulation are identical to those in Table two from [9] with the exception that the sampling time is configured to each digital node as described in Section 5.1. The flux of beam neutrino events are taken from ?? also using GENIE [16] v2.12.10.

We find that the digital back-end readout permits the ability to fully capture 99% events from beam neutrino events up to 10 GeV provided the local FIFO depth is at least 426. Each ASIC would be able to record all resets from these neutrino events regardless of incident neutrino momentum direction if the local FIFO depth is 1670. These results present an expected upper-bound of the required local and remote FIFO depths for the digital ASIC, since most electrons of reconstructed energy for neutrino oscillations (See Chapter 5 from [77]) expected to be less than 4 GeV, while the analysis presented here are for events up to 10 GeV.

The current Q-Pix digital prototype allows for dynamic and configurable routing. We find that the only stable relationship between the local FIFO depth and the remote FIFO depth occurs for the "Snake" based routing, where the required depths are approximately equal. Additionally, the relationship between these FIFO depths are independent of tile size, which imply that tiles of any size should reconfigure itself to always have an effective "Snake" routing in the event of SPF.

We also find no difference in the ability of a "push" architecture to better alleviate neutrino events than the current "pull" based architecture. The reason for this is due to the quick arrival time of neutrino resets compared to the average packet transaction time.

In order for a "push" architecture to be able to reduce both the remote and local FIFO depth requirements the average packet transaction time would have to be small compared to the average RTD on each node. The total decrease of the packet transaction time will likely have to be an order of magnitude, or more, according to Figure 5.8 The distribution of RTDs for the example scatter event clearly indicate that most of the resets come within 1  $\mu\text{s}$  of each other. Since the current packet transaction time is, on average  $\approx 50 \mu\text{s}$ , for the push architecture to transfer packets more quickly than they arrive the packet transaction time would have to decrease by about a factor of 50.

A combination of changes could make this possible: a faster local oscillator, a different commu-

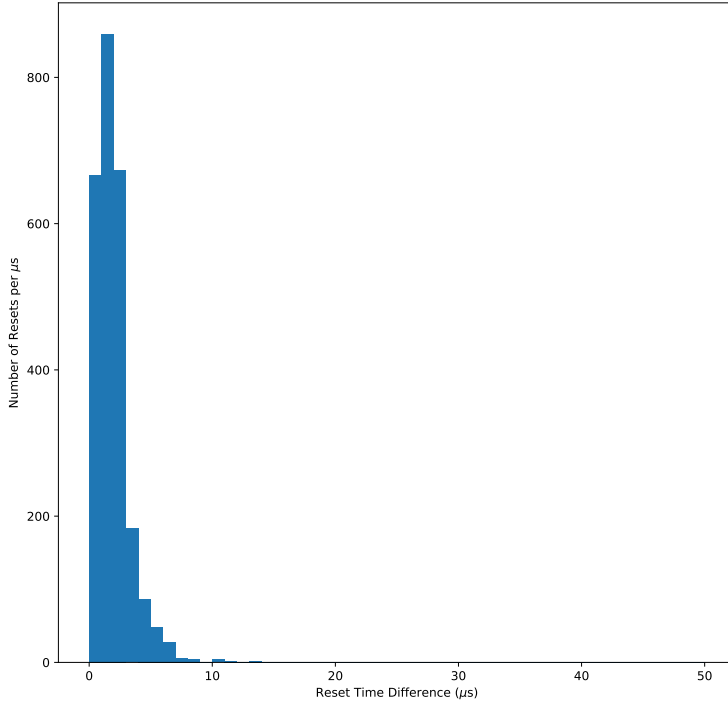


Figure 5.38: A calculation of all of the Reset Time Differences (RTDs) for the example scatter event shown in Figure 5.21. A packet transaction takes  $\approx 50 \mu s$  to occur. The distribution of RTDs for a scatter event indicate that most of the resets occur separated by less than  $1 \mu s$ .

nication protocol, and zero-suppresion on some packet data. Future designers will have to ask themselves if a redesign of the digital clock, the packet communication protocol, and/or the FSM of the digital ASIC is easier than increasing two FIFO depths. It is the humble opinion of the author of this work that it is not.

Finally, we remark how much the digital ASIC is capable of, despite it's seemingly simple design 4.2. In the spirit of the Q-Pix's principle of least action, we assert that the digital ASIC should be also be as simple as possible while relaying all data required for the application.

## SUMMARY AND OUTLOOK

### 6.1 Conclusions

The results presented in this work provide the first tests and verification of the digital back-end for novel pixel readout technology targeted at liquid Argon Time-Project-Chambers.

The first Q-Pix analog prototype using Off-The-Shelf analog components has been built and is currently taking measurements. This prototype promises to provide gaseous Argon diffusion measurements, which will likely be the first true physics measurement using a Q-Pix based readout.

We have built and verified the first digital prototype boards which have verified communication reliability to protect against potential data loss. We developed a frequency calibration method for remote nodes to demonstrate Q-Pix's ability to have independent oscillators. We used this prototype and verified the ability to reconstruct remote oscillator frequencies with a precision more than an order of magnitude required ( $0.1 \text{ ppm} < 1 \text{ ppm}$ ). These results are verified between two different interrogation frequencies.

We developed multiple simulations to model the detector's response to long ( $1000 \text{ second}$ ) run time exposure of radiogenic backgrounds as well as tested the ability to readout beam neutrino events at LBNF. Our simulations show that the current ASIC's local (64) and remote (128) FIFO depths of the digital ASIC prototype are too small to GeV scale neutrino events in a DUNE-FD. We estimate that the local FIFO depth should be at least be able to record 426 unique resets in order to fully capture 99% of neutrino events with energy up to 10 GeV. These results are modified to a required 394 when accounted for expected (dis)appearance spectra given in [12]. This result provides the first limit on the memory required for a Q-Pix ASIC, should it be used in a DUNE-FD module to measure neutrino oscillations.

To test the remote FIFO depths and local oscillator frequency requirements we developed the first simulation to model the Q-Pix digital back-end response to physical events within a DUNE-FD APA. We find that the distribution of the ASIC frequency needs to be  $\approx 0.5\%$  in order to maintain obtain reliable remote FIFO depths with the current readout protocol. These results also indicate that the only reliable routing methodology is the "Snake" routing (Section 5.3), which is shown to be independent of both tile size and digital architecture (See Table 5.2). The routing ("Snake")

provides a unitary relationship between the local and remote FIFO depth requirements.

### The Future of Q-Pix

The Q-Pix design is a novel readout technology. However, "novelty does not confer automatically benefit", David Nygren. The full Q-Pix validation still awaits key results to demonstrate its capabilities in a DUNE-FD module. Namely, Q-Pix still needs to test both the analog and digital prototypes at cold liquid Argon temperatures.

The front-end requires a reliable replenishment circuit as well as low leakage current ( $\approx 100$  aA or less to be below radiogenic backgrounds). Also, when known, the timing response of the replenishment circuit should be applied to the RTD results presented in this work. Knowledge of the timing response of the analog front-end can be combined with the neutrino simulation events shown here to allow for accurate event reconstruction. These reconstructed events will permit an analysis to estimate of Q-Pix's ability to perform neutrino oscillation measurements.

### Q-Pix's First and Second Digital Prototypes

The work presented here can accurately be viewed both as a means to understand the Q-Pix's first digital ASIC and as a guide toward the second digital design. The key result of this work indicates that the local and remote FIFO depths of the second prototype should both be increased to at or above 394 to capture 99% of neutrino oscillation interactions. The reason the first prototype did not incorporate these larger buff sizes was due to fabrication limitations of the ASIC. If oscillator tests of the first prototype indicate that the mean drift between neighbor ASICs is reliably under 0.5%, then the local oscillator need not be changed either. All other underlying logic, with perhaps the exception of FWFT FIFOs, have been verified in the first digital prototype. These tests need only be repeated on the first prototype ASIC.

Eventually the Q-Pix front and back-end ASICs will likely be combined into a single chip. Still, the motivation provided by the results presented here for the second prototype (applied only to the digital portion) remain unchanged.

## BIBLIOGRAPHY

- <sup>1</sup>D. Dominguez, *Cern accelerating science*, 2015.
- <sup>2</sup>J. L. Hewett et al., *Fundamental physics at the intensity frontier*, 2012.
- <sup>3</sup>B. Abi et al., “Volume i. introduction to dune”, *Journal of Instrumentation* **15**, T08008 (2020).
- <sup>4</sup>X. Qian and P. Vogel, “Neutrino mass hierarchy”, *Progress in Particle and Nuclear Physics* **83**, 1–30 (2015).
- <sup>5</sup>R. Acciarri et al., *Long-baseline neutrino facility (lbnf) and deep underground neutrino experiment (dune) conceptual design report volume 1: the lbnf and dune projects*, 2016.
- <sup>6</sup>D. Nygren and Y. Mei, *Q-pix: pixel-scale signal capture for kiloton liquid argon tpc detectors: time-to-charge waveform capture, local clocks, dynamic networks*, 2018.
- <sup>7</sup>B. Abi et al., “Volume iv. the dune far detector single-phase technology”, *Journal of Instrumentation* **15**, T08010 (2020).
- <sup>8</sup>M. Rooks, S. Abbaszadeh, J. Asaadi, M. Febbraro, R. W. Gladen, E. Gramellini, K. Hellier, F. M. Blaszczyk, and A. D. McDonald, *Development of a novel, windowless, amorphous selenium based photodetector for use in liquid noble detectors*, 2022.
- <sup>9</sup>S. Kubota et al., “Enhanced low-energy supernova burst detection in large liquid argon time projection chambers enabled by q-pix”, *Phys. Rev. D* **106**, 032011 (2022).
- <sup>10</sup>*Precision switched integrator transimpedance amplifier*, PDS-1329A, IVC 102 datasheet, Texas Instruments (1996).
- <sup>11</sup>A. A. Abud et al., “Deep underground neutrino experiment (dune) near detector conceptual design report”, *Instruments* **5**, 10.3390/instruments5040031 (2021).
- <sup>12</sup>B. Abi et al., *Deep underground neutrino experiment (dune), far detector technical design report, volume ii: dune physics*, 2020.
- <sup>13</sup>R. L. Workman and Others, “Review of Particle Physics”, *PTEP* **2022**, 083C01 (2022).
- <sup>14</sup>*Liquid Argon Properties (Tables and Calculators) kernel description*, <https://lar.bnl.gov/properties/>, Accessed: 2023-01-04.
- <sup>15</sup>I. Esteban, M. C. Gonzalez-Garcia, M. Maltoni, T. Schwetz, and A. Zhou, “The fate of hints: updated global analysis of three-flavor neutrino oscillations”, *Journal of High Energy Physics* **2020**, 178, 178 (2020).

- <sup>16</sup>C. Andreopoulos et al., “The GENIE Neutrino Monte Carlo Generator”, *Nucl. Instrum. Meth. A* **614**, 87–104 (2010).
- <sup>17</sup>S. L. Glashow, “Partial-symmetries of weak interactions”, *Nuclear Physics* **22**, 579–588 (1961).
- <sup>18</sup>A. Salam and J. C. Ward, *Electromagnetic and weak interactions*, tech. rep. (IMPERIAL COLL OF SCIENCE and TECHNOLOGY LONDON (ENGLAND), 1964).
- <sup>19</sup>S. Weinberg, “A model of leptons”, *Physical review letters* **19**, 1264 (1967).
- <sup>20</sup>M. Gell-Mann, “The Eightfold Way: A Theory of strong interaction symmetry”, *10 . 2172 / 4008239* (1961).
- <sup>21</sup>M. Gell-Mann, “A schematic model of baryons and mesons”, *Physics Letters* **8**, 214–215 (1964).
- <sup>22</sup>J. J. Aubert, U. Becker, P. J. Biggs, J. Burger, M. Chen, G. Everhart, P. Goldhagen, J. Leong, T. McCorriston, T. G. Rhoades, M. Rohde, S. C. C. Ting, S. L. Wu, and Y. Y. Lee, “Experimental observation of a heavy particle  $J$ ”, *Phys. Rev. Lett.* **33**, 1404–1406 (1974).
- <sup>23</sup>E. D. Bloom, D. H. Coward, H. Destaebler, J. Drees, G. Miller, L. W. Mo, R. E. Taylor, M. Breidenbach, J. I. Friedman, G. C. Hartmann, and H. W. Kendall, “High-Energy Inelastic e-p Scattering at  $6^\circ$  and  $10^\circ$ ”, *prl* **23**, 930–934 (1969).
- <sup>24</sup>M. Breidenbach, J. I. Friedman, H. W. Kendall, E. D. Bloom, D. H. Coward, H. Destaebler, J. Drees, L. W. Mo, and R. E. Taylor, “Observed Behavior of Highly Inelastic Electron-Proton Scattering”, *prl* **23**, 935–939 (1969).
- <sup>25</sup>S. W. Herb et al., “Observation of a dimuon resonance at 9.5 gev in 400-gev proton-nucleus collisions”, *Phys. Rev. Lett.* **39**, 252–255 (1977).
- <sup>26</sup>S. Abachi et al., “Observation of the top quark”, *Physical Review Letters* **74**, 2632–2637 (1995).
- <sup>27</sup>S. H. Neddermeyer and C. D. Anderson, “Note on the nature of cosmic-ray particles”, *Phys. Rev.* **51**, 884–886 (1937).
- <sup>28</sup>M. L. Perl et al., “Evidence for anomalous lepton production in  $e^+ - e^-$  annihilation”, *Phys. Rev. Lett.* **35**, 1489–1492 (1975).
- <sup>29</sup>K. Kodama et al., “Observation of tau neutrino interactions”, *Physics Letters B* **504**, 218–224 (2001).
- <sup>30</sup>R. Brandelik et al., “Evidence for planar events in e+e- annihilation at high energies”, *Physics Letters B* **86**, 243–249 (1979).
- <sup>31</sup>D. P. Barber et al., “Discovery of three jet events and a test of quantum chromodynamics at petra”, *Phys. Rev. Lett.* **43**, 830–833 (1979).

- <sup>32</sup>G. Arnison et al., “Experimental observation of isolated large transverse energy electrons with associated missing energy at s=540 gev”, *Physics Letters B* **122**, 103–116 (1983).
- <sup>33</sup>G. Arnison et al., “Experimental observation of lepton pairs of invariant mass around 95 gev/c<sup>2</sup> at the cern sps collider”, *Physics Letters B* **126**, 398–410 (1983).
- <sup>34</sup>P. Higgs, “Broken symmetries, massless particles and gauge fields”, *Physics Letters* **12**, 132–133 (1964).
- <sup>35</sup>G. Aad et al., “Observation of a new particle in the search for the standard model higgs boson with the atlas detector at the lhc”, *Physics Letters B* **716**, 1–29 (2012).
- <sup>36</sup>A. Airapetian et al., “ATLAS: Detector and physics performance technical design report. Volume 2”, (1999).
- <sup>37</sup>G. L. Bayatian et al., “CMS Physics: Technical Design Report Volume 1: Detector Performance and Software”, (2006).
- <sup>38</sup>T. Abe et al., *Belle ii technical design report*, 2010.
- <sup>39</sup>“Juno physics and detector”, *Progress in Particle and Nuclear Physics* **123**, 103927 (2022).
- <sup>40</sup>D. A. Glaser, “Some effects of ionizing radiation on the formation of bubbles in liquids”, *Phys. Rev.* **87**, 665–665 (1952).
- <sup>41</sup>J. Chadwick, “The intensity distribution in the magnetic spectrum of beta particles from radium (B + C)”, *Verh. Phys. Gesell.* **16**, 383–391 (1914).
- <sup>42</sup>J. S. Chadwick, “Possible existence of a neutron”, *Nature* **129**, 312–312 (1932).
- <sup>43</sup>E. Fermi, “Versuch einer Theorie der  $\beta$ -Strahlen. I”, *Zeitschrift fur Physik* **88**, 161–177 (1934).
- <sup>44</sup>C. L. Cowan, F. Reines, F. B. Harrison, H. W. Kruse, and A. D. McGuire, “Detection of the free neutrino: a confirmation”, *Science* **124**, 103–104 (1956).
- <sup>45</sup>G. Danby, J.-M. Gaillard, K. Goulianos, L. M. Lederman, N. Mistry, M. Schwartz, and J. Steinberger, “Observation of high-energy neutrino reactions and the existence of two kinds of neutrinos”, *Phys. Rev. Lett.* **9**, 36–44 (1962).
- <sup>46</sup>F. P. An et al., “Observation of electron-antineutrino disappearance at daya bay”, *Phys. Rev. Lett.* **108**, 171803 (2012).
- <sup>47</sup>Q. R. Ahmad et al., “Direct evidence for neutrino flavor transformation from neutral-current interactions in the sudbury neutrino observatory”, *Phys. Rev. Lett.* **89**, 011301 (2002).

- <sup>48</sup>M. A. Acero et al., “First measurement of neutrino oscillation parameters using neutrinos and antineutrinos by nova”, [Phys. Rev. Lett. \*\*123\*\*, 151803 \(2019\)](#).
- <sup>49</sup>K. Abe et al., “Indication of electron neutrino appearance from an accelerator-produced off-axis muon neutrino beam”, [Phys. Rev. Lett. \*\*107\*\*, 041801 \(2011\)](#).
- <sup>50</sup>J. K. Ahn et al., “Observation of reactor electron antineutrinos disappearance in the reno experiment”, [Phys. Rev. Lett. \*\*108\*\*, 191802 \(2012\)](#).
- <sup>51</sup>S. Fukuda et al., “Determination of solar neutrino oscillation parameters using 1496 days of super-kamiokande-i data”, [Physics Letters B \*\*539\*\*, 179–187 \(2002\)](#).
- <sup>52</sup>K. Eguchi et al., “First results from kamland: evidence for reactor antineutrino disappearance”, [Phys. Rev. Lett. \*\*90\*\*, 021802 \(2003\)](#).
- <sup>53</sup>Y. Abe et al., “Indication of reactor  $\bar{\nu}_e$  disappearance in the double chooz experiment”, [Phys. Rev. Lett. \*\*108\*\*, 131801 \(2012\)](#).
- <sup>54</sup>R. Davis, D. S. Harmer, and K. C. Hoffman, “Search for neutrinos from the sun”, [Phys. Rev. Lett. \*\*20\*\*, 1205–1209 \(1968\)](#).
- <sup>55</sup>G. Charpak, R. Bouclier, T. Bressani, J. Favier, and C. Zupancic, “The Use of Multiwire Proportional Counters to Select and Localize Charged Particles”, [Nucl. Instrum. Meth. \*\*62\*\*, 262–268 \(1968\)](#).
- <sup>56</sup>J. N. Marx and D. R. Nygren, “The time projection chamber”, [Physics Today \*\*31\*\*, 46–53 \(1978\)](#).
- <sup>57</sup>E. Aprile et al., “The XENON1t dark matter experiment”, [The European Physical Journal C \*\*77\*\*, 10.1140/epjc/s10052-017-5326-3 \(2017\)](#).
- <sup>58</sup>C. Rubbia, *The liquid-argon time projection chamber: a new concept for neutrino detectors*, tech. rep. (1977).
- <sup>59</sup>R. Acciarri et al., “Demonstration of mev-scale physics in liquid argon time projection chambers using argoneut”, [Phys. Rev. D \*\*99\*\*, 012002 \(2019\)](#).
- <sup>60</sup>R. Acciarri et al., “Design and construction of the microboone detector”, [Journal of Instrumentation \*\*12\*\*, P02017 \(2017\)](#).
- <sup>61</sup>R. Acciarri et al., “The liquid argon in a testbeam (lariat) experiment”, [Journal of Instrumentation \*\*15\*\*, P04026 \(2020\)](#).
- <sup>62</sup>A. Friedland and S. W. Li, “Understanding the energy resolution of liquid argon neutrino detectors”, [Phys. Rev. D \*\*99\*\*, 036009 \(2019\)](#).

- <sup>63</sup>F. Arneodo, *The icarus experiment, a second-generation proton decay experiment and neutrino observatory at the gran sasso laboratory*, 2001.
- <sup>64</sup>K. Abe et al., “Search for proton decay via  $p \rightarrow e^+\pi^0$  and  $p \rightarrow \mu^+\pi^0$  in 0.31 megaton · years exposure of the super-kamiokande water cherenkov detector”, *Phys. Rev. D* **95**, 012004 (2017).
- <sup>65</sup>P. Nath and R. Arnowitt, “Limits on photino and squark masses from proton lifetime in supergravity models”, *Phys. Rev. D* **38**, 1479–1484 (1988).
- <sup>66</sup>H.-K. Proto-Collaboration et al., *Hyper-kamiokande design report*, 2018.
- <sup>67</sup>G. M. Fuller, R. W. Mayle, J. R. Wilson, and D. N. Schramm, “Resonant Neutrino Oscillations and Stellar Collapse”, *apj* **322**, 795 (1987).
- <sup>68</sup>K. Abe et al., “Measurements of neutrino oscillation in appearance and disappearance channels by the t2k experiment with  $6.6 \times 10^{20}$  protons on target”, *Phys. Rev. D* **91**, 072010 (2015).
- <sup>69</sup>B. Pontecorvo, “Inverse beta processes and nonconservation of lepton charge”, *Zh. Eksp. Teor. Fiz.* **34**, 247 (1957).
- <sup>70</sup>Z. Maki, M. Nakagawa, and S. Sakata, “Remarks on the Unified Model of Elementary Particles”, *Progress of Theoretical Physics* **28**, 870–880 (1962).
- <sup>71</sup>L. Wolfenstein, “Neutrino oscillations in matter”, *Phys. Rev. D* **17**, 2369–2374 (1978).
- <sup>72</sup>A. Y. Smirnov, “The msw effect and matter effects in neutrino oscillations”, *Physica Scripta* **2005**, 57–64 (2004).
- <sup>73</sup>P Sadowski, B Radics, Ananya, Y Yamazaki, and P Baldi, “Efficient antihydrogen detection in antimatter physics by deep learning”, *Journal of Physics Communications* **1**, 025001 (2017).
- <sup>74</sup>P. Sadowski and P. Baldi, “Deep learning in the natural sciences: applications to physics”, in Braverman readings in machine learning (2017).
- <sup>75</sup>D. Dwyer, M. Garcia-Sciveres, D. Gnani, C. Grace, S. Kohn, M. Kramer, A. Krieger, C. Lin, K. Luk, P. Madigan, C. Marshall, H. Steiner, and T. Stezelberger, “Larpix: demonstration of low-power 3d pixelated charge readout for liquid argon time projection chambers”, *Journal of Instrumentation* **13**, P10007 (2018).
- <sup>76</sup>J. Asaadi, M. Auger, A. Ereditato, D. Goeldi, R. Hänni, U. Kose, I. Kreslo, D. Lorca, M. Luethi, C. R. von Rohr, J. Sinclair, F. Stocker, C. Tognina, and M. Weber, “A pixelated charge readout for liquid argon time projection chambers”, *Journal of Instrumentation* **13**, C02008 (2018).
- <sup>77</sup>B. Abi et al., “Volume iii. dune far detector technical coordination”, *Journal of Instrumentation* **15**, T08009 (2020).

- <sup>78</sup>L. Paulucci and on behalf of DUNE collaboration, “The dune vertical drift photon detection system”, *Journal of Instrumentation* **17**, C01067 (2022).
- <sup>79</sup>J. Joshi and X. Qian, *Signal processing in the microboone larpc*, 2015.
- <sup>80</sup>S. Agostinelli et al., “Geant4—a simulation toolkit”, *Nuclear Instruments and Methods in Physics Research Section A: Accelerators, Spectrometers, Detectors and Associated Equipment* **506**, 250–303 (2003).
- <sup>81</sup>*Zybo z7 board reference manual*, Zybo Z7 Reference Manual, Digilent ([https://digilent.com/reference/\\_media/reference/zybo-z7/zybo-z7\\_rm.pdf](https://digilent.com/reference/_media/reference/zybo-z7/zybo-z7_rm.pdf)).
- <sup>82</sup>Y. Li, T. Tsang, C. Thorn, X. Qian, M. Diwan, J. Joshi, S. Kettell, W. Morse, T. Rao, J. Stewart, W. Tang, and B. Viren, “Measurement of longitudinal electron diffusion in liquid argon”, *Nuclear Instruments and Methods in Physics Research Section A: Accelerators, Spectrometers, Detectors and Associated Equipment* **816**, 160–170 (2016).
- <sup>83</sup>Lattice, *Ice40 ultraplus family data sheet*, lattice ice40up fpga data sheet, Lattice Semiconductor (<https://www.latticesemi.com/-/media/LatticeSemi/Documents/DataSheets/iCE/iCE40-UltraPlus-Family-Data-Sheet.ashx>).
- <sup>84</sup>N. None, “Study of reconstructed 39ar beta decays at the microboone detector”, [10.2172/1573057](https://doi.org/10.2172/1573057) (2018).
- <sup>85</sup>J. Shi, *Studies of radiological backgrounds in the dune far detector and the sensitivity to the solar neutrino day-night effect using the photon-detector system*, 2019.
- <sup>86</sup>R. Acciarri et al., “A study of electron recombination using highly ionizing particles in the ArgoNeuT Liquid Argon TPC”, *Journal of Instrumentation* **8**, P08005, P08005 (2013).
- <sup>87</sup>C. Marshall, K. McFarland, and C. Wilkinson, “Neutrino-electron elastic scattering for flux determination at the dune oscillation experiment”, *Physical Review D* **101**, [10.1103/PhysRevD.101.032002](https://doi.org/10.1103/PhysRevD.101.032002) (2020).

*Appendix A*

NEUTRINO INTERACTION INTEGRAL DATA

lepton Pdg	Horn Current Direction	Z-Pos	Theta	95% Capture	99% Capture
12	forward	10	0	262	398
12	forward	80	0	270	402
12	forward	180	0	262	402
12	forward	280	0	254	378
12	forward	350	0	242	378
12	forward	10	2	266	390
12	forward	80	2	270	422
12	forward	180	2	270	414
12	forward	280	2	258	378
12	forward	350	2	238	398
12	forward	10	-2	266	426
12	forward	80	-2	266	426
12	forward	180	-2	266	410
12	forward	280	-2	258	398
12	forward	350	-2	246	366
12	forward	10	90	946	1526
12	forward	80	90	950	1554
12	forward	180	90	922	1638
12	forward	280	90	798	1426
12	forward	350	90	238	326
12	forward	10	-90	274	390
12	forward	80	-90	874	1570
12	forward	180	-90	954	1670
12	forward	280	-90	918	1586
12	forward	350	-90	906	1666

12	forward	10	0	262	398
12	forward	10	2	266	390
12	forward	10	-2	266	426
12	forward	10	90	946	1526
12	forward	10	-90	274	390
12	forward	80	0	270	402
12	forward	80	2	270	422
12	forward	80	-2	266	426
12	forward	80	90	950	1554
12	forward	80	-90	874	1570
12	forward	180	0	262	402
12	forward	180	2	270	414
12	forward	180	-2	266	410
12	forward	180	90	922	1638
12	forward	180	-90	954	1670
12	forward	280	0	254	378
12	forward	280	2	258	378
12	forward	280	-2	258	398
12	forward	280	90	798	1426
12	forward	280	-90	918	1586
12	forward	350	0	242	378
12	forward	350	2	238	398
12	forward	350	-2	246	366
12	forward	350	90	238	326
12	forward	350	-90	906	1666
-12	forward	10	0	238	362
-12	forward	80	0	246	370
-12	forward	180	0	234	358
-12	forward	280	0	230	370
-12	forward	350	0	214	334
-12	forward	10	2	230	358
-12	forward	80	2	238	382

-12	forward	180	2	234	350
-12	forward	280	2	226	350
-12	forward	350	2	214	330
-12	forward	10	-2	234	382
-12	forward	80	-2	238	358
-12	forward	180	-2	238	358
-12	forward	280	-2	226	362
-12	forward	350	-2	214	334
-12	forward	10	90	710	1378
-12	forward	80	90	686	1274
-12	forward	180	90	666	1350
-12	forward	280	90	582	1250
-12	forward	350	90	206	306
-12	forward	10	-90	238	354
-12	forward	80	-90	634	1358
-12	forward	180	-90	670	1358
-12	forward	280	-90	702	1454
-12	forward	350	-90	666	1354
-12	forward	10	0	238	362
-12	forward	10	2	230	358
-12	forward	10	-2	234	382
-12	forward	10	90	710	1378
-12	forward	10	-90	238	354
-12	forward	80	0	246	370
-12	forward	80	2	238	382
-12	forward	80	-2	238	358
-12	forward	80	90	686	1274
-12	forward	80	-90	634	1358
-12	forward	180	0	234	358
-12	forward	180	2	234	350
-12	forward	180	-2	238	358
-12	forward	180	90	666	1350

-12	forward	180	-90	670	1358
-12	forward	280	0	230	370
-12	forward	280	2	226	350
-12	forward	280	-2	226	362
-12	forward	280	90	582	1250
-12	forward	280	-90	702	1454
-12	forward	350	0	214	334
-12	forward	350	2	214	330
-12	forward	350	-2	214	334
-12	forward	350	90	206	306
-12	forward	350	-90	666	1354
-12	reverse	10	0	222	342
-12	reverse	80	0	226	334
-12	reverse	180	0	226	326
-12	reverse	280	0	218	322
-12	reverse	350	0	202	306
-12	reverse	10	2	226	322
-12	reverse	80	2	222	330
-12	reverse	180	2	222	326
-12	reverse	280	2	214	318
-12	reverse	350	2	198	290
-12	reverse	10	-2	218	326
-12	reverse	80	-2	226	342
-12	reverse	180	-2	218	318
-12	reverse	280	-2	214	322
-12	reverse	350	-2	202	306
-12	reverse	10	90	710	1374
-12	reverse	80	90	674	1378
-12	reverse	180	90	642	1434
-12	reverse	280	90	578	1266
-12	reverse	350	90	194	286
-12	reverse	10	-90	230	330

-12	reverse	80	-90	590	1314
-12	reverse	180	-90	622	1334
-12	reverse	280	-90	674	1398
-12	reverse	350	-90	638	1310
-12	reverse	10	0	222	342
-12	reverse	10	2	226	322
-12	reverse	10	-2	218	326
-12	reverse	10	90	710	1374
-12	reverse	10	-90	230	330
-12	reverse	80	0	226	334
-12	reverse	80	2	222	330
-12	reverse	80	-2	226	342
-12	reverse	80	90	674	1378
-12	reverse	80	-90	590	1314
-12	reverse	180	0	226	326
-12	reverse	180	2	222	326
-12	reverse	180	-2	218	318
-12	reverse	180	90	642	1434
-12	reverse	180	-90	622	1334
-12	reverse	280	0	218	322
-12	reverse	280	2	214	318
-12	reverse	280	-2	214	322
-12	reverse	280	90	578	1266
-12	reverse	280	-90	674	1398
-12	reverse	350	0	202	306
-12	reverse	350	2	198	290
-12	reverse	350	-2	202	306
-12	reverse	350	90	194	286
-12	reverse	350	-90	638	1310
14	forward	10	0	258	370
14	forward	80	0	258	386
14	forward	180	0	254	366

14	forward	280	0	246	358
14	forward	350	0	238	338
14	forward	10	2	258	382
14	forward	80	2	258	398
14	forward	180	2	258	394
14	forward	280	2	246	334
14	forward	350	2	226	338
14	forward	10	-2	254	378
14	forward	80	-2	262	386
14	forward	180	-2	254	354
14	forward	280	-2	238	346
14	forward	350	-2	230	326
14	forward	10	90	786	1534
14	forward	80	90	798	1470
14	forward	180	90	754	1454
14	forward	280	90	682	1338
14	forward	350	90	234	322
14	forward	10	-90	258	382
14	forward	80	-90	726	1494
14	forward	180	-90	778	1490
14	forward	280	-90	766	1366
14	forward	350	-90	786	1482
14	forward	10	0	258	370
14	forward	10	2	258	382
14	forward	10	-2	254	378
14	forward	10	90	786	1534
14	forward	10	-90	258	382
14	forward	80	0	258	386
14	forward	80	2	258	398
14	forward	80	-2	262	386
14	forward	80	90	798	1470
14	forward	80	-90	726	1494

14	forward	180	0	254	366
14	forward	180	2	258	394
14	forward	180	-2	254	354
14	forward	180	90	754	1454
14	forward	180	-90	778	1490
14	forward	280	0	246	358
14	forward	280	2	246	334
14	forward	280	-2	238	346
14	forward	280	90	682	1338
14	forward	280	-90	766	1366
14	forward	350	0	238	338
14	forward	350	2	226	338
14	forward	350	-2	230	326
14	forward	350	90	234	322
14	forward	350	-90	786	1482
14	reverse	10	0	270	382
14	reverse	80	0	278	406
14	reverse	180	0	266	394
14	reverse	280	0	258	378
14	reverse	350	0	242	366
14	reverse	10	2	274	402
14	reverse	80	2	282	390
14	reverse	180	2	266	398
14	reverse	280	2	262	374
14	reverse	350	2	242	374
14	reverse	10	-2	262	406
14	reverse	80	-2	274	418
14	reverse	180	-2	262	378
14	reverse	280	-2	258	394
14	reverse	350	-2	238	354
14	reverse	10	90	942	1570
14	reverse	80	90	898	1618

14	reverse	180	90	842	1550
14	reverse	280	90	822	1522
14	reverse	350	90	234	334
14	reverse	10	-90	270	406
14	reverse	80	-90	838	1526
14	reverse	180	-90	898	1610
14	reverse	280	-90	914	1562
14	reverse	350	-90	894	1642
14	reverse	10	0	270	382
14	reverse	10	2	274	402
14	reverse	10	-2	262	406
14	reverse	10	90	942	1570
14	reverse	10	-90	270	406
14	reverse	80	0	278	406
14	reverse	80	2	282	390
14	reverse	80	-2	274	418
14	reverse	80	90	898	1618
14	reverse	80	-90	838	1526
14	reverse	180	0	266	394
14	reverse	180	2	266	398
14	reverse	180	-2	262	378
14	reverse	180	90	842	1550
14	reverse	180	-90	898	1610
14	reverse	280	0	258	378
14	reverse	280	2	262	374
14	reverse	280	-2	258	394
14	reverse	280	90	822	1522
14	reverse	280	-90	914	1562
14	reverse	350	0	242	366
14	reverse	350	2	242	374
14	reverse	350	-2	238	354
14	reverse	350	90	234	334

14	reverse	350	-90	894	1642
-14	forward	10	0	222	326
-14	forward	80	0	226	334
-14	forward	180	0	214	322
-14	forward	280	0	210	314
-14	forward	350	0	194	302
-14	forward	10	2	218	342
-14	forward	80	2	222	330
-14	forward	180	2	214	322
-14	forward	280	2	210	314
-14	forward	350	2	198	290
-14	forward	10	-2	218	322
-14	forward	80	-2	222	322
-14	forward	180	-2	214	310
-14	forward	280	-2	206	314
-14	forward	350	-2	202	298
-14	forward	10	90	578	1274
-14	forward	80	90	578	1254
-14	forward	180	90	522	1186
-14	forward	280	90	490	1046
-14	forward	350	90	182	270
-14	forward	10	-90	218	314
-14	forward	80	-90	546	1214
-14	forward	180	-90	570	1150
-14	forward	280	-90	538	1190
-14	forward	350	-90	550	1238
-14	forward	10	0	222	326
-14	forward	10	2	218	342
-14	forward	10	-2	218	322
-14	forward	10	90	578	1274
-14	forward	10	-90	218	314
-14	forward	80	0	226	334

-14	forward	80	2	222	330
-14	forward	80	-2	222	322
-14	forward	80	90	578	1254
-14	forward	80	-90	546	1214
-14	forward	180	0	214	322
-14	forward	180	2	214	322
-14	forward	180	-2	214	310
-14	forward	180	90	522	1186
-14	forward	180	-90	570	1150
-14	forward	280	0	210	314
-14	forward	280	2	210	314
-14	forward	280	-2	206	314
-14	forward	280	90	490	1046
-14	forward	280	-90	538	1190
-14	forward	350	0	194	302
-14	forward	350	2	198	290
-14	forward	350	-2	202	298
-14	forward	350	90	182	270
-14	forward	350	-90	550	1238
-14	reverse	10	0	218	338
-14	reverse	80	0	218	326
-14	reverse	180	0	210	318
-14	reverse	280	0	206	306
-14	reverse	350	0	194	294
-14	reverse	10	2	210	318
-14	reverse	80	2	210	338
-14	reverse	180	2	218	326
-14	reverse	280	2	206	302
-14	reverse	350	2	194	278
-14	reverse	10	-2	218	310
-14	reverse	80	-2	218	334
-14	reverse	180	-2	214	314

-14	reverse	280	-2	206	306
-14	reverse	350	-2	194	290
-14	reverse	10	90	514	1098
-14	reverse	80	90	486	1082
-14	reverse	180	90	498	1102
-14	reverse	280	90	446	1030
-14	reverse	350	90	174	266
-14	reverse	10	-90	218	326
-14	reverse	80	-90	486	1014
-14	reverse	180	-90	494	1110
-14	reverse	280	-90	494	1122
-14	reverse	350	-90	506	1118
-14	reverse	10	0	218	338
-14	reverse	10	2	210	318
-14	reverse	10	-2	218	310
-14	reverse	10	90	514	1098
-14	reverse	10	-90	218	326
-14	reverse	80	0	218	326
-14	reverse	80	2	210	338
-14	reverse	80	-2	218	334
-14	reverse	80	90	486	1082
-14	reverse	80	-90	486	1014
-14	reverse	180	0	210	318
-14	reverse	180	2	218	326
-14	reverse	180	-2	214	314
-14	reverse	180	90	498	1102
-14	reverse	180	-90	494	1110
-14	reverse	280	0	206	306
-14	reverse	280	2	206	302
-14	reverse	280	-2	206	306
-14	reverse	280	90	446	1030
-14	reverse	280	-90	494	1122

-14	reverse	350	0	194	294
-14	reverse	350	2	194	278
-14	reverse	350	-2	194	290
-14	reverse	350	90	174	266
-14	reverse	350	-90	506	1118

Table A.1: APA Integral Data

*Appendix B*

## Q-PIX ANALOG ASIC FIRST PROTOTYPE

**QPIX Layout: Integrator + Amplifier + Comparator**

Size: 350um x 90 um

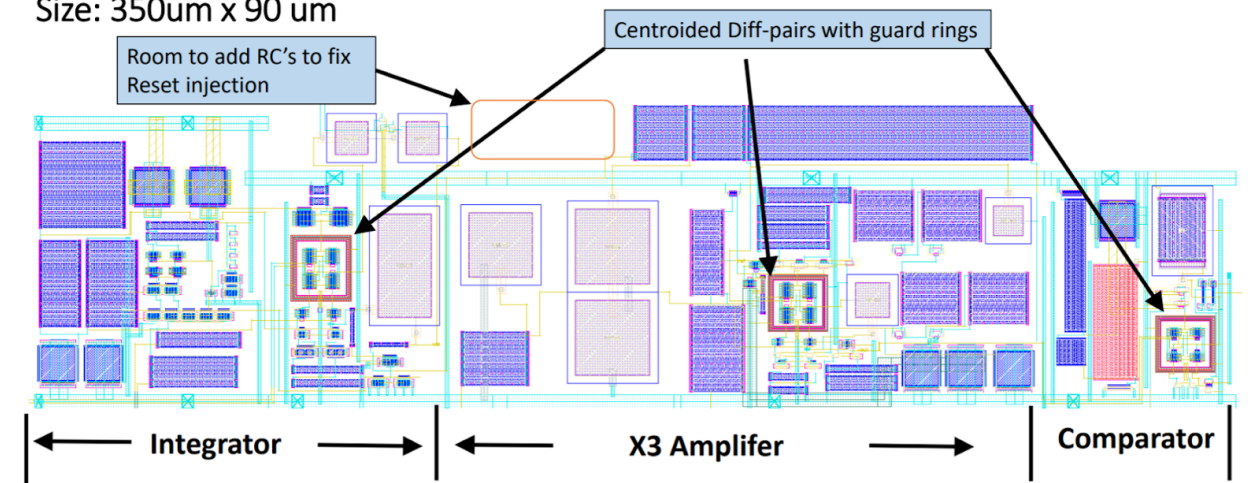


Figure B.1: Full Schematic of the upcoming Q-Pix analog front-end ASIC.